The Effect of Dimensional Parameters on the Dynamic Performance of Over-Arch Differential Drive Vehicles

THE UNIVERSITY OF
WAIKATO
Te Whare Wānanga o Waikato

A thesis submitted

in fulfilment of the requirements

for the degree of

Master of Engineering

At

The University of Waikato

Andrew Tattersall

2022

Declaration

In submitting this thesis to The University of Waikato School of Engineering, I affirm my awareness of the university's standards and honour code.

Name: Andrew Tattersall

Signature: A. J. Tattersall

Abstract

This work contributes to the field of agricultural vehicle dynamics by assessing the dimensional sensitivity of over-arch differential drive vehicle performance. The findings from this work are important for vehicle optimisation with regards to drive forces, energy consumption, chassis loading, and vehicle stability. Dimensional optimisation of the vehicles has been ignored, which is a problem if efficient and environmentally friendly autonomous over-arch agricultural vehicles are to be built.

Worldwide, one in nine people do not have enough food to eat. The World Food Program has a goal to end hunger and improve the quality of available food by 2030. In New Zealand, the agricultural industry contributes $13.8 billion dollars to annual GDP and is growing, making agriculture's contribution valuable to the New Zealand economy. However, there is a labour shortage in agriculture. This shortage of labour negatively effects food production. One potential solution to the labour shortage is automation.

Differential drive mobile robots (DDMRs) are often used in agricultural automation research because they are simple and cheap to build, and the drive system is ideal for an over-arch chassis design. Over-arch vehicles are often required in vineyards and apple orchards. Research into DDMRs is largely limited to optimisation of control and path tracking, but optimisation of the physical vehicle has been ignored. In order to optimise vehicle dimensions before manufacturing starts, the influence of dimensions on drive forces, energy consumption, chassis loading, and vehicle stability needs to be assessed.

In this study, a dynamic model of a large scale agricultural over-arch DDMR is constructed and the dimensional sensitivity of peak drive/braking force, energy consumption,

chassis shear force and lateral chassis splay/compression force is assessed. The effects of caster trail and the lateral position of the center of mass on stability are also assessed. Results show that peak drive/braking force, energy consumption, stability and chassis loading are all sensitive to vehicle dimensions to different degrees. Energy consumption showed the least sensitivity, while forces were found to be significantly influenced. For a large scale DDMR traversing common agricultural trajectories, increasing caster trail by 0.2 m, decreasing longitudinal position of the center of mass by 0.2 m, and increasing track width by 0.2 m provides a decrease in peak drive force of 56.4 %, 13.9 % and 9.37 % respectively. These sample results illustrate the importance of understanding dimensional sensitivity, because they are not insignificant. The dimensional sensitivities were also found to be a good guide for vehicles of smaller scale. A case study was conducted on a Simulink model of a large scale over-arch DDMR designed for operating in vineyards. Dimensional optimisation was successfully performed such that the vehicle was able to operate adequately in the simulated vineyard environment. The case study illustrates that dimensional sensitivity is useful for the optimisation of a vehicle for its intended working environment.

This works shows that physical optimisation of these vehicles is extremely important. If optimised, savings could be found in energy consumption, cost, and materials. As automation becomes more important, accurate vehicle control is essential for performance and safety, and the work in this thesis helps to achieve this. The products of dimensional optimisation benefit the overall effort to fill the labour gap and supply enough food for the worlds growing population.

Acknowledgements

- First of all, I want to thank my supervisor, Dr. Ben McGuinness, for all the time he has put into this project. His input and expertise have been invaluable.
- I want to thank the Ministry of Business, Innovation and Employment for funding this research, and I want to thank Professor Mike Duke and Dr Shen Hin Lim for not only leading the University of Waikato division but also for their technical input.
- I also would like to thank my parents, Alton and Rose, for their continued love and support during my studies, as well as the rest of my family and friends.
- Finally, I want to thank the rest of the team in D.G.12 for their support and for making the working environment fun and engaging.

Table of Contents

List of Figures

List of Tables

Chapter 1

Introduction

1.1 Overview

Food security is a global concern, particularly with the population forecast to rise to 9.7 billion by 2050 [6]. Worldwide, one in nine people to do not have enough food to eat [7], thus there is a lot of interest in solving this problem. The World Food Program has a goal to end hunger and improve the quality of available food by 2030 [7]. However, there are factors restricting growth of food production. Labours shortages, extreme weather events and world conflicts are just a few.

In New Zealand , the agriculture industry contributes $13.8 billion dollars to annual GDP and is still growing (Figure 1.1) [1], making its contribution valuable to the New Zealand's economy. However, in New Zealand, there is a labour shortage in the agriculture industry [8][9][10][11][12]. One potential solution to the labour shortage, hence addressing world hunger, is automation. Automation in agriculture is becoming more common [13]. However, working in outdoor unstructured environments is difficult, with bad weather conditions and poor lighting having a significant impact. Also, agricultural tasks done by humans are often complex and difficult to replicate with automation. If functionality is achieved, automation also needs to be cost effective for growers. Autonomous tractors do exist [14], but tractors are generally designed to haul other equipment specifically

designed to do the actual task. Ideally, a cheap, simple, all-in-one machine designed for the task at hand is available. For these reasons, different types of agricultural vehicles are being considered.

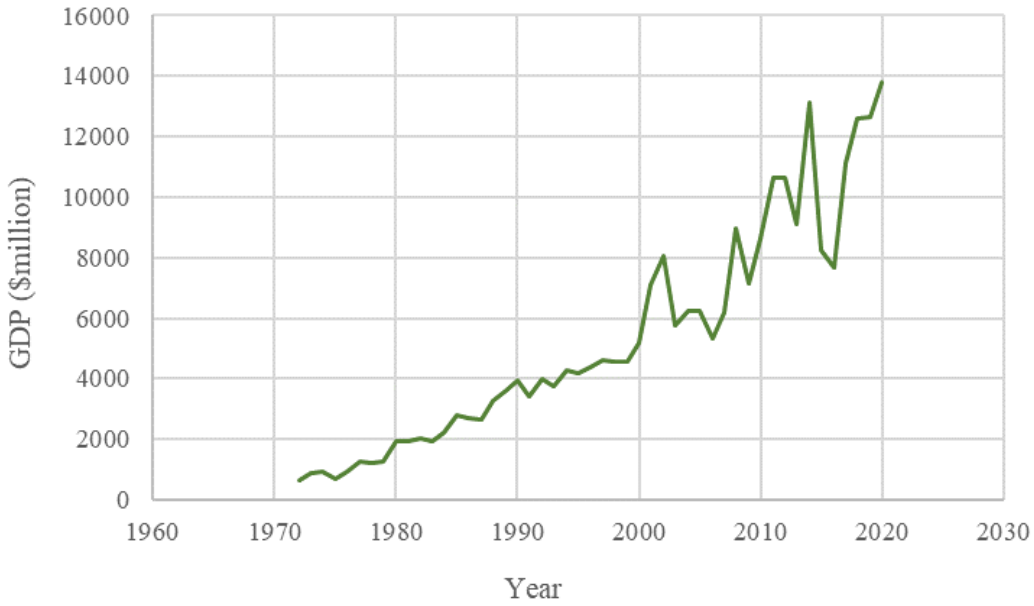

Figure 1.1: *Agriculture GDP in NZ by year [1].*

1.2 Differential Drive Mobile Vehicles

Powered traction vehicles have been used in agriculture since the 19^{th} century [15] and are part of the increased crop production caused by mechanisation [16]. However, the task of detecting and harvesting food crops autonomously is not necessarily well suited for traditional farm machinery. In order to choose the best machine for the job, one must compare one machine to another. Important things to consider are function (ability to do the required task) cost, simplicity, maintenance, duty cycle, and environmental impact.

Most tractors run off diesel and have ackermann steering (electric versions do exist [17]). Using diesel means only brief stops are required for refueling, and ackermann steering is robust and well understood. Some farm vehicles use skid steering [18]. Skid steering does away with ackermann steering, reducing the complexity of the vehicle, and the four powered wheels provide good traction. Tracked vehicles provide similar benefits to skid

steered though are better on softer surfaces. Using electricity rather than diesel as a power source can allow the design of extremely mobile vehicles (especially if in hub motors are used). Ted, an over-arch vineyard weeding robot, has four electrically powered and steered wheels allowing it to maneuver in tight spaces [19].

The before mentioned vehicles all have benefits. However, the diesel powered skid steered and tracked vehicles all have a negative impact on the environment due their excess carbon emissions. Also, the complexity of their design could potentially be reduced. An inherent property of these drive systems is that the tires/tracks skid across the ground during turns, and the forces induced on the chassis due to this could significantly deflect the chassis, particularly if the chassis is of over-arch design. Furthermore, this skidding motion can excessively tear up the ground during operation (depending on the surface), potentially damaging shallow root systems. Ted reduces the problem of emissions by using batteries and electric motors [19]. However, the reduction of carbon emissions with this method will depend on the type of electricity generation and embedded carbon from manufacturing. The vehicle does require eight different motors to drive and steer meaning the complexity and cost of the design is high. A potential solution to the problems outlined is the differential drive mobile robot/vehicle (DDMR). A DDMR only requires two motors to provide power and steering, and is mechanically suited for electric motors (particularly in-hub motors). A differential drive is also ideal for over-arch chassis (which are required for some tasks) because electric motors require minimal space and the wheels cannot be connected to each other via an axle and differential. Research vehicles designed for agriculture and other applications are often DDMRs for these reasons [20][21][22][23][24]. One key draw back to the differential drive is the reliance on accurate drive wheel velocities to keep the vehicle on a desired trajectory, and it can be difficult to control in sloped and uneven orchards. Upon reviewing DDMRs, it was found that they are typically small scale. A common example is a vacuum cleaning robot. However, some recent DDMRs are large scale and are discussed in section 1.3.

1.3 Maaratech Project

Today, the Ministry of Business, Innovation and Employment (MBIE) is putting funding towards research in the agricultural industry. The focus of the research is to find ways of filling the labour gap as well as improve the working conditions of the current labour force. Fully autonomous harvesting systems are a focus of the research, and these systems typically consist of cameras, manipulators, end-effectors and autonomous vehicles. Some of these autonomous vehicles require an over-arch chassis because their purpose is to travel over crop rows or trellises and scan and harvest autonomously. Examples of these over-arch DDMRs are some of the vehicles designed at the University of Waikato (Figure 1.2). These vehicles were designed for imaging and harvesting tasks in vineyards and 2D apple orchards.

(a) (b)

Figure 1.2: *"Archie Senior" (a) and "Archie Junior" (b).*

During field testing, the vehicles did not perform as expected and the motions of the vehicles were unpredictable. The casters were the apparent cause. If vehicles were driven forward and then reversed, the front end of the vehicles fishtailed as the casters spun around to orientate with the direction of motion. This problem could potentially be improved though better control of the drive wheels. However, performing dimensional optimisation (increasing caster trail for example) could also improve stability, meaning the motors controllers would have less work to do.

Another issue was discovered when trying to manoeuvre on a slope. One of the vehicles failed to do so predictably. This is an issue because operating environments for agricultural vehicles are rarely flat. A potential problem could be the control script for the differential drive. However, understanding of how physical dimensions of the vehicle affect motion on slopes would be very valuable for improving design and therefore performance.

Problems were also found with chassis deformation. The vehicles were constructed using the over-arch chassis design, making the chassis inherently less stiff. Chassis deformation was observed during operation of the vehicles. Understanding of the forces applied to these vehicles during operation would be valuable for optimisation of chassis stiffness. Many agricultural vehicles use the over-arch design [25][26][27][28][29][30][31][32], so it is important to understand how dynamic forces stress the frame.

So, these over-arch DMMR's need to be optimised to improve their performance. Vehicle optimisation is not new (think of the evolution of automobiles for racing and civilian use). However, the agricultural environment is very different to the road or race track, and the drive system and chassis design are very different for over-arch DDMRs, significantly reducing the relevance of automobile optimisation. It should be noted that automobiles such as utes have been optimised for agriculture environment, but again, the drive system and chassis are very different. Optimisation of DDMR's is typically done by building better controllers, but the physical design of the vehicles is largely ignored during optimisation, and little work has been on large scale over-arch DDMRs.

It is proposed that the dynamic behaviour of a DDMR is more sensitive to particular vehicle dimensions over others. Improving the performance and predictability of a vehicle (by optimising vehicle dimensions) will inherently make the vehicle easier to control, and therefore should be done first. Besides control, dimensional optimisation will allow the selection of smaller and lighter vehicle components (motors and chassis etc) which in turn reduce the overall cost of manufacture and operation.

1.4 Objective

The purpose of this study is to widen the field of agricultural vehicle dynamics and increase understanding of over-arch DDMR dynamics, to allow better optimisation of design with regard to drive forces required, energy consumption, stability, and forces applied to an over-arch frame. In particular, this study focuses on the influence of vehicle dimensions on these variables. Center of mass (COM) position, caster dimensions, and chassis dimensions are of special interest. It is hoped this study is useful for the design and optimisation of over-arch differential drive vehicles. Improving the design of these vehicles aids the task of increasing food production and filling the labour gap in the agricultural industry via automation.

1.5 Approach

Using the correct approach when conducting a study is very important when valuable and relevant information is desired. In order to understand the effect each vehicle dimension has on performance, each one can be adjusted independently and the variables defining vehicle performance measured. This is the approach used in this study, and is done by constructing a dynamic model that includes all dimensions of interest and then adjusting said dimensions. This is a straight forward method to gather valuable information regarding dimensional sensitivity. Each agricultural task and working environment requires different vehicle trajectories. Therefore, to obtain relevant information, dimensional sensitivity is assessed on typical trajectories found in an agricultural working environment. To determine the dynamic model's accuracy, and therefore the results obtained from the model, it is compared with other data. Real world experiments are favoured and are used when practically possible, but motion software is also used.

1.6 Contribution

This work contributes to the field of agricultural robotics by providing a better understanding of the sensitivity of over-arch DDMR dynamics to vehicle dimensions. An improved understanding of the effect of dimensions on performance allows over-arch DDMRs to be better optimised for the task at hand and allows for easier control and path tracking. Vehicle cost and environmental impact can also be reduced. Much research has be done regarding control and path tracking for these vehicles, but physical optimisation has been ignored, and this work helps to fill this gap. In some cases, a DDMR may not be the best option for the specific working environment, and this work aids in determining such scenarios. These specific study outcomes aid the overall effort to help growers to fill the labour gap and keep the agricultural industry in step with the demands of population growth and the goal of no hunger by 2030.

1.7 Thesis Overview

Chapter 2 reviews research into DDMR optimisation via dimensional analysis with regards to drive forces, stability, energy consumption, and the forces induced in an over-arch chassis. Optimisation of a DDMR in slope environments is also reviewed, as well as typical variables included in dynamic models.

In Chapter 3 a dynamic model of a DDMR is defined as well as the kinematics required to build the model. The method used to evaluate forces induced in an over-arch chassis is also presented.

The accuracy of the dynamic model is assessed in Chapter 4. It is compared with Solidworks Motion as well as real world data. More specifically, caster reaction forces are determined via an experiment, and a mid size DDMR is compared to the model.

Chapter 5 discusses the simulations conducted to assess dimensional sensitivity for vehicle stability, chassis loading, and drive forces. It presents the simulation parameters used as well as descriptions of the vehicles modelled.

Chapter 6 presents and discusses results for dimension sensitivity with regards to stability, drive forces, and chassis loading. The sensitivity of different vehicle dimensions are also compared relative to each other on different trajectories.

Chapter 7 concludes the thesis, outlining key findings from the study. The most significant dimensional sensitivities are presented as well as other results such as the effect of caster trail and the position of the COM on stability.

Chapter 2

Literature Review

This chapter will review research into DDMR optimisation, the forces induced in an over-arch chassis due to casters and drive wheels, energy consumption, and vehicle stability. It will consider vehicle dimension optimisation, over-arch chassis optimisation, caster behaviour, and the impact of a sloped working environment. Dynamic models will be reviewed as well as mathematical methods. Kinematic models, while needed to plot trajectories and build dynamic models, will not be reviewed because they are well understood and easy to implement and this study is chiefly focused on the dynamic behaviour of DDMRs.

2.1 Mathematical Methods

In order to build a dynamic model of a DDMR, a mathematical method needs to be selected. Lagrangian and Newton-Euler mechanics are most commonly used to build dynamic models, but others such as Kane's method have also been used [33]. It has been shown that the Lagrangian and Newton Euler method are equivalent mathematically [34], and both methods were found to be the same in terms of computational efficiency when studying dynamic models of manipulators [35]. The Lagrangian formulation is deemed to be a less complex approach because the Newton-Euler method requires all

reaction and frictional forces to be known, and these forces can be hard to quantify [34]. The mathematical form of Lagrangian mechanics is cleaner for complex systems when compared to Newton-Euler, and is more easily applied to a large variety of physical problems [36]. However, the dynamics of a DDMR are relatively simple making the benefits of Lagrangian mechanics less obvious. Also, Lagrangian mechanics are not always taught at an undergraduate level giving poor readability for some readers. So, recognising that Lagrangian mechanics are not intrinsically required for the model, Newton-Euler is the best option due to its readability.

2.2 Existing Dynamic Models

To use a dynamic model to study and optimise a DDMR, the model needs to include the components of interest. Many dynamic models of DDMRs exist and are well understood. However, not all models include the same vehicle parameters and components. At a minimum, only the drive wheels and main chassis are considered, and the COM is kept on the longitudinal axis of the vehicle. The casters are often ignored. More complex models include caster wheels [37], lateral position of COM [38][4], normal forces [39][40], camber [41], and wheel slip [40][42]. Very simple models are only kinematic. Kinematic models are required to build dynamic models, but dynamic models are needed for dimensional optimisation. Some models also include detailed motor characteristics [43][44]. One key parameter that is most often not included is the angle of the slope the vehicle is driving on. This is important as the working environments of agricultural vehicles is often sloped. Though not as common, there are studies that include it [42][40][45]. A crucial component for a detailed dynamics model is the instantaneous caster angles. Real time caster orientation is very important if instantaneous caster reaction forces are to be analysed. Efforts have been made to model real time caster orientation so that they can be taken into account by a controller. A study successfully did this, finding that a 1st order transfer function is adequate to describe the orientation of the caster wheels [46]. A model to predict instantaneous caster orientation was also successfully built by Chenier et al [47].

Based on this review, enough models exist to provide the information needed to build the dynamic model required for dimensional optimisation.

2.3 Optimisation of Differential Drive Mobile Robots

Vehicles, especially automobiles, are constantly being optimised and improved. A great example is the Formula 1 race car. However, these vehicles are not typically optimised for the agricultural environment (except for tractors and farm vehicles). Ackermann steering is almost exclusively used for automobiles and tractors, with skid or track steering sometimes being used for excavating equipment. In general, these vehicles are designed for much higher speeds and accelerations than what could would be expected of an over-arch DDMR. Also, chassis designs are extremely different to over-arch vehicles. For these reasons, research into the optimisation of automobiles and tractors is not useful for this study.

A large number of studies have focused on DDMR control [48][49][50][51][52][53][54][43] [55][56]. However, these studies do not consider optimisation of the physical robot to improve performance. Physical optimisation is important for DDMRs, especially at large scale as they are heavy and require larger quantities of energy and large drive forces to operate. Higher capacity battery packs are required to account for this greater energy requirement, adding even more weight and increasing battery capacity exponentially [57]. In terms of smaller scale robots, studies have looked at a couple of parameters, vertical load capacity and center of mass position. One study looked at the effect of weight distribution in a manual wheelchair (which has the same configuration as a DDMR) on propulsion [58]. They found that shifting mass away from the drive wheels increased propulsion torques by as much as 73 %, which is very relevant. Floor surface type (tile or carpet) was also found to have an effect on torques. Another study looked at the effect of the ratio between a circular DDMRs width and the planned work space area on the mobility of the robot. 0.8 was found to be the ideal ratio between a circular DDMR and the path/corridor along which it is required to travel [59]. The study is

incomplete because they did not ascertain changes in energy consumption, drive forces, or chassis loading, and the vehicle was at a very small scale. Research was conducted into the effect of specific robot dimensions on stability and maneuverability [60]. More specifically, the effect of center of mass (COM) position on aggressive cornering maneuvers was assessed. They found that a COM placed behind the center of the drive wheels was best for aggressive corner maneuvers. It also produced less tracking errors (suggesting greater inherent stability for aggressive cornering maneuvers), quicker lap times, and a smaller change in motor saturation. However, agricultural over-arch DDMRs will not be making aggressive cornering maneuvers, so the study is of little use. Another study was done regarding the point of reference for a 3DOF robot [2]. A DDMR was connected to a trolley (Figure 2.1) and then tested (on different trajectories) with the trajectory navigation/reference point positioned at different locations on the DDMR-Trolley vehicle. It was tested with the reference point at the trolley COM (green dot) and combined COM (blue dot).

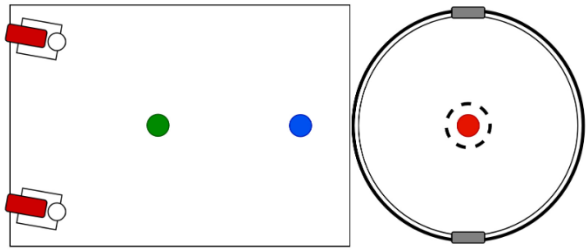

Figure 2.1: *DDMR connected to a trolley [2]. Red dot = COM of DDMR, green dot = COM of trolley, and blue dot = com of trolley and DDMR combined.*

Changes in drive torques required were analysed at the two different reference points. However, the 3DOF nature of the DDMR-Trolley vehicle removed the usefulness of the study. The third degree of freedom comes from the rotation of the DDMR relative to the trolley (Figure 2.2).

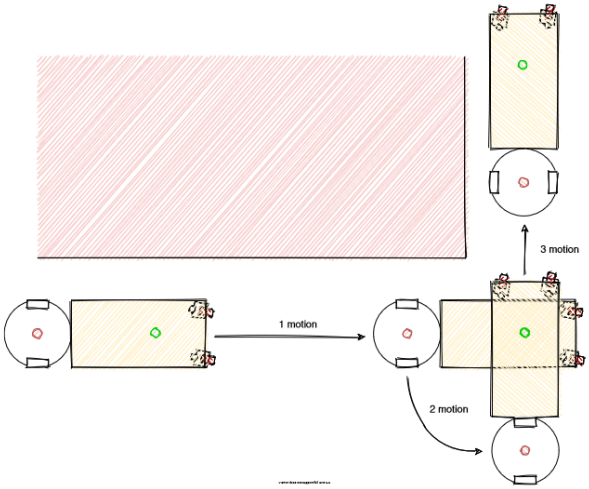

Figure 2.2: *DDMR-Trolley performing a maneuver [2].*

Wheel chair stability tests were conducted by Ding et al [4], and it was found that shifting the COM closer to the drive wheels improved stability. This study is relevant because the effect of the COM position on stability is of interest. However, they only considered the COM position, and neglected other dimensions. A study conducted research into the effect of DDMR dimensions and turn radius on minimum path travelling time [61]. The dimensions of interest were wheel diameter and caster wheel distance (which is assumed to be the wheel base). However, reducing path traveled time is not of interest to the current study, and is of no use. Another study considered the effect of caster orientation on wheel chair turning resistance at two different caster trails [3]. Results show that caster orientation does indeed have an effect on turning resistance, and a smaller caster trail significantly increases turning resistance and therefore motor torque (Figure 2.3). However, the study could have gone into more detail and tested more caster trail values to build a more robust trend.

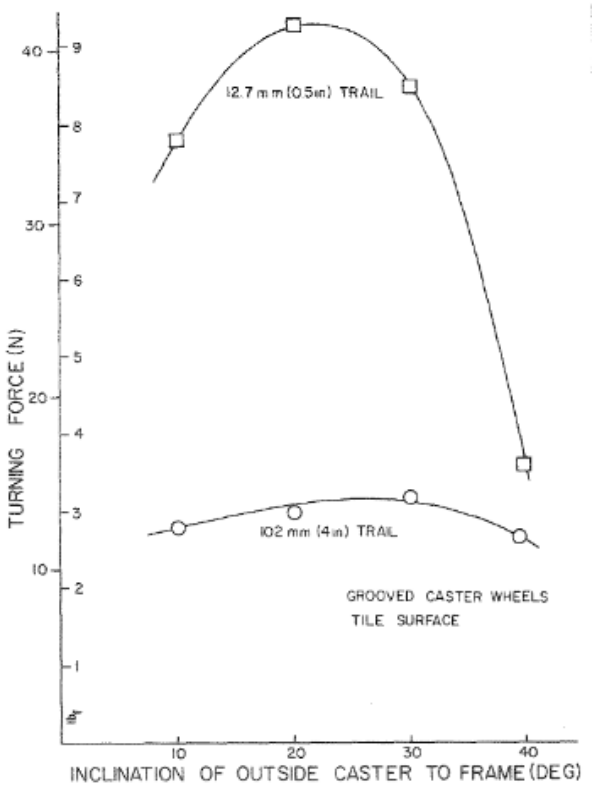

Figure 2.3: *Wheel chair turning force vs caster orientation at two different caster trails [3]*

One key aspect of the differential drive is the behaviour of the free running wheels, which in most cases are casters. The caster reaction forces depend on their orientation, and can cause erratic vehicle behaviour. Some studies have looked at the effect of caster orientation. One study considered the influence of caster orientation on powered wheelchair stability [4]. A powered wheel chair was driven backwards with the casters in different initial orientations (Figure 2.4). Errors in wheel chair trajectories were observed. It was also found that the speed of the wheelchair was an important factor. Higher speeds gave less directional divergence. A dynamic model of the wheel chair was also built which agreed with measured results. A model describing wheel chair stability was also successfully built by Babel and Guegan [46]. These studies are useful, but the effect of different caster trails (and other dimensions) were neglected.

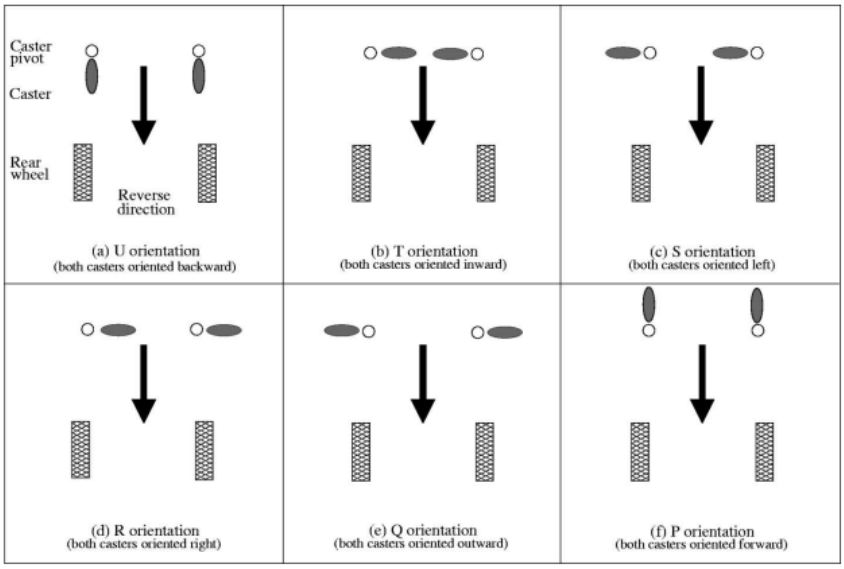

Figure 2.4: *Caster orientations tested [4].*

Another study analysed the effect of caster configuration on drive wheel torque [62]. It was found the having two casters at each end of the robot (4 casters) caused greater torque stability as opposed to one wheel at each end (2 casters), which suggests 4 casters are easier to control. This is useful when thinking about vehicle configuration, but not when optimising vehicle dimensions.

It is possible the reaction forces from the casters significantly resist the motion of the vehicle and may need to be accounted for in vehicle chassis design. If large enough, the reaction forces could cause the over-arch frame to splay outward or compress inward. The significance of caster reaction forces were assessed by Rajagopal and Barakat [63] and were found it to be negligible. However, the DDMR in the study was not at large scale, and large scale DDMRs are of chief interest in the current study. A study considered the motion of a gurney with four caster wheels [64]. It found that the main contributing factor regarding resistance to motion was the caster wheels, suggesting casters cannot be ignored. However, reaction forces on the frame were not specifically assessed. Another study modelled the motion of a gurney, and did model the caster reaction forces [65]. Unfortunately, the magnitudes of the forces applied to the frame were not included (just the overall motion on the gurney). Research has also been conducted into the turning and rolling resistance of different caster wheel types and sizes [66][67][68][69], but they do not

consider the effect of different caster trails on chassis loading. Lateral and longitudinal forces on wheel chair caster wheels were measured by VanSickle et al [70]. However, the data is not very useful as it is in very small magnitudes making it difficult to analyse, and the effect of increased caster trail was not considered. An interesting study was conducted on active caster wheels [71]. Part of the study focused on the effect of split/dual caster wheels on scrubbing torque, and it found that split/dual wheels reduced the reaction torque from the ground. This could be a useful way to reduce the effect of casters on vehicle motion, but is not of interest at this time. During research into caster stability, caster forces were measured, but they were only the normal forces [72]. Another study looked at the effect of caster trail and orientation on wheel chair turning resistance [3]. However, it did not analyse the caster reaction forces directly. Finally, lateral caster tire forces were measured by Ding et al [4], but the forces were not translated into the coordinates of the chassis, and the longitudinal forces of the caster tires were not measured. Also, caster trail was not taken account of. No useful studies exist on the effects of caster reaction forces on chassis loading. Studies include the casters when analysing overall motion, but specific reaction forces on the chassis are not studied, and variations of caster trail are ignored.

To accurately estimate chassis loading due to casters, the caster reaction force model needs to be a reasonable representation of reality. Plenty of caster models exist (generally as part of DDMR models) [65][4][38][73][37][33][74][75], but specific validation of the caster models needs to be done. Longitudinal and lateral forces and yaw moment were measured on a wheel chair wheel [75]. This was done by attaching the wheel to a swing arm and placing it onto a turn table such that it had a slip angle of $\pm 9^{\circ}$. However, the wheel was only tested across a small range of angles relative to the turn table, and casters are often at very different angles relative to the motion of the vehicle. Considering the lack of caster specific experiments, the search was widened to include automobile steering system models and experiments because steering systems do have a degree of caster trail (mechanical and pneumatic). Automobile tire and steering dynamics are a well studied topic. The magic tire formula model is an example of a well known and used tire model [76]. However, upon review, it is not clear these types of models/experiments are relevant

to free running casters wheels, because the degree of rotation for steered systems is much lower. Also, the steering angle of the wheels are most often dictated by the steering system, not the motion of the vehicle. The commonality between the two systems (steered and free running caster) likely lies in aligning torques. However, automobile steering models are complex with many parameters, and it is better to validate and use a simpler free running caster wheel model. So, automobile steering models are not useful for the current study. To the authors knowledge no experiments have been conducted to specifically validate a free running caster wheel model in literature.

Longitudinal chassis deformation was an issue observed in vehicles designed at the University of Waikato. Therefore, and understanding of the forces being applied to the frame by the power train is important. Research in this area is lacking. Finite element analysis was performed on an over-arch chassis to determine its suitability for maximum load [26]. However, the drive forces from the power train and caster reaction forces were not considered. Something similar was done for a pineapple picking vehicle [30], but it also did not consider drive/reaction forces on the frame. A more relevant chassis optimisation study has been done [77], where static and dynamic stress analysis was performed on a chassis for a blueberry harvesting vehicle. The dynamic analysis took into account chassis deformation due to uneven surfaces. However, stress and deflection of a over-arch chassis due to vertical loads is not of particular interest at this time.

Another key factor to consider for the optimisation of DDMRs is the effect of a sloped working environment. A study focused on wheel slip detection did consider slope in its dynamic model [40], but it did not consider physical optimisation of vehicle for improved performance on a slope. Another study focused on controlling a wheel chair on a slope [78], but is not useful because the wheel chair itself was not adjusted to improve performance. Larry Crichlow built a comprehensive wheel chair simulator that takes into account sloped environments [73], but again, no optimisation was conducted. Research was conducted into the stability of different vehicle configurations on slopes [5], and it was found that a three wheeled vehicle was the least stable (Figure 2.5, second from left). A four-wheeled articulated vehicle was found to be the most stable (Figure 2.5, far right). These results could be used to select the ideal wheel configuration for a more standard chassis design,

but it is not particularly useful for over-arch differential drive vehicles. Another study focused on modelling a powered wheel chair while considering slipping and gravitational disturbances [42], but it is more focused on control than physical optimisation.

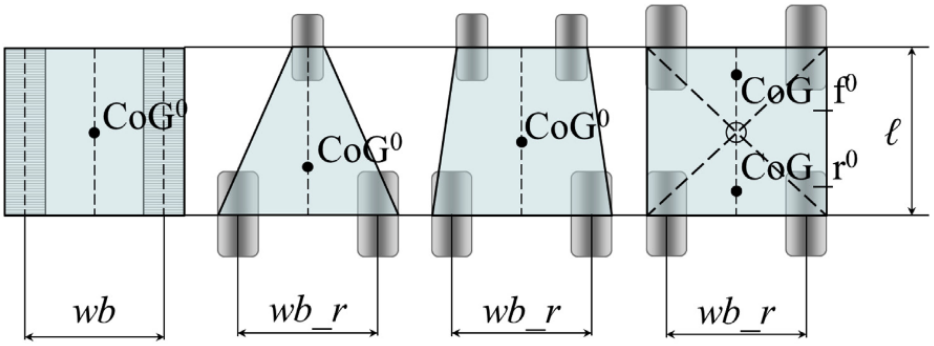

Figure 2.5: *Vehicle configurations tested in sloped environments [5].*

Energy consumption is an important aspect to consider when optimising any vehicle because it affects run times between refueling/recharging and the cost of operation. Manufacturing costs are also higher if more batteries are required. A study aimed to reduce energy consumption of a DDMR through improved controller design [79], and was successful. However, improvements were not make through optimisation of vehicle dimensions. Another study looked at energy consumption [80], but again was not done through vehicle optimisation. Research was conducted into energy consumption with regards to tracking accuracy [81]. This is not useful because it does not consider vehicle dimensions. Mauricio Jaramillo-Morales, Sedat Dogru and Lino Marques conducted research into energy reduction via optimisation of vehicle speed profiles [82]. It could be useful to do this for DDMRs in agriculture to help increase vehicle battery replacement/recharge intervals, but it is not of direct importance to the current study.

Many of the studies discussed have been focused on wheels chairs, which at first glance may remove their relevance. However, wheel configurations of wheel chairs are typically identical to DDMRs giving good reason to investigate them.

2.4 Summary

Dimensional optimisation of DDMRs has been for the most part neglected in literature. Work has been done to understand the influence of casters on vehicle behaviour but optimisation has been ignored, and to the authors knowledge, no dedicated experiment to validate caster reaction forces exists. Slope has been accounted for in dynamics models but optimisation for a sloped working environment needs to be done. Lastly, little research has been conducted regarding loads applied to over-arch chassis and requires more work. Therefore, a great opportunity exists to widen the field of agricultural over-arch vehicle dynamics and fill the gaps discovered in this review. A dynamic model of an over-arch DDMR will now be built so that questions raised from reviewing literature can be answered. The main question raised from the literature review is: Do variations in vehicle dimensions have a significant impact on over-arch DDMR performance?

Specific Research Questions:

- How do variations in the dimensions of a DDMR significantly affect peak drive forces, and is it important to keep chassis width constant while increasing drive wheel track width?
- Do some dimension values produce less energy consumption compared to others, and is the difference significant?
- Are loads on an over-arch chassis significantly influenced by dimensions?
- Do caster trail and the lateral position of the COM have an effect on vehicle stability, and is it better to have the casters and COM trailing or leading on a forward trajectory?
- Do large scale vehicles show more sensitivity to dimensional changes than small scale vehicles?

Chapter 3

Kinematics and Dynamics of an Over-arch Differential Drive Vehicle

This chapter outlines the development of the dynamic model used to investigate the dimensional sensitivity of over-arch DDMRs. It starts by building necessary kinematics after which the dynamic model is constructed. The model includes slope forces, dynamic normal forces, caster forces and chassis loading. Changes in drive wheel and caster tire contact patch size is also included, as well as rolling resistances. Vehicle suspension is ignored because it is assumed to have minimal affect on dimensional sensitivity.

3.1 Kinematic Model

This section develops the kinematics needed to build a dynamic model of a DDMR. First of all, it is necessary to consider the relationship between reference frame 1, the inertial frame (x_1, y_1), and reference frame 2, the vehicle frame (x_2, y_2) (Figure 3.1). Point A in reference frame 2, can be related to reference frame 1 via (3.1) [34].

$$\begin{bmatrix} x_1 \\ y_1 \end{bmatrix} = \begin{bmatrix} \cos(\theta_1) & -\sin(\theta_1) \\ \sin(\theta_1) & \cos(\theta_1) \end{bmatrix} \begin{bmatrix} x_2 \\ y_2 \end{bmatrix} \tag{3.1}$$

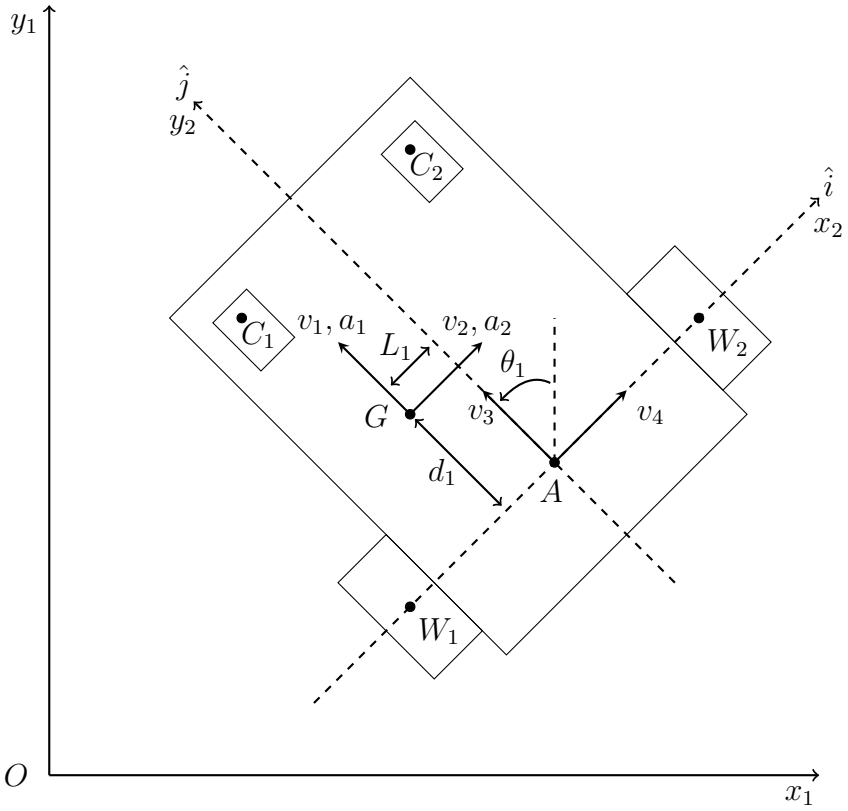

Figure 3.1: *Vehicle co-ordinate systems.*

As the center of mass (G) is relevant to the dynamic model, it also needs to be related to the inertial frame. The position and velocity of G in the inertial frame can be defined by (3.2) and (3.3) [4].

$$\begin{bmatrix} x_{1G} \\ y_{1G} \end{bmatrix} = \begin{bmatrix} \cos(\theta_1) & -\sin(\theta_1) \\ \sin(\theta_1) & \cos(\theta_1) \end{bmatrix} \begin{bmatrix} x_{2G} \\ y_{2G} \end{bmatrix} \tag{3.2}$$

$$\begin{bmatrix} \dot{x}_{1G} \\ \dot{y}_{1G} \end{bmatrix} = \begin{bmatrix} \cos(\theta_1) & -\sin(\theta_1) \\ \sin(\theta_1) & \cos(\theta_1) \end{bmatrix} \begin{bmatrix} v_2 \\ v_1 \end{bmatrix} \tag{3.3}$$

Computing (3.3) gives (3.4) and (3.5). By taking the derivatives, (3.6) and (3.7) are obtained, and when simplified they give (3.8) and (3.9) [4].

$$\dot{x}_{1G} = v_2 \cos\theta_1 - v_1 \sin\theta_1 \tag{3.4}$$

$$\dot{y}_{1G} = v_2 \sin\theta_1 + v_1 \cos\theta_1 \tag{3.5}$$

$$\ddot{x}_{1G} = (\dot{v}_2 \cos\theta_1 - v_2 \sin\theta_1 \dot{\theta}_1) - (\dot{v}_1 \sin\theta_1 + v_1 \cos\theta_1 \dot{\theta}_1) \tag{3.6}$$

$$\ddot{y}_{1G} = (\dot{v}_2 \sin\theta_1 + v_2 \cos\theta_1 \dot{\theta}_1) + (\dot{v}_1 \cos\theta_1 - v_1 \sin\theta_1 \dot{\theta}_1) \tag{3.7}$$

$$\ddot{x}_{1G} = (\dot{v}_2 - v_1 \dot{\theta}_1) \cos\theta_1 - (\dot{v}_1 + v_2 \dot{\theta}_1) \sin\theta_1 \tag{3.8}$$

$$\ddot{y}_{1G} = (\dot{v}_2 - v_1 \dot{\theta}_1) \sin\theta_1 + (\dot{v}_1 + v_2 \dot{\theta}_1) \cos\theta_1 \tag{3.9}$$

Now, by looking at the terms making up $\ddot{x}_{1G}$ and $\ddot{y}_{1G}$, it becomes clear that a_1 and a_2 are defined by equations (3.10) and (3.11) [4].

$$a_1 = \dot{v}_1 + v_2 \dot{\theta}_1 \tag{3.10}$$

$$a_2 = \dot{v}_2 - v_1 \dot{\theta}_1 \tag{3.11}$$

By inspection, v_2 only has a component from the rotation of the vehicle about the mid point between the drive wheels (A). This is due to the assumption that there is no lateral slip of the drive wheels [34][53]. Therefore, v_2 is defined by (3.12). v_1 is derived using L_1 and the linear and angular velocities of the vehicle (3.13).

$$v_2 = -d_1 \dot{\theta}_1 \tag{3.12}$$

$$v_1 = v_3 + L_1 \dot{\theta}_1 \tag{3.13}$$

Another kinematic property required for the dynamic model is the direction at which the king pins of the casters are moving (θ_7 and θ_8, see Figure 3.2) [38]. These directions are needed to calculate the reaction forces exerted on the DDMR chassis due to the casters [38]. The reaction forces are important because they affect the power and torque required from the drive train. Also, the reaction forces are of interest as they may cause significant

deformation of an over-arch vehicle chassis (depending on chassis stiffness). Magnitudes of velocities $\vec{v}_7$ and $\vec{v}_8$ are defined by (3.14) and (3.15) [83]. The angles θ_7 and θ_8 can be obtained by computing the $\hat{i}$ and $\hat{j}$ components of $\vec{v}_7$ and $\vec{v}_8$ and converting them into polar coordinates.

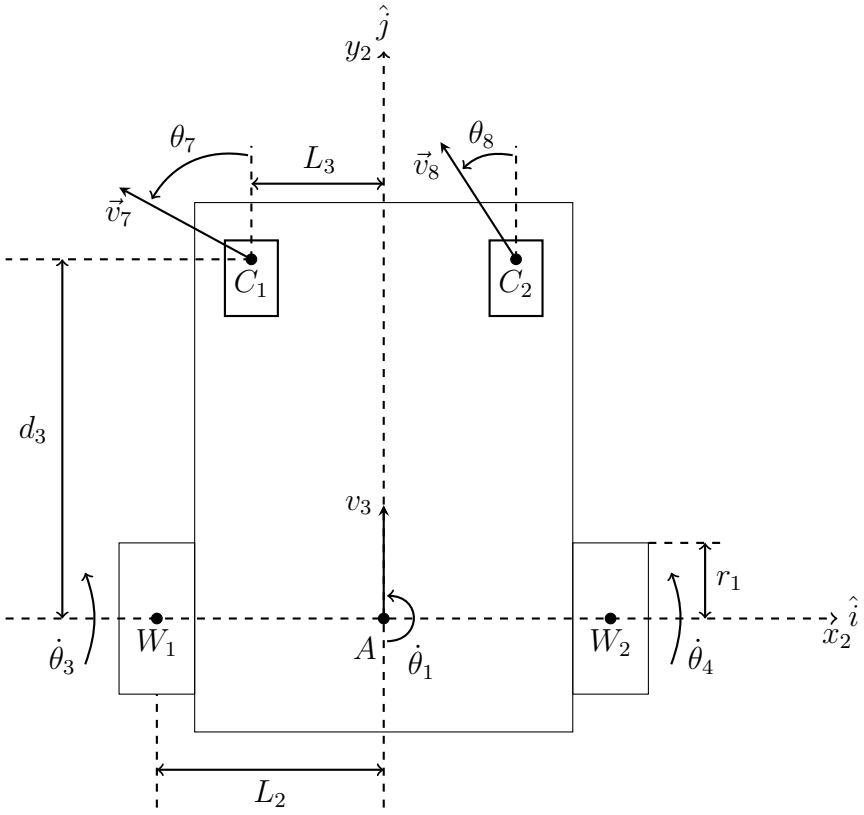

Figure 3.2: *Kinematic diagram of DDMR.*

$$||\vec{v}_7|| = \sqrt{(v_3 - L_3\dot{\theta}_1)^2 + (d_3\dot{\theta}_1)^2} \tag{3.14}$$

$$||\vec{v}_8|| = \sqrt{(v_3 + L_3\dot{\theta}_1)^2 + (d_3\dot{\theta}_1)^2} \tag{3.15}$$

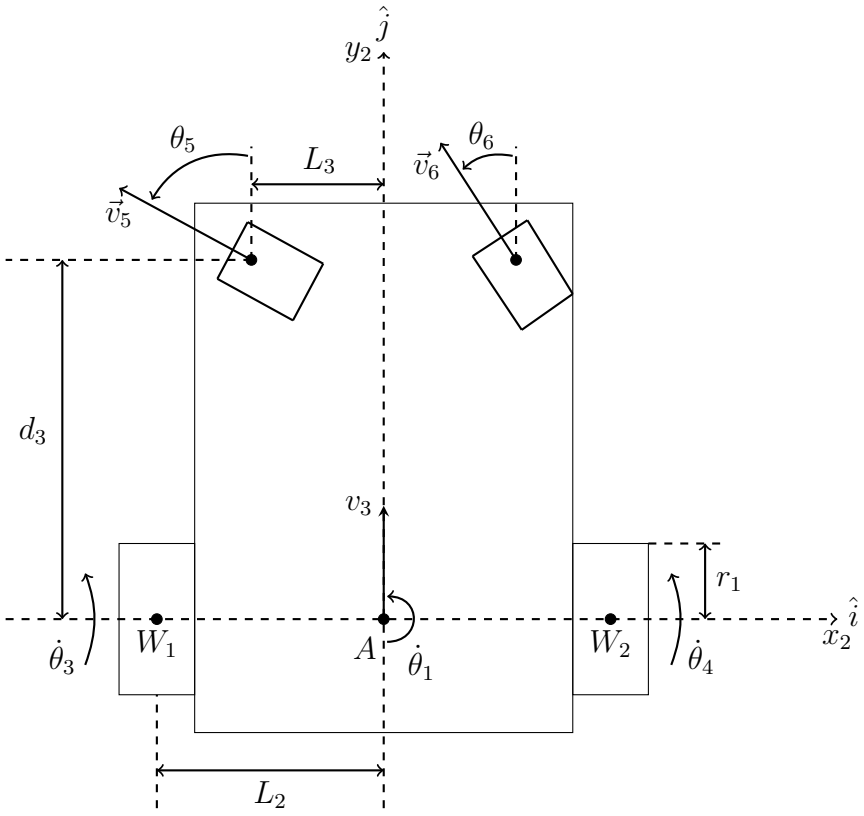

Figure 3.3: *Instantaneous caster orientation.*

In order to find the directions in which the ground reaction forces are acting on the casters, the difference between the king pin directions (θ_7 and θ_8) and instantaneous caster orientations (θ_5 and θ_6, Figure 3.3) needs to be found [38]. To do this, one must obtain θ_5 and θ_6. These can be found using (3.16) and (3.17) [47]. It should be noted that there are initial conditions where the motions of the casters cannot be determined. For example, if the casters are rotated 180 ° (θ_5 and $\theta_5 = \pi$) and the vehicle is driven directly forwards ($0 < v_3$ and $\dot{\theta}_1 = 0$), it is not possible to predict the directions of $\dot{\theta}_5$ and $\dot{\theta}_6$.

$$\theta_5 = \int \left(\frac{\dot{\theta}_1}{d_4}(d_3 \cos(\theta_5) + L_3 \sin(\theta_5) - d_4) - \frac{v_3}{d_4} \sin(\theta_5) \right) \tag{3.16}$$

$$\theta_6 = \int \left(\frac{\dot{\theta}_1}{d_4}(d_3 \cos(\theta_6) - L_3 \sin(\theta_6) - d_4) - \frac{v_3}{d_4} \sin(\theta_6) \right) \tag{3.17}$$

Finally, the last important kinematic property for the dynamic model is the linear and angular velocities and accelerations of the drive wheels. The angular velocities and

accelerations of the left and right drive wheels ($\dot{\theta}_3$, $\dot{\theta}_4$, $\ddot{\theta}_3$ and $\ddot{\theta}_4$) are expressed by (3.18), (3.19), (3.22) and (3.23). Linear velocities and accelerations are found using (3.20), (3.21), (3.24) and (3.25)

$$\dot{\theta}_3 = \frac{v_3}{r_1} - \frac{L_2}{r_1}\dot{\theta}_1 \tag{3.18}$$

$$\dot{\theta}_4 = \frac{v_3}{r_1} + \frac{L_2}{r_1}\dot{\theta}_1 \tag{3.19}$$

$$v_9 = v_3 - L_2\dot{\theta}_1 \tag{3.20}$$

$$v_{10} = v_3 + L_2\dot{\theta}_1 \tag{3.21}$$

$$\ddot{\theta}_3 = \frac{\dot{v}_3}{r_1} - \frac{L_2}{r_1}\ddot{\theta}_1 \tag{3.22}$$

$$\ddot{\theta}_4 = \frac{\dot{v}_3}{r_1} + \frac{L_2}{r_1}\ddot{\theta}_1 \tag{3.23}$$

$$a_9 = \dot{v}_3 - L_2\ddot{\theta}_1 \tag{3.24}$$

$$a_{10} = \dot{v}_3 + L_2\ddot{\theta}_1 \tag{3.25}$$

3.2 Dynamic Model

This section develops a dynamic model to describe the motion of a DDMR and the forces applied to an over-arch chassis during said motion. Figure 3.4 shows all the relevant forces and accelerations of the system in the x_2y_2 plane. Ding et al, Aylor and John, Dhaouadi et al, and DeSantis were the main authors consulted to build this model [4][38][34][53].

3.2.1 High Level Vehicle Model

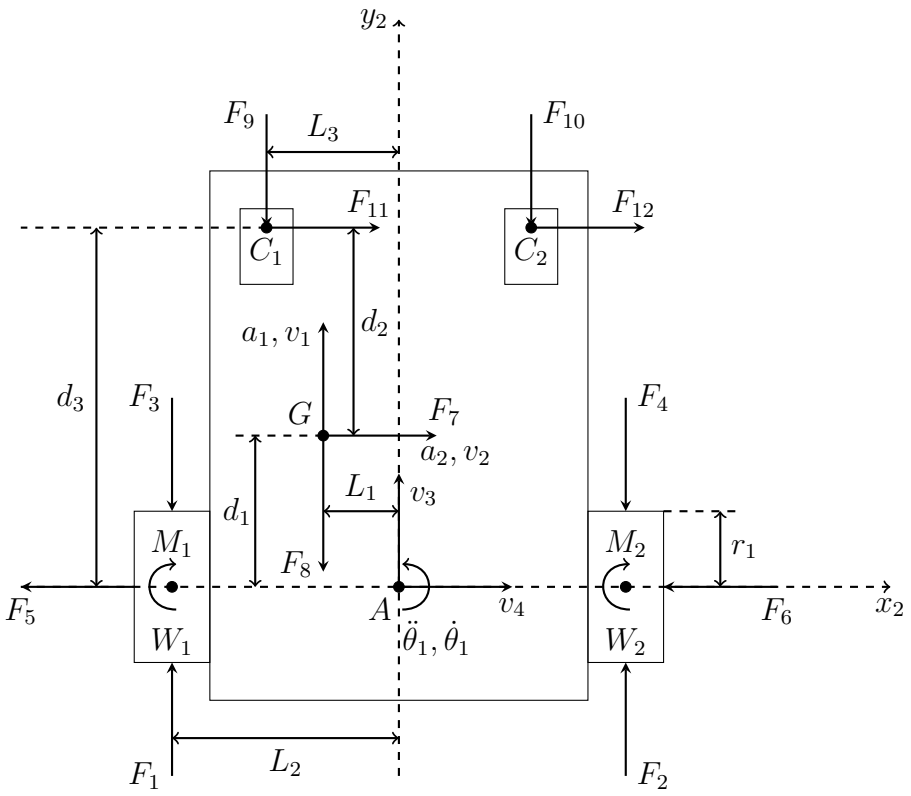

Figure 3.4: *Free Body Diagram of DDMR.*

The sum of the longitudinal forces acting on the DDMR are described by (3.26). Substituting (3.10) for a_1, (3.13) for v_1, and (3.12) for v_2 gives (3.28). Rearranging for $\dot{v}_3$ provides (3.29) which describes the longitudinal acceleration of point A.

$$m_G a_1 = F_1 + F_2 - F_3 - F_4 - F_9 - F_{10} - F_8 \tag{3.26}$$

$$m_G(\dot{v}_1 + v_2\dot{\theta}_1) = F_1 + F_2 - F_3 - F_4 - F_9 - F_{10} - F_8 \tag{3.27}$$

$$m_G(\dot{v}_3 + L_1\ddot{\theta}_1 - d_1\dot{\theta}_1^2) = F_1 + F_2 - F_3 - F_4 - F_9 - F_{10} - F_8 \tag{3.28}$$

$$\dot{v}_3 = \frac{F_1 + F_2 - F_3 - F_4 - F_9 - F_{10} - F_8}{m_G} + d_1\dot{\theta}_1^2 - L_1\ddot{\theta}_1 \tag{3.29}$$

The sum of moments around point A is found using equation (3.30). Substituting in the kinematic equations for a_1, a_2, v_1 and v_2 gives (3.32). Rearranging for $\ddot{\theta}_1$ provides (3.35).

$$\begin{aligned} I_G\ddot{\theta}_1 + m_G a_2 d_1 - m_G a_1 L_1 = (F_2 - F_1)L_2 + (F_3 - F_4)L_2 \\ +(F_9 - F_{10})L_3 - F_7 d_1 - F_8 L_1 - (F_{11} + F_{12})d_3 - M_1 - M_2 \end{aligned} \tag{3.30}$$

$$\begin{aligned} I_G\ddot{\theta}_1 + m_G(\dot{v}_1 + v_2\dot{\theta}_1)d_1 - m_G(\dot{v}_2 - v_1\dot{\theta}_1)L_1 = (F_2 - F_1)L_2 + (F_3 - F_4)L_2 \\ +(F_9 - F_{10})L_3 - F_7 d_1 - F_8 L_1 - (F_{11} + F_{12})d_3 - M_1 - M_2 \end{aligned} \tag{3.31}$$

$$\begin{aligned} I_G\ddot{\theta}_1 + m_G(\dot{v}_3 + L_1\ddot{\theta}_1 - d_1\dot{\theta}_1^2)d_1 - m_G(-d_1\ddot{\theta}_1 - v_3\dot{\theta}_1 - L_1\dot{\theta}_1^2)L_1 = (F_2 - F_1)L_2 \\ +(F_3 - F_4)L_2 + (F_9 - F_{10})L_3 - F_7 d_1 - F_8 L_1 - (F_{11} + F_{12})d_3 - M_1 - M_2 \end{aligned} \tag{3.32}$$

$$\begin{aligned} \ddot{\theta}_1(I_G + m_G L_1^2 + m_G d_1^2) + m_G\dot{v}_3 L_1 + m_G v_3 d_1\dot{\theta}_1 = (F_2 - F_1)L_2 + (F_3 - F_4)L_2 \\ +(F_9 - F_{10})L_3 - F_7 d_1 - F_8 L_1 - (F_{11} + F_{12})d_3 - M_1 - M_2 \end{aligned} \tag{3.33}$$

$$\begin{aligned} \ddot{\theta}_1(I_G + m_G L_1^2 + m_G d_1^2) = (F_2 - F_1)L_2 + (F_3 - F_4)L_2 + (F_9 - F_{10})L_3 - F_7 d_1 \\ -F_8 L_1 - (F_{11} + F_{12})d_3 - M_1 - M_2 - m_G\dot{v}_3 L_1 - m_G v_3 d_1\dot{\theta}_1 \end{aligned} \tag{3.34}$$

$$\begin{aligned} \ddot{\theta}_1 = \frac{((F_2 - F_1)L_2 + (F_3 - F_4)L_2 + (F_9 - F_{10})L_3 - F_7 d_1 - F_8 L_1)}{(I_G + m_G L_1^2 + m_G d_1^2)} \\ -\frac{((F_{11} + F_{12})d_3 + M_1 + M_2 + m_G\dot{v}_3 L_1 + m_G v_3 d_1\dot{\theta}_1)}{(I_G + m_G L_1^2 + m_G d_1^2)} \end{aligned} \tag{3.35}$$

F_1 can be found by Rearranging (3.29), giving (3.36). Substituting this into (3.35), one can solve for F_2 (3.37). So, the linear and angular accelerations of the vehicle, and the forces required by the drive wheels have been defined. Next, the reaction forces exerted on the vehicle from the drive wheels and casters need to be found. Gravitational forces and normal forces are also not yet defined.

$$F_1 = m_G(\dot{v}_3 + L_1\ddot{\theta}_1 - d_1\dot{\theta}_1^2) - F_2 + F_3 + F_4 + F_9 + F_{10} + F_8 \tag{3.36}$$

$$\begin{aligned} F_2 = &\frac{\ddot{\theta}_1(I_G + m_G L_1^2 + m_G d_1^2) - (F_3 - F_4)L_2 - (F_9 - F_{10})L_3 + F_7 d_1}{2L_2} \\ &+ \frac{F_8 L_1 + (F_{11} + F_{12})d_3 + m_G \dot{v}_3 L_1 + m_G v_3 d_1 \dot{\theta}_1 + M_1 + M_2}{2L_2} \\ &+ \frac{m_G(\dot{v}_3 + L_1\ddot{\theta}_1 - d_1\dot{\theta}_1^2) + F_3 + F_4 + F_9 + F_{10} + F_8}{2} \end{aligned} \tag{3.37}$$

m_G = total mass of vehicle (kg)
I_G = rotational inertial of vehicle about G (kgm^2)
$\ddot{\theta}_1$ = angular acceleration of vehicle (rad/s^2)
F_1 = drive force on left drive wheel (N)
F_2 = drive force on right drive wheel (N)
F_3 = reaction force (rolling resistance and inertia) on left drive wheel (N)
F_4 = reaction force on (rolling resistance and inertia) right drive wheel (N)
F_5 = lateral reaction force on left drive wheel (W_1) (N)
F_6 = lateral reaction force on right drive wheel (W_2) (N)
F_7 = lateral gravitational force due to the slope (N)
F_8 = longitudinal gravitational force due to the slope (N)
F_9 = longitudinal reaction force from left caster (C_1) (N)
F_{10} = longitudinal reaction force from right caster (C_2) (N)
F_{11} = lateral reaction force from left caster (C_1) (N)
F_{12} = lateral reaction force from right caster (C_2) (N)

$I_G + m_G L_1^2 + m_G d_1^2$ gives the rotational inertia about point A in kgm^2. The lateral reaction reaction forces on the drive wheels (F_5 and F_6) are not defined in this model, but they are not required as the vehicle is being analysed assuming zero lateral slip of the drive wheels.

3.2.2 Caster Model

A free body diagram of the casters can be seen in Figure 3.5. Summing the forces in the direction of y_2 and x_2 gives (3.38) to (3.41).

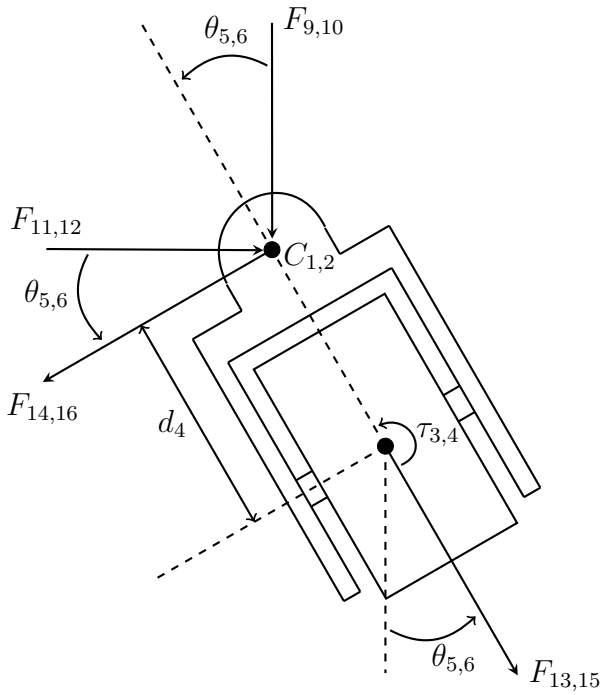

Figure 3.5: *Reactions forces on casters.*

$$F_9 = -F_{14}\sin\theta_5 - F_{13}\cos\theta_5 \tag{3.38}$$

$$F_{11} = F_{14}\cos\theta_5 - F_{13}\sin\theta_5 \tag{3.39}$$

F_{13} = reaction force from rolling resistance of tire (N)

F_{14} = reaction force generated from ground reaction torque (N) (see (3.42))

$$F_{10} = -F_{16}\sin\theta_6 - F_{15}\cos\theta_6 \tag{3.40}$$

$$F_{12} = F_{16}\cos\theta_6 - F_{15}\sin\theta_6 \tag{3.41}$$

F_{15} = reaction force from rolling resistance of tire

F_{16} = reaction force generated from ground reaction torque (N) (see (3.46))

The next step is to determine when forces F_{13} through F_{16} are activated and in which directions they act. This is determined by looking at the difference between the caster king pin velocity directions (θ_7 and θ_8) and the instantaneous caster positions (θ_5 and θ_6) (see Figure 3.6) [38]. Using the left caster (C_1) to explain, if both velocities are co-linear ($\theta_9 = 0$), then only F_{13} will be activated. If perpendicular ($\theta_9 = 90$), only F_{14} will be activated. In the scenario where they are neither co-linear or perpendicular ($0 < \theta_9 < 90$), both F_{13} and F_{14} will be activated. θ_9 is defined by (3.45). θ_5 and θ_7 have already been defined in section 3.1. So, F_{14} and F_{13} are defined by (3.42) and (3.43), and F_{16} and F_{15} are defined by (3.46) and (3.47). Ground reaction torques can be found using (3.44) and (3.48) [84].

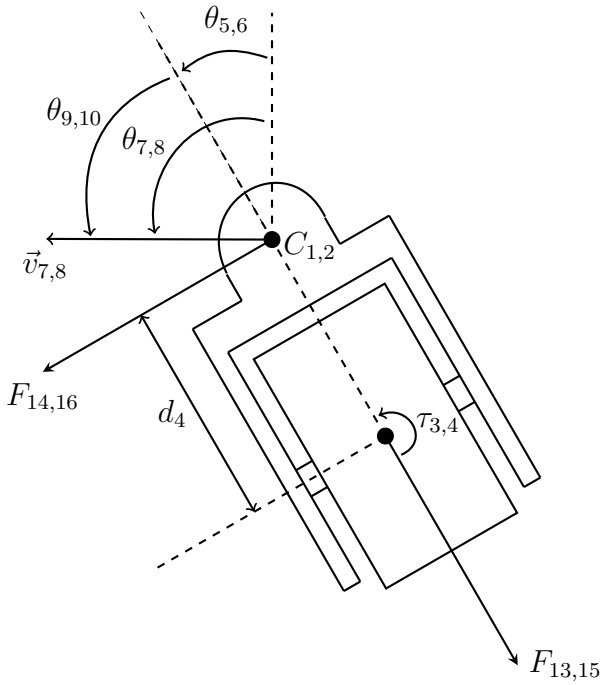

Figure 3.6: *King pin velocity vectors and instantaneous caster positions.*

$$F_{14} = \frac{\tau_3}{d_4} sgn(\sin\theta_9) \tag{3.42}$$

$$F_{13} = -N_3 k_2 sgn(\cos\theta_9) \tag{3.43}$$

$$\tau_3 = \frac{2\mu N_3^{1.5}}{3\sqrt{\pi p}} \tag{3.44}$$

$$\theta_9 = \theta_7 - \theta_5 \tag{3.45}$$

τ_3 = ground reaction torque (Nm)
μ = static coefficient of friction of tire on ground
k_2 = coefficient of rolling resistance of caster (assumed to be constant)
N_3 = Load on left caster (C_1) (N)
p = tire pressure (Pa)
$\vec{v}_7$ = king pin velocity of left caster (m/s)

$$F_{16} = \frac{\tau_4}{d_4} sgn(\sin\theta_{10}) \tag{3.46}$$

$$F_{15} = -N_4 k_2 sgn(\cos\theta_{10}) \tag{3.47}$$

$$\tau_4 = \frac{2\mu N_4^{1.5}}{3\sqrt{\pi p}} \tag{3.48}$$

$$\theta_{10} = \theta_8 - \theta_6 \tag{3.49}$$

τ_4 = ground reaction torque (Nm)
μ = static friction of tire on ground
k_2 = coefficient of rolling resistance of caster (assumed to be constant)
N_4 = Load on right caster (C_2) (N)
p = tire pressure (Pa)
$\vec{v}_8$ = king pin velocity of right caster (m/s)

The friction coefficient of a tire is different when it is rolling and turning simultaneously [85]. This variation of friction can be defined by (3.50) using a coefficient of friction (COF) of 0.7 for the zero velocity condition [85]. It is assumed that (3.50) is a good

approximation for the tires in the current study, and that the COF for zero velocity can be adjusted if needed without negatively effecting results. Therefore, this expression was used (with zero velocity COF adjusted accordingly) for the caster and drive wheel ground reaction torque friction coefficients.

$$\mu = f(v) = 0.4511e^{-0.4603|v|} + 0.2376 \tag{3.50}$$

μ = COF
v = running speed of tire (km/h)

The running speed $|v|$ for each caster wheel is a function of the king pin velocity ($v_{7,8}$) and the orientation of the caster tire relative to the king pin velocities ($\theta_{9,10}$) (see equations (3.51) and (3.52)). One thing to note about the caster model is that caster wheel inertia about all axes has been ignored due to the typical low mass of casters. Also, in the caster model it is assumed that caster tires never slip linearly in any direction.

$$||\vec{v}_5|| = |v_7 cos(\theta_9)| \tag{3.51}$$

$$||\vec{v}_6|| = |v_8 cos(\theta_{10})| \tag{3.52}$$

3.2.3 Drive Wheels

The current rotational inertial of the vehicle does not take into account the rotational inertial of the drive wheels. This is taken into account when calculating the reaction forces F_3 and F_4, and is done by considering the force required to accelerate the drive wheels based on rotational inertia. Assuming no slip, F_3 and F_4 are initially defined by (3.56) and (3.57).

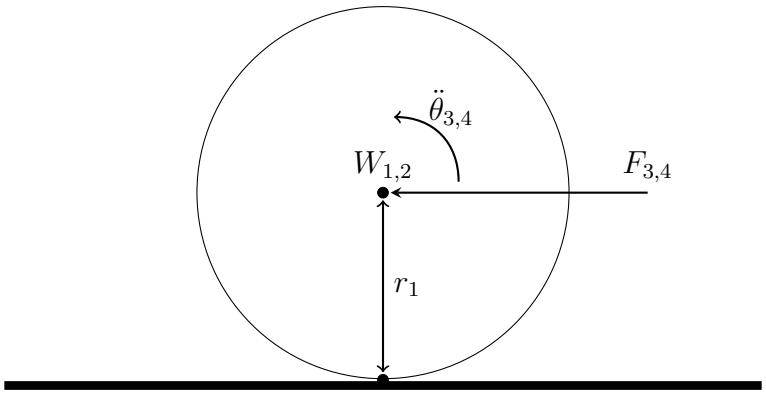

Figure 3.7: *Free body diagram of drive wheel.*

$$I_W \ddot{\theta}_3 = F_3 r_1 \tag{3.53}$$

$$\ddot{\theta}_3 = \frac{a_9}{r_1} \tag{3.54}$$

$$I_W (a_9 / r_1) = F_3 r_1 \tag{3.55}$$

$$F_3 = \frac{I_W a_9}{r_1^2} \tag{3.56}$$

$$F_4 = \frac{I_W a_{10}}{r_1^2} \tag{3.57}$$

$\ddot{\theta}_3$ = angular acceleration of left drive wheel (W_1) (rad/s^2)
I_W = rotational inertia of drive wheels (kgm^2)
a_9 = linear acceleration of left drive wheel (m/s^2)
r_1 = radius of drive wheels (m)
$\ddot{\theta}_4$ = angular acceleration of right drive wheel (W_2)
I_W = rotational inertia of drive wheels (kgm^2)
a_{10} = linear acceleration of right drive wheel (m/s^2)
r_1 = radius of drive wheels (m)

To complete the reaction forces on the drive wheels, rolling resistances and ground reaction torques need to be considered. Taking rolling resistance into account gives (3.58) and (3.59). Note, rolling resistance does increase with vehicle speed [86]. However, due to the expected low speeds of over-arch agricultural DDMRs, the coefficient of rolling resistance is assumed to be constant.

$$F_3 = \frac{I_W a_9}{r_1^2} + N_1 k_1 sgn(\dot{\theta}_3) \tag{3.58}$$

$$F_4 = \frac{I_W a_{10}}{r_1^2} + N_2 k_1 sgn(\dot{\theta}_4) \tag{3.59}$$

N_1 = load on left drive wheel (W_1) (N)
N_2 = load on right drive wheel (W_2) (N)
k_1 = coefficient of rolling resistance of drive wheels
$\dot{\theta}_3$ = angular velocity of left drive wheel (W_1) (rad/s)
$\dot{\theta}_4$ = angular velocity of right drive wheel (W_2) (rad/s)

Drive wheel ground reaction torques are described by equations (3.60) and (3.61). As it can be seen, these are calculated in a similar way to τ_3 and τ_4, and also take into account equation (3.50).

$$M_1 = \frac{2\mu N_1^{1.5}}{3\sqrt{\pi p}} sgn(\dot{\theta}_1) \tag{3.60}$$

$$M_2 = \frac{2\mu N_2^{1.5}}{3\sqrt{\pi p}} sgn(\dot{\theta}_1) \tag{3.61}$$

3.2.4 Normal Forces

Horizontal forces due to a slope and dynamic normal forces on the vehicle's wheels are also included in the model. Forces F_7 and F_8 depend on the orientation of the vehicle relative

to the slope (see Figures 3.8 and 3.9). If $\theta_1 = 0$ or 180, then $F_7 = m_G g sin\theta_2$ and $F_8 = 0$. If $\theta_1 = 90$ or 270, then $F_7 = 0$ and $F_8 = m_G g sin\theta_2$. Therefore, F_7 and F_8 can be defined by (3.66) and (3.62) respectively. The effect of linear and centripetal acceleration were included by using $-a_1$ and $-a_2$ and multiplying them by $M_G h_1$. (see equations (3.64) and (3.68)).

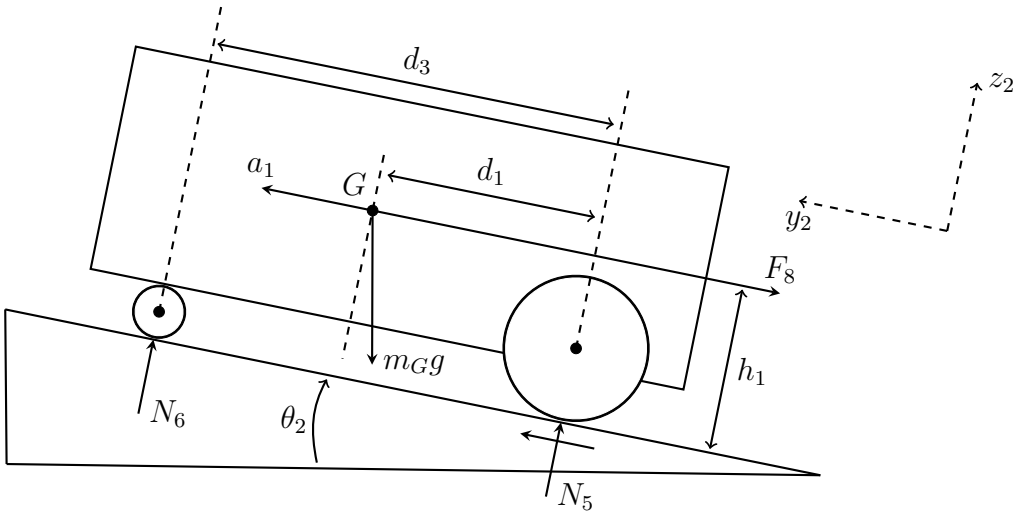

Figure 3.8: *Vehicle driving up a slope.*

$$F_8 = m_G g \sin\theta_2 \sin\theta_1 \tag{3.62}$$

$$N_5 + N_6 - m_G g \cos(\theta_2 \sin\theta_1) = 0 \tag{3.63}$$

$$N_6 = \frac{m_G g \cos(\theta_2 \sin\theta_1) d_1 - F_8 h_1 - m_G a_1 h_1}{d_3} \tag{3.64}$$

$$N_5 = m_G g \cos(\theta_2 \sin\theta_1) - \frac{m_G g \cos(\theta_2 \sin\theta_1) d_1 - F_8 h_1 - m_G a_1 h_1}{d_3} \tag{3.65}$$

N_5 = total normal load at rear of vehicle (N)

N_6 = total normal load at front of vehicle (N)

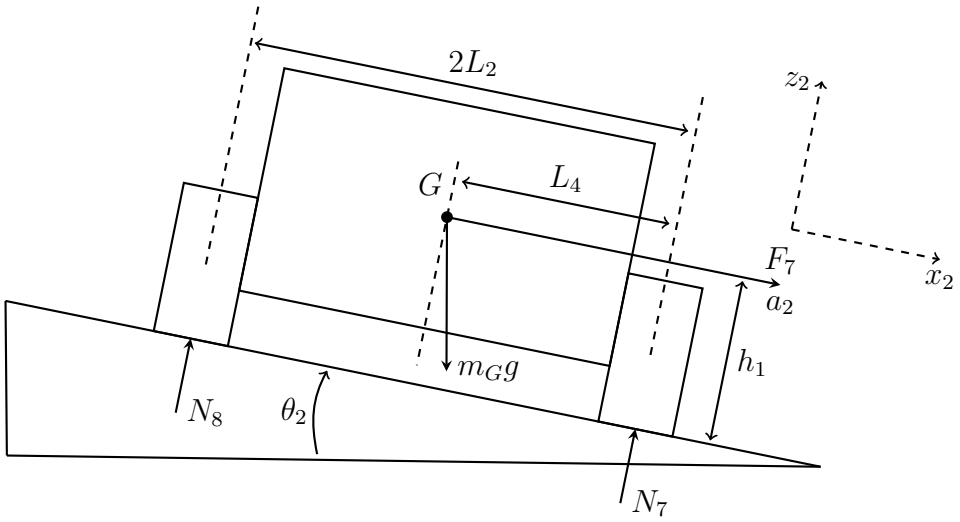

Figure 3.9: *Vehicle driving along a slope.*

$$F_7 = m_G g \sin\theta_2 \cos\theta_1 \tag{3.66}$$

$$N_7 + N_8 - m_G g \cos(\theta_2 \cos\theta_1) = 0 \tag{3.67}$$

$$N_8 = \frac{m_G g \cos(\theta_2 \cos\theta_1) L_4 - F_7 h_1 + m_G a_2 h_1}{2L_2} \tag{3.68}$$

$$N_7 = m_G g \cos(\theta_2 \cos\theta_1) - \frac{m_G g \cos(\theta_2 \cos\theta_1) L_4 - F_7 h_1 + m_G a_2 h_1}{2L_2} \tag{3.69}$$

N_7 = total normal load on right side of vehicle (N)

N_8 = total normal load on left side of vehicle (N)

Normal forces can be found using N_5, N_6, N_7 and N_8 (which are from equations (3.65), (3.64), (3.69) and (3.68) respectively) and plugging them into equations gives (3.70), (3.71), (3.72) and (3.73). This normal force model agrees with Doumiati et al [87]. It should be noted that for this model to be most accurate, the track width of the casters should be kept the same as the drive wheels ($2L_3 = 2L_2$) otherwise the model becomes statically indeterminate.

$$N_1 = \frac{N_5}{2} + \frac{N_8}{2} - \frac{m_G g}{4} \tag{3.70}$$

$$N_2 = \frac{N_5}{2} + \frac{N_7}{2} - \frac{m_G g}{4} \tag{3.71}$$

$$N_3 = \frac{N_6}{2} + \frac{N_8}{2} - \frac{m_G g}{4} \tag{3.72}$$

$$N_4 = \frac{N_6}{2} + \frac{N_7}{2} - \frac{m_G g}{4} \tag{3.73}$$

3.2.5 Over-arch Chassis Loading

To gain an understanding of shear forces acting on the vehicle chassis, the net drive forces on each side of the vehicle can be calculated using equations (3.74) and (3.75) (see Figure 3.10 for forces acting on the chassis).

$$\sum F_{y_2 L} = F_1 - F_3 - F_9 \tag{3.74}$$

$$\sum F_{y_2 R} = F_2 - F_4 - F_{10} \tag{3.75}$$

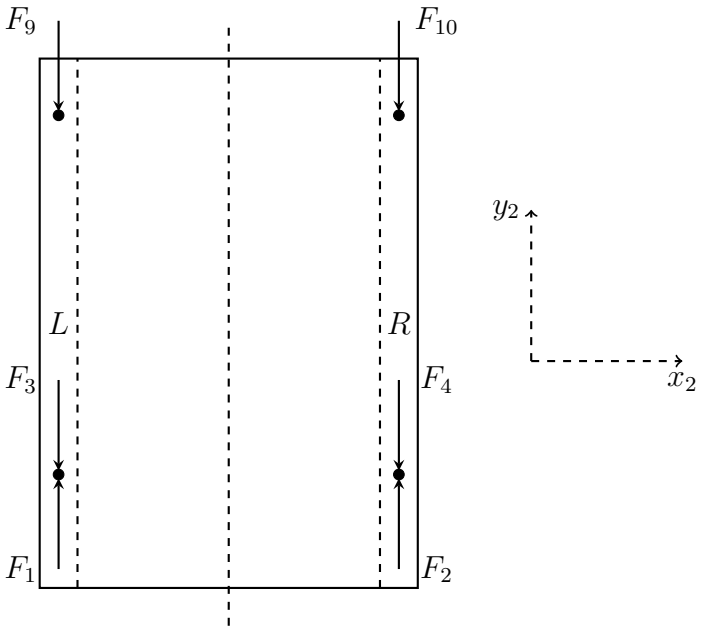

Figure 3.10: *Top down view of vehicle chassis with longitudinal forces shown.*

Total shear force on the frame can be found by taking half of the difference between the left and right net forces (see (3.77)). It is assumed that chassis stiffness is the same for both sides of the vehicle and that it is constant. An example of how results for F_{17} could be used in finite element analysis (FEA) can be seen in Figure 3.11. It is assumed that loads on the chassis due to the motion of the vehicle do not change the position of the centre of the chassis in the lateral direction x_2. Therefore, the chassis can be fixed in the centre during FEA, which allows symmetry to be used.

$$F_{17} = \sum F_{y_2 L} - \sum F_{y_2 R} \tag{3.76}$$

$$F_{17} = \frac{(F_1 - F_3 - F_9) - (F_2 - F_4 - F_{10})}{2} \tag{3.77}$$

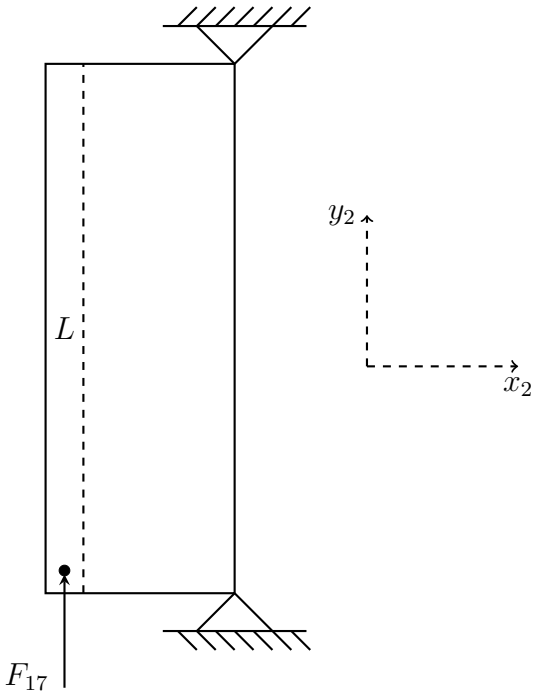

Figure 3.11: *Top down view of how the total shear force may be applied to the frame during FEA analysis.*

Lateral reaction forces on the drive wheels are assumed to be equal and in the same direction. Therefore, the only lateral reaction forces with potential to splay or compress the chassis are the lateral caster reaction forces F_{11} and F_{12} (Figure 3.12).

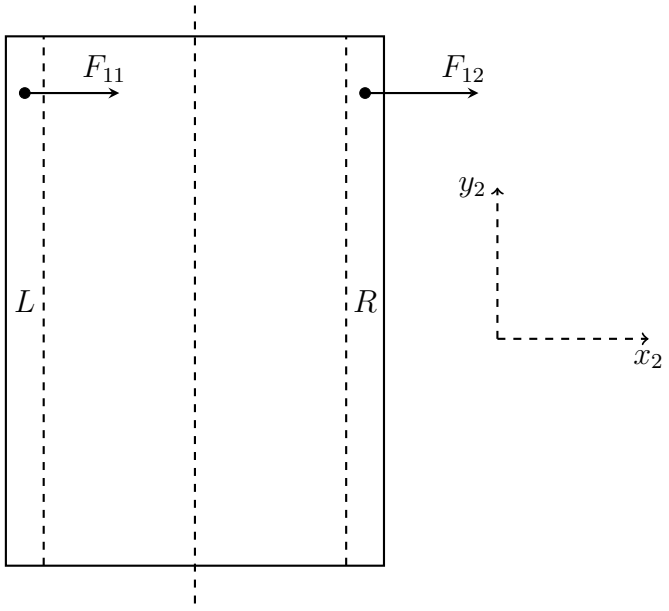

Figure 3.12: *Top down view of vehicle chassis with lateral caster reaction forces shown.*

If there is a difference between caster lateral forces (F_{11} and F_{12}), the two sides of vehicle will experience different amounts of deflection. A large difference between F_{11} and F_{12} ($0 << |F_{18}|$) means the chassis will be compressed or splayed significantly, depending on the stiffness of the chassis (see equation (3.78)). An example of how splay force F_{18} could be applied to the chassis during FEA can be seen in Figure 3.13. Like with the shear force, the centre of the chassis is assumed to be stationary in the lateral direction, meaning it can be fixed in the centre during FEA.

$$F_{18} = \frac{F_{11} - F_{12}}{2} \tag{3.78}$$

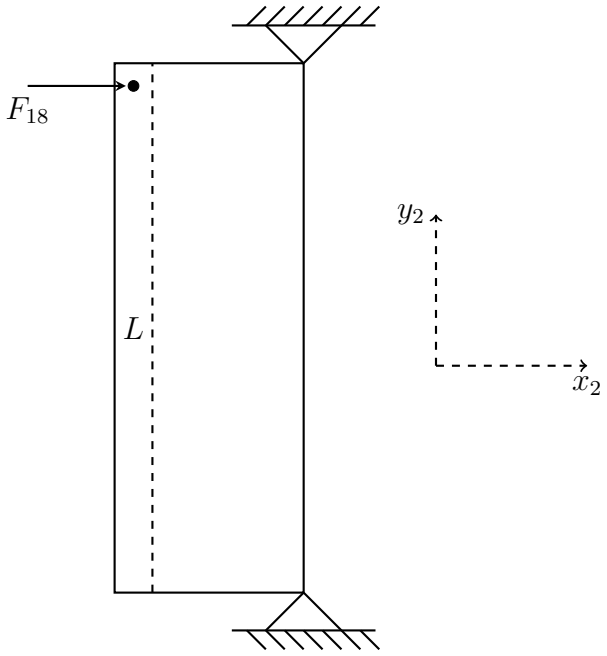

Figure 3.13: *Top down view of how the total splay force may be applied to the frame during FEA analysis.*

Note, even though the forces on the frame will induce chassis deflection, it is assumed that vehicle chassis is infinitely stiff for all simulations regarding dimensional sensitivity and stability etc. Actual chassis deflection will effect the motion of the vehicle but it is beyond the scope of this study and is not included.

3.2.6 Energy Consumption

Finally, the total energy consumption of the vehicle over the course of a trajectory is defined by equation (3.79).

$$E_{total} = \int_{t_0}^{t_1} (F_1 r\dot{\theta}_3 + F_2 r\dot{\theta}_4)\, dt \tag{3.79}$$

3.3 Model Summary

A dynamic model of an over-arch DDMR has now been defined including casters, position of the COM, normal forces, chassis loading, frictional forces, energy consumption, and chassis loading. The following chapter will asses the accuracy of the model.

Chapter 4

Dynamic Model Validation

To obtain useful information regarding the dynamics of DDMRs, the accuracy of the model needs to be assessed. In this chapter, the dynamic model is compared with motion software (Solidoworks Motion) as well as a test vehicle. One key aspect of this study is the validation of the caster reaction forces. An experiment is used to determine the accuracy of the mathematical approximation.

Section 4.1 discusses an experiment done to ascertain the accuracy of the caster model.

Section 4.2 compares a simplified version of the dynamical model to a model constructed in Soliworks Motion. The caster model is also compared with Solidworks Motion.

Section 4.3 discusses a field test conducted with a mid sized DDMR. The vehicle is driven on multiple trajectories and the results are compared to the dynamic model.

4.1 Caster Reaction Force Experiment

To ascertain the ability of the caster model to approximate reality, an experimental rig (Figures 4.1 and 4.3a) was designed and built to measure the longitudinal reaction force ($F_{9,10}$) and lateral reaction force ($F_{11,12}$) applied to the caster king pin.

4.1.1 Experimental Setup and Method

A stepper motor and ball screw were used to pull a carriage along two main linear rails. The caster assembly (Figure 4.3b) was attached to a sub carriage which was in turn attached to the main carriage via two sub rails (Figure 4.2). An encoder was placed at the top of the caster king pin to measure the angular rotation of the caster (Figures 4.4b and 4.4c). A load cell was connected between the two carriages to measure the reaction forces (Figures 4.2 and 4.4d). The main carriage was aligned in two configurations to measure $F_{11,12}$ and $F_{9,10}$ (Figures 4.4e and 4.4f). A folded sheet metal bar (call it a "weight bar") was placed on top of the caster to enable different loads to be applied. A thrust bearing was placed between the weight bar and caster mounting plate to minimise the contribution of the rotational inertia of the weights. An acrylic sheet was placed on the ground to provide a more consistent even surface for cleaner results.

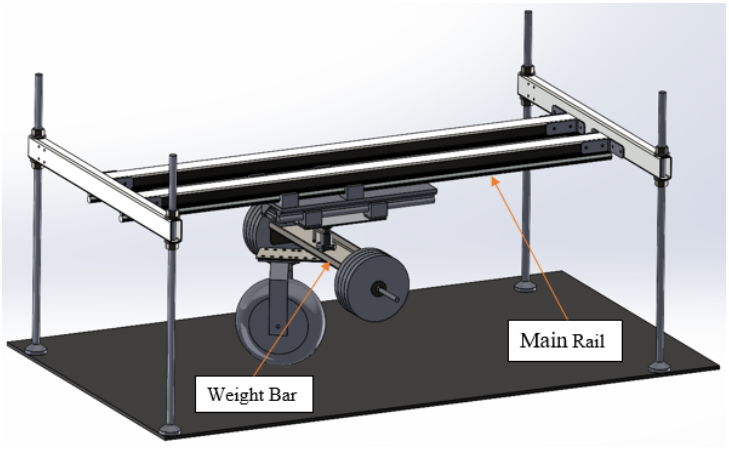

Figure 4.1: *CAD model of experimental rig.*

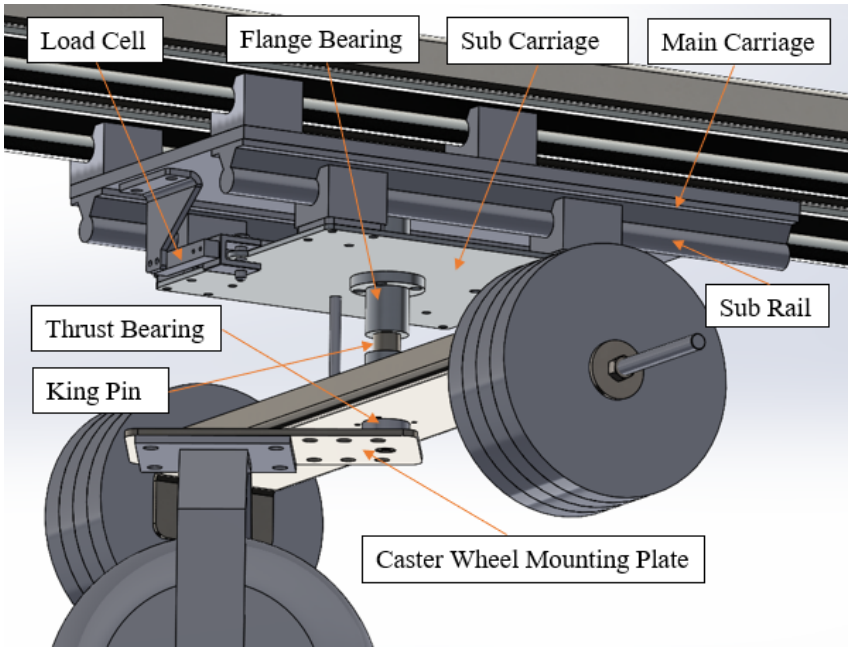

Figure 4.2: *CAD model of experimental rig, close up of components.*

(a) (b)

Figure 4.3: *Caster experiment photos, full rig (a) and caster assembly (b).*

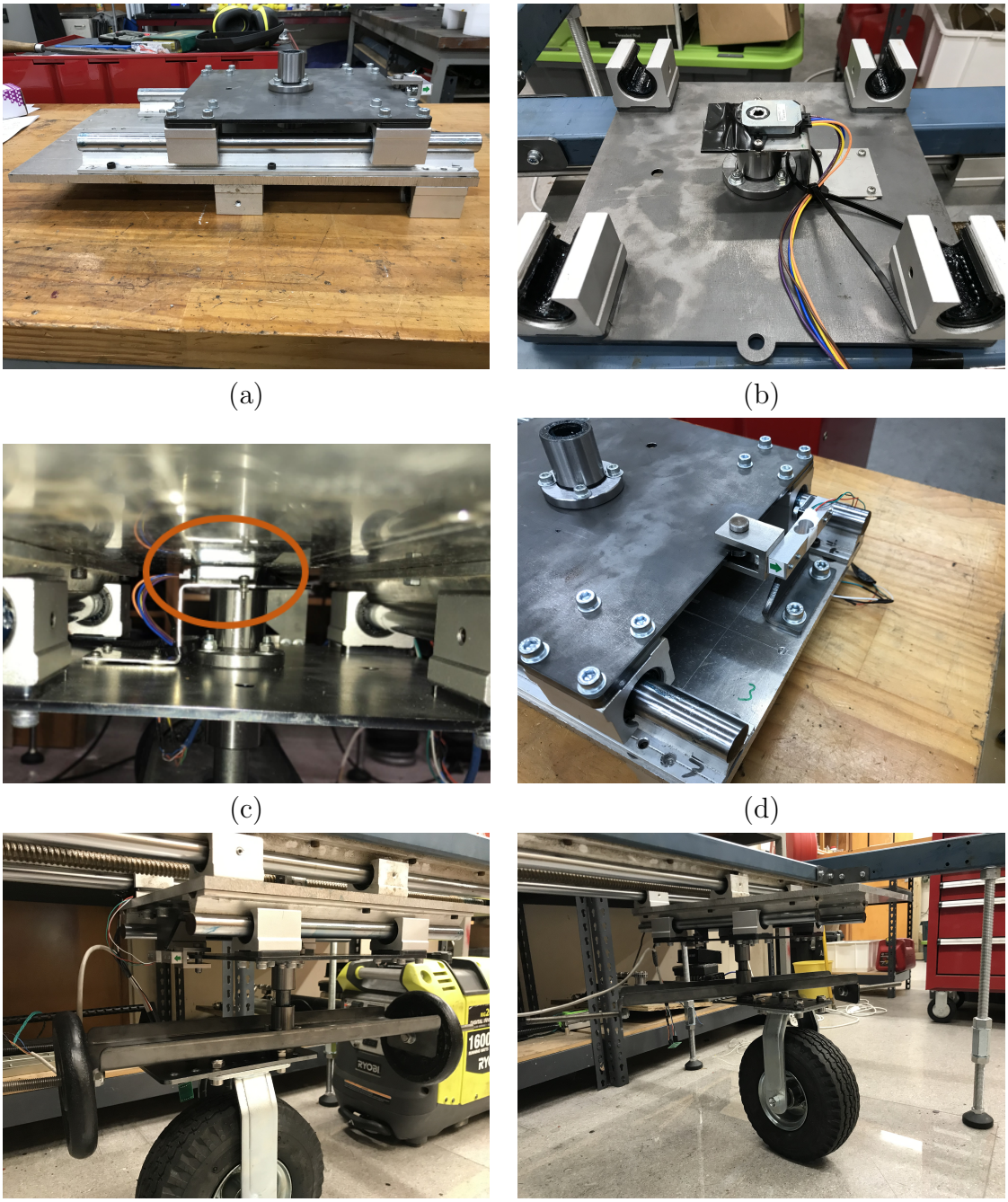

(a) (b) (c) (d) (e) (f)

Figure 4.4: *Caster experiment photos, main and sub carriage assembly (a), encoder mounted on sub carriage (b), encoder pushed up against underside of main carriage (c), load cell connected to main and sub carriage (d), sub carriage co-linear with main carriage to measure longitudinal reaction forces (e), and sub carriage perpendicular to main carriage to measure lateral reaction forces (f).*

The load cell was sampled at a rate of 80 Hz using an HX711 chip during the experiments, and was calibrated before the experiments began. Maximum load cell rating was 10 kg. An Arduino was used to read the chip and calculate the load in grams. The experiment was run in a total of 15 configurations for $F_{11,12}$ and $F_{9,10}$ in order to obtain all results of interest. Caster loads and trails for test configurations can be seen in table 4.1. Caster tire properties can be seen in table 4.2.

Table 4.1: Caster test configurations.

Configuration	N_c (N)	d_4 (m)
1	82.3	0.075
2	131.3	0.075
3	180.4	0.075
4	229.4	0.075
5	278.5	0.075
6	82.3	0.1
7	131.3	0.1
8	180.4	0.1
9	229.4	0.1
10	278.5	0.1
11	82.3	0.125
12	131.3	0.125
13	180.4	0.125
14	229.4	0.125
15	278.5	0.125

Table 4.2: Caster tire properties.

Radius (m)	Tire Pressure (Pa)	Dynamic COF	Coefficient of Rolling Resistance
0.125	55158	0.546	0.029

The dynamic coefficient of friction was estimated by locking the caster wheel and pulling it along the acrylic sheet. The COF was measured at three weights, 9.125, 11.625 and 14.125 kg, giving values of 0.578, 0.547 and 0.512 respectively, with an average of 0.546. Rolling resistance was estimated from the longitudinal reaction force plots in section 4.1.2.2 and Appendix A.

4.1.1.1 Lateral and Longitudinal Caster Reaction Forces

Measured and simulated lateral reaction forces were plotted against caster angle and time with a caster trail of 0.075 m and a caster load of 278.5 N. Plots were also constructed for caster loads of 82.3, 131.3, 180.4 and 229.4 N (see these plots in Appendix A). Note, because caster king pin motion is on the same vector as $F_{9,10}$, $\theta_{5,6} = \theta_{9,10}$. $\theta_{5,6}$ is the angle of the caster relative to the rig and $\theta_{9,10}$ is the difference between $\theta_{5,6}$ and the direction of the king pin velocity ($\theta_{7,8}$). Due to the fact the model cannot predict exactly when the caster will start turning (which in reality is based on inconsistencies of ground contact etc), the measured and simulated plots were shifted so the points at which both plots cross the horizontal axis are equal. Also, 180° of rotation is not consistently observed in the measured data because the caster had to be set with some initial angle to ensure it started rotating in a reasonable amount of time. The rig is not long enough to allow for very small initial caster angles.

4.1.1.2 Contact Patch Radius

The contact patch of the caster tire was investigated to see if the expected contact patch radius is a good approximation of reality. Equation (4.1) is an alternate version of (3.44) and is used to calculate expected contact patch radius (R) from the simulated torque ($\tau_{3,4}$), which is based on caster load and tire pressure. Actual torques can also be estimated with this equation using the measured contact patch radius.

$$\tau_{3,4} = \frac{2\pi\mu p R^3}{3} \tag{4.1}$$

4.1.1.3 Influence of Caster Trail on Peak Reaction Forces

Peak lateral and longitudinal reaction forces were also plotted against 3 different caster trails (0.075, 0.1 and 0.125m) at a caster load of 278.5 N to asses the influence of caster trail on reaction forces.

4.1.1.4 Instantaneous Caster Position

Caster angle vs time was measured during the experiments and was compared to the model at three different speeds. The speeds were 0.0095, 0.0122, and 0.025 m/s, and three samples were plotted from each speed along side the Simulink model.

4.1.2 Evaluation of Caster Reaction Forces

4.1.2.1 Initial Lateral Reaction Force

Upon inspection of Figure 4.5 and 4.6, lateral reaction forces match the model fairly well in the middle portion of the plots. A positive vertical offset can also be observed, with the absolute value of maximum negative magnitudes being lower than the maximum positive amplitudes. The average point at which peak lateral forces occur (based on Figures 4.5 and 4.6 and those in Appednix A) is at 165.5° and the force drops off steeply from there. The steep drop off towards the end of caster rotation is the relaxation of the tire as caster rotation slows to zero. The simulated force does not show this because it does not account for tire deflection during twisting. This is clear when Figure 4.6 is observed, because it can be seen that the force takes a long time to reduce after reaching it's peak value. Peak lateral forces occur near the point at which the caster rotation starts to slow

(at around 60 s). During the last 30-40s of the tests, caster rotation is at a minimum, allowing the deformed tire to relax as it rolls on the ground. The simulated force reduces instantaneously to zero and occurs much later but it stays at a higher value until it does so. The instantaneous drop in the model is due to the signum function in equations 3.42 and 3.46. The discontinuity at $\theta_{5,6} = 90°$ is due to the lateral force only being comprised of rolling resistance at $\theta_{5,6} = 90°$. This discontinuity is not observed as clearly in the measured data due to a loose connection between the load cell and the main carriage of the caster rig.

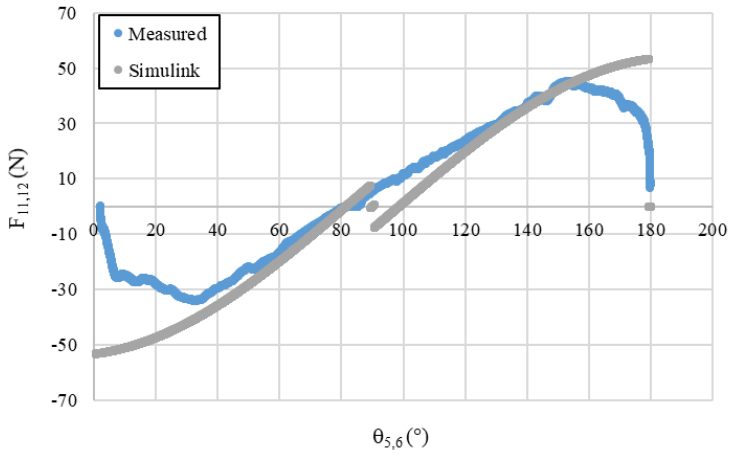

Figure 4.5: *Lateral reaction force vs caster angle @ 278.5 N of normal load.*

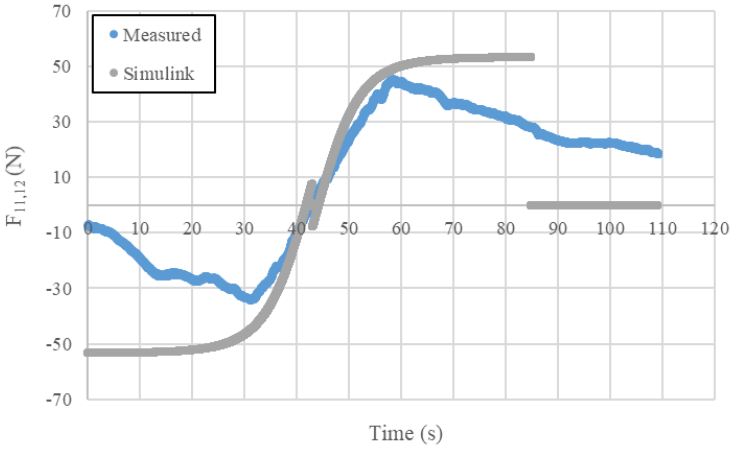

Figure 4.6: *Lateral reaction force vs time @ 278.5 N of normal load.*

4.1.2.2 Initial Longitudinal Reaction Force

The measured results for longitudinal reaction force show good agreement with the model but with a noticeably different peak force (Figures 4.7 and 4.8). Significant disagreement in peak reaction forces are observed for both lateral and longitudinal reaction forces across all caster loads and needs to be addressed.

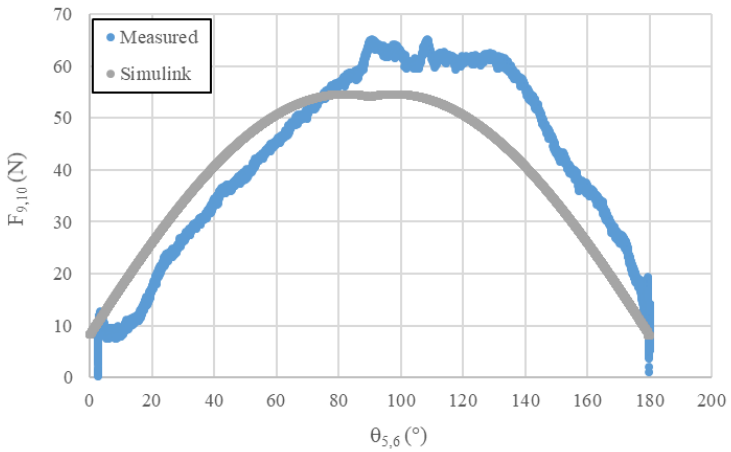

Figure 4.7: *Longitudinal reaction force vs caster angle @ 278.5 N of normal load.*

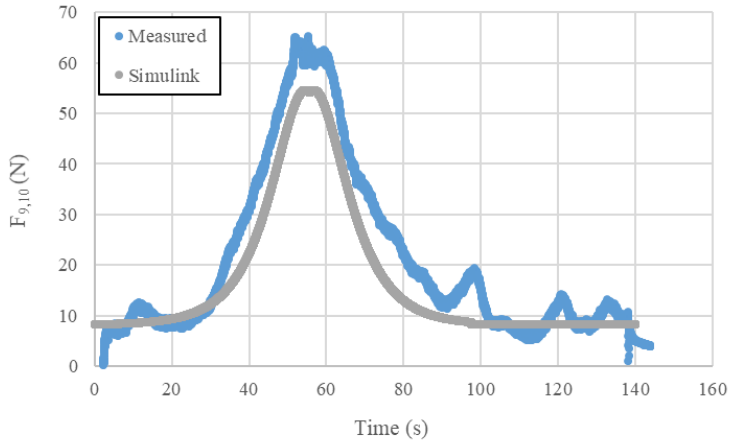

Figure 4.8: *Longitudinal reaction force vs time @ 278.5 N of normal load.*

4.1.2.3 Final Lateral Reaction Force

The force profile for the lateral forces shows a need for improvement. The instantaneous drop to zero does not match measured data (due to tire relaxation as discussed). To approximate the effect of tire relaxation, $F_{14,16}$ (the force required to overcome the ground reaction torque on the tire) is defined by a new function for $165.5° < \theta_{5,6} <= 180°$ and $0 <= \theta_{5,6} < 14.5°$ (see equation (4.2)). Let the angle describing these regions be called $\theta_{F_{11,12max}}$. With the boundaries described, $\theta_{F_{11,12max}} = 14.5°$ for the caster tire used in the experiment. Measured and simulated lateral reaction forces were plotted again but including the extra function (Figures 4.9 and 4.10). The measured and simulated forces match better with the extra function. However, the measured force eases off in a more linear fashion. There were some experimental results that do match the simulation better (Figures 4.11 and 4.12).

$$F_{14,16} = \frac{\tau_{3,4}}{d_4} \frac{|\sin(\theta_{5,6})|}{\theta_{F_{11,12max}}} sgn(\sin(\theta_{5,6})) \tag{4.2}$$

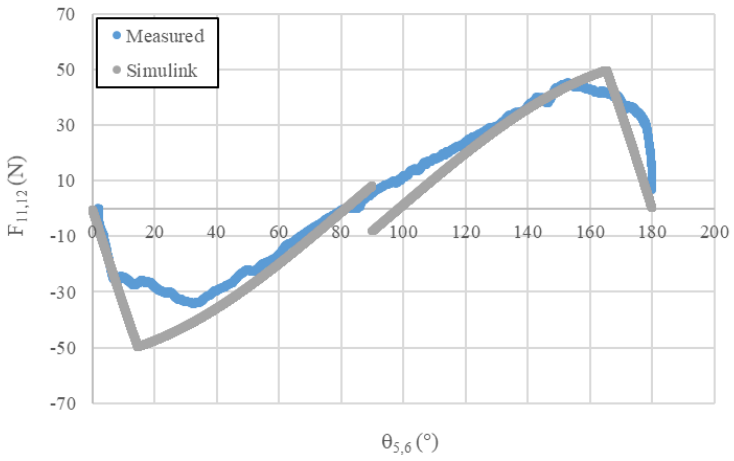

Figure 4.9: *Lateral reaction force vs caster angle @ 278.5 N of normal load with adjusted function.*

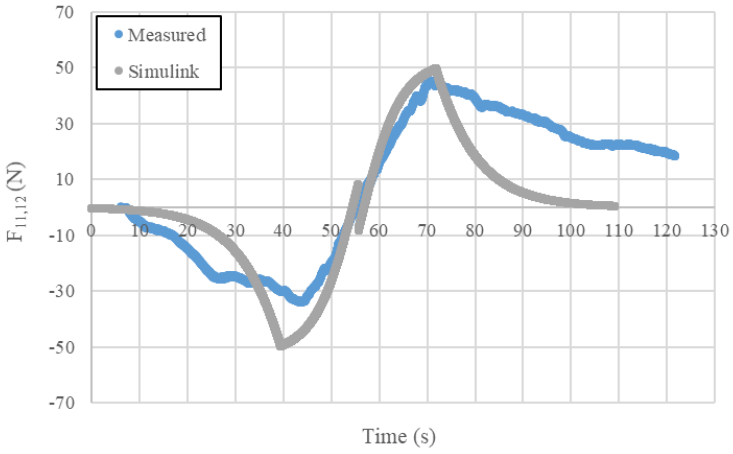

Figure 4.10: *Lateral reaction force vs time @ 278.5 N of normal load with adjusted function.*

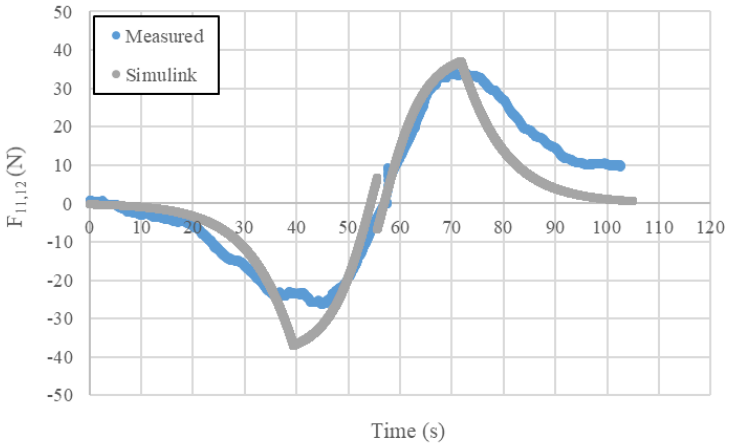

Figure 4.11: *Lateral reaction force vs time @ 229.4 N of normal load with adjusted function (example of better fit).*

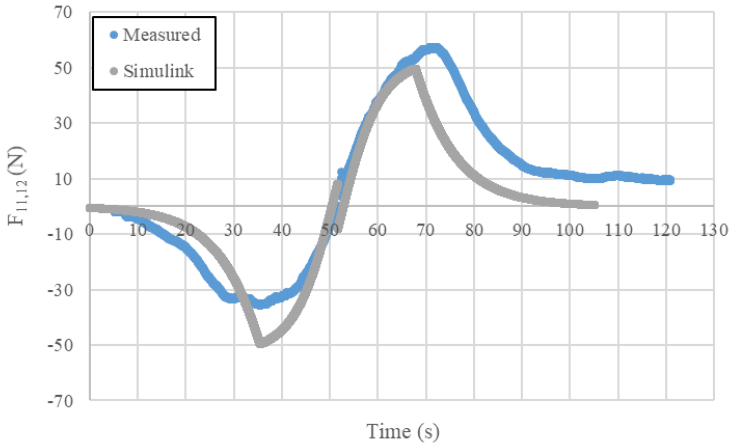

Figure 4.12: *Lateral reaction force vs time @ 278.5 N of normal load with adjusted function (example of better fit).*

4.1.2.4 Final Longitudinal Reaction Force

Longitudinal forces at a caster load of 278.5 N were also plotted again with the new function (Figures 4.13 and 4.14). Adding the extra function is not detrimental to the accuracy of the longitudinal force model but it does not fit as well during the transitions to pure rolling resistance.

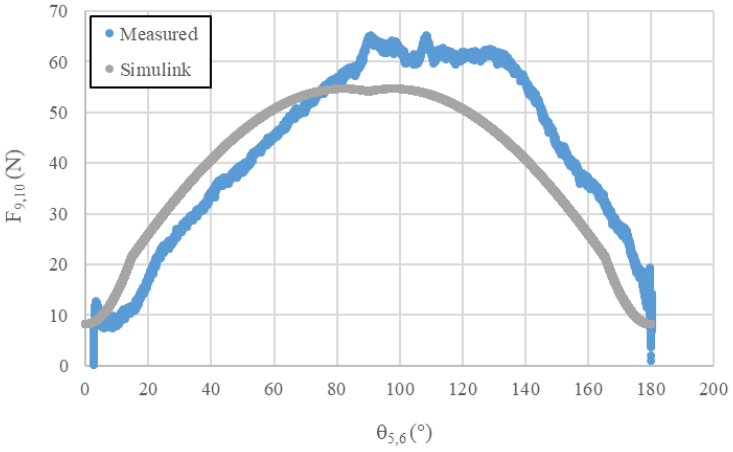

Figure 4.13: *Longitudinal reaction force vs caster angle @ 278.5 N of normal load with adjusted function.*

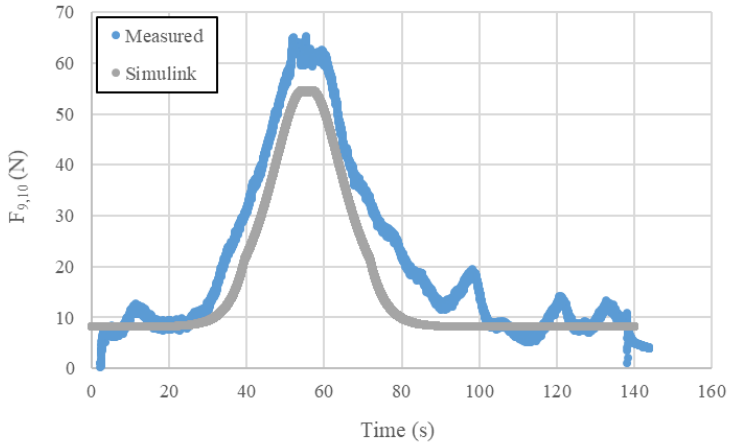

Figure 4.14: *Longitudinal reaction force vs time @ 278.5 N of normal load with adjusted function.*

4.1.2.5 Peak Reaction Forces

For the results discussed thus far, a clear discrepancy is seen in the peak lateral and longitudinal forces. The discrepancies could be due to static forces as well as flex in the experimental rig's frame. There was also issue with the encoder. In some cases the encoder made contact with the main carriage, creating a greater static force between the two carriages (see Figure 4.4c). To mitigate these issues, the encoder was removed and the frame was stiffened. A minimum of 7 new samples were taken at each caster load to gain a better approximation of peak forces. Peak longitudinal and lateral forces were plotted alongside the Simulink model (Figures 4.15 and 4.16). Error bars show ± 1 STDEV. The Simulink trend lines match a power function of $x^{1.5}$, which is no surprise (see equations 3.44 and 3.48). The measured lateral reaction forces also show a similar trend but are closer to a power function of x^2. Measured longitudinal forces are a good approximation except for the last two caster loads and have a high R^2 value. Lateral reaction forces also have a high R^2 value, but are consistently lower than the model. This could be caused by the rolling speed of the caster tire during peak lateral force, because based on all tests at all loads, peak lateral force on average occurs when the caster is 14.5° from finishing its rotation. At this point the caster wheel has some angular/rolling velocity. Coefficient of friction decreases as rolling speed increases as shown by Cao et al

[85]. However, the function (see equation (3.50)) describing the change in friction may not be as close an approximation as assumed. Rolling speed for this particular tire may have a much greater affect on the COF than anticipated, thus decreasing peak lateral forces. Another potential cause for the discrepancy is the experimental frame, which is not completely rigid (even when stiffened). Because the load cell functions via strain gauges, displacement in the frame could cause readings to be lower than expected. Static forces in the linear rails and bearings could also contribute to lower values, particularly because the sub rails on which the sub carriage runs are loaded to a greater extent laterally at peak lateral force for the lateral rig configuration. Due to loose tolerances in the caster mounting plate, caster trail (d_4) may vary by 2-3mm, which would have a small effect. This was investigated by adjusting d_4 in the Simulink model, and indeed, it only shifted the peak force by $\pm$ 0.5 N. Caster king pin wear may also play a part. Grooves were created in the caster king pin during the experiments (see Figure 4.17). This might affect the frictional moment acting on the system from the king pin and bearing interaction. Finally, accurate measurements for the lateral reaction forces rely upon the short rails on the small carriage being perpendicular to the main rails holding the larger carriage. It is probable they are in fact not perpendicular to a small degree.

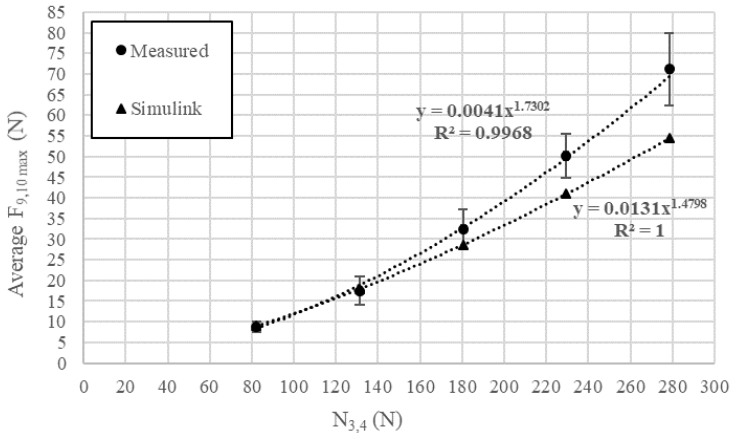

Figure 4.15: *Average peak longitudinal reaction force vs caster load.*

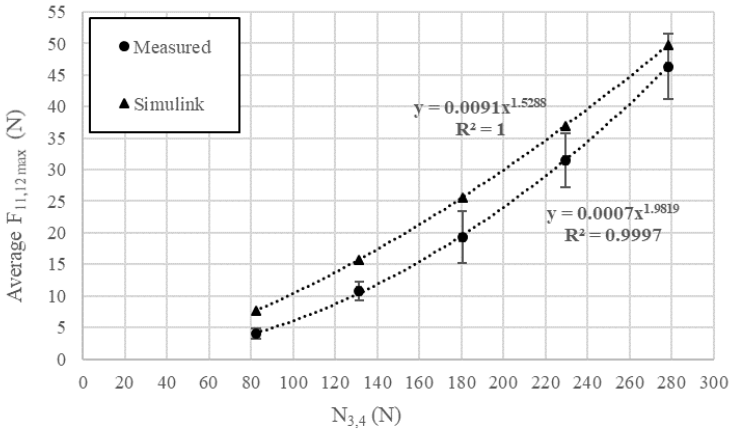

Figure 4.16: *Average peak lateral reaction force vs caster load.*

Figure 4.17: *Damaged caster king pin.*

4.1.2.6 Contact Patch Radius

A comparison of measured and expected contact patch radius (R) can be see in Figure 4.18. A comparison of torque calculated from caster load and tire pressure, and torque calculated using measured R values can be seen in Figure 4.19. Measured tire contact patches are significantly lower than expected values based on caster load and tire pressure. This provides a good explanation of why measured lateral reaction forces are on average lower than expected. The trend line for torques calculated using the measured contact patch radius has a significantly larger exponent than torques calculated from caster load and tire pressure (Figure 4.19). This would explain the larger exponents for the trend lines of the average measured peak caster reaction forces (especially longitudinal forces,

Figure 4.15). The generally lower reaction torque values calculated from measured R values could also explain the lower measured lateral reaction forces.

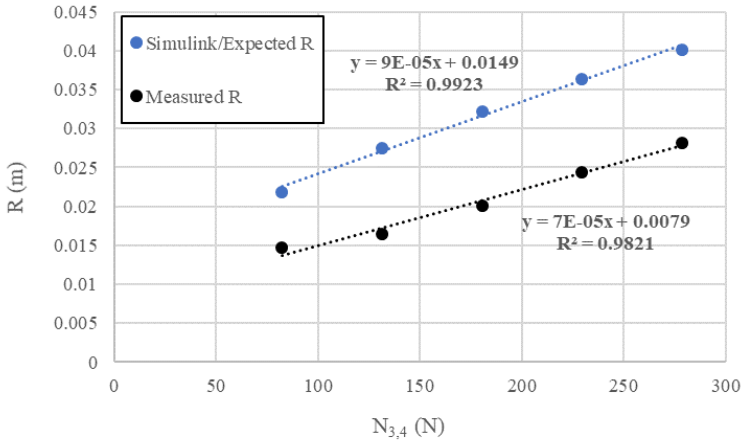

Figure 4.18: *Caster tire contact patch radius vs caster load.*

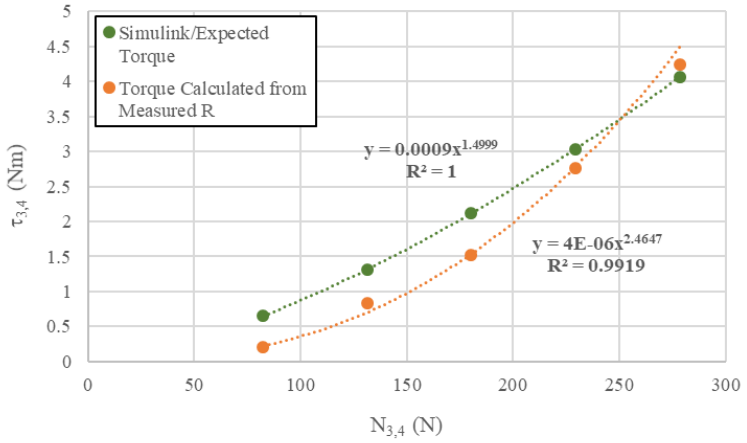

Figure 4.19: *Caster tire reaction torques vs caster load.*

4.1.2.7 Influence of Caster Trail

Peak lateral and longitudinal drive force vs caster trail can be seen in Figures 4.20 and 4.21 respectively. A clear trend can be seen. Peak forces reduce in a non linear fashion as caster trail is increased, with exponents close to -1. This is expected due to the factor of $\frac{1}{d_4}$ in equation (3.46).

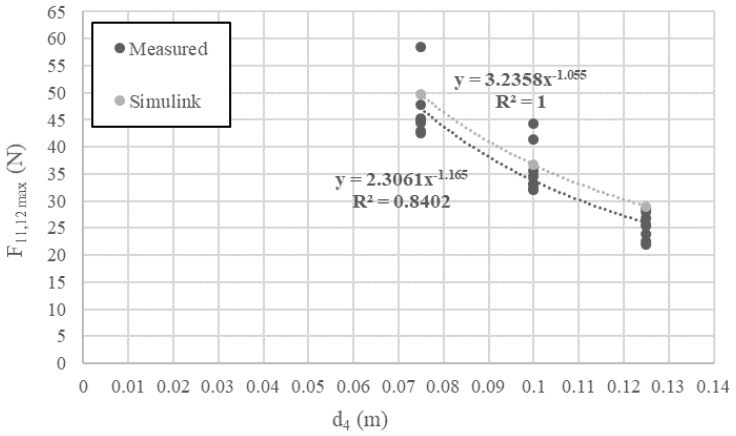

Figure 4.20: *Peak lateral reaction force vs caster trail.*

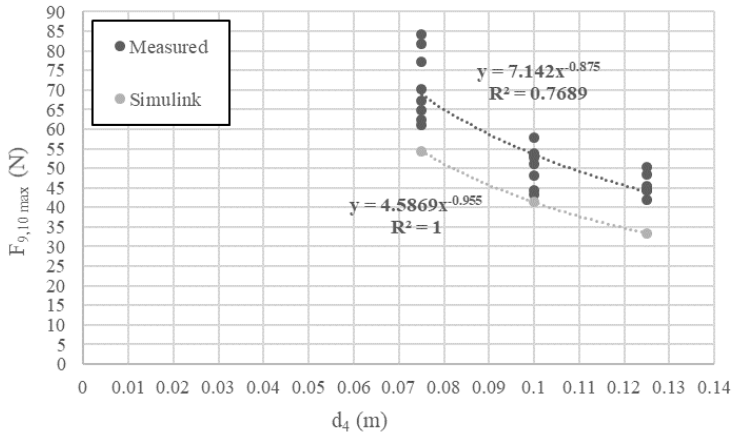

Figure 4.21: *Peak longitudinal reaction force vs caster trail.*

4.1.2.8 Instantaneous Caster Position

Caster angle ($\theta_{5,6}$) vs time for three different king pin speeds ($v_{7,8}$) can be seen in Figures 4.22-4.24). Upon inspection it is clear that the model outlined by Chenier et al (equations (3.16) and (3.17)) is an excellent method to approximate instantaneous caster position [47]. Note, any offsets in the data have been removed because the model does not predict when the caster will start rotating.

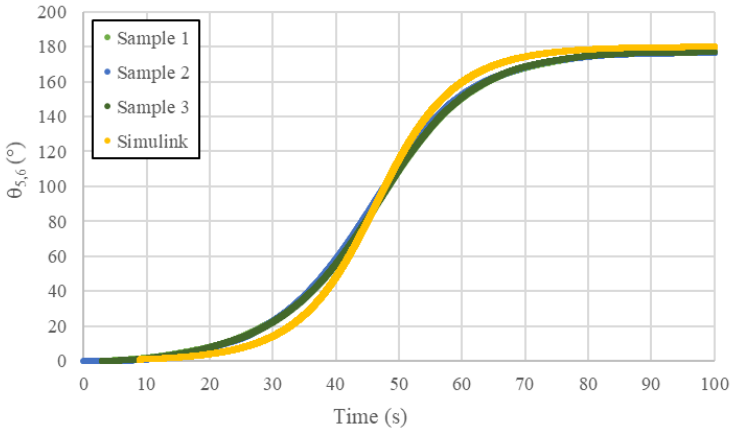

Figure 4.22: *Caster angle vs time @ $v_{7,8}$ = 0.0095 m/s.*

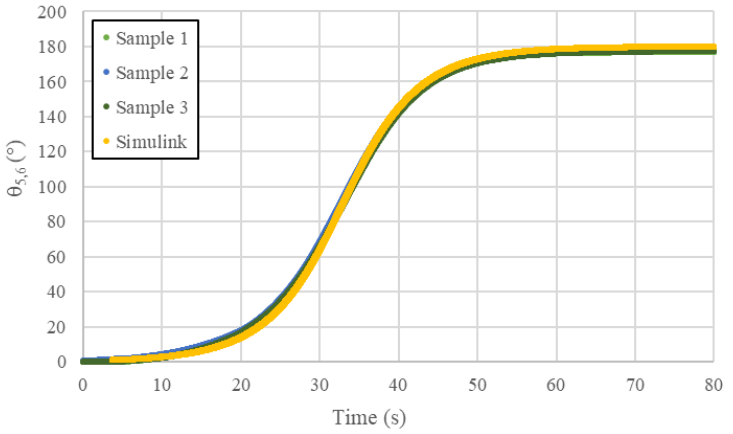

Figure 4.23: *Caster angle vs time @ $v_{7,8}$ = 0.0122 m/s.*

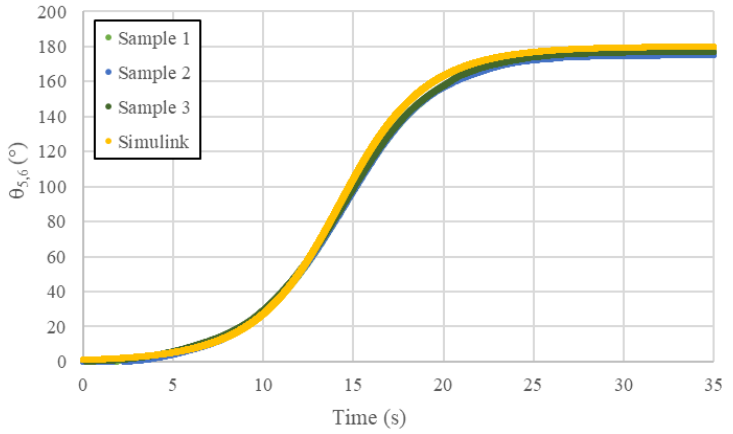

Figure 4.24: *Caster angle vs time @ $v_{7,8}$ = 0.025 m/s.*

4.1.3 Caster Experiment Summary

Despite some discrepancies, the caster model outline in this study is a useful approximation of reaction forces exerted by the casters to the vehicle body. Also, the largest lateral peak force was over predicted making it worse case scenario, which suggests it can be safely used in the optimisation of chassis stiffness in the lateral (x_2) direction. Longitudinal force was under predicted at higher caster loads, but as these forces are in the longitudinal direction (y_2), they will have negligible effects on chassis deflection in the lateral direction. Due to the accuracy of the function describing instantaneous caster position (equations (3.16) and (3.17)), the final reaction force vs time plots are an excellent prediction.

4.2 Solidworks Motion

4.2.1 Comparison of a Simplified Dynamic Model

A simple model of a DDMR was constructed in Solidworks (Figure 4.25). To simplify the Solidworks Motion simulation the vehicle only included the drives wheels (casters ignored), because it would be quite difficult to set up the parameters of the caster model to match casters in Solidworks motion. The rolling resistances were also ignored due to negligible rolling resistance from the solid body contacts used in the Solidworks Motion simulation. The dimensions, mass, and inertia's of the Solidworks vehicle can be seen in table 4.3. An important dimension to notice is the lateral position of the COM (L_1). With a value of 0.395 m it should cause a large degree of eccentricity. It was given a reasonably large value so that it's effect in both software simulations could easily be compared (L_1 would normally be close to 0 for most vehicles). Simulation test parameters can be seen in table 4.4. The Solidworks Motion solver settings can be found in table 4.5. The wheel ground interaction was set as a solid body contact, with the friction and restitution coefficients set at 1 and 0.1 respectively. Models were compared in a level and sloped environment (figure 4.26). The simplified Simulink model assumes the contact patches of the drive

wheels are infinitely small and do not change (i.e. tire compression is not taken into account), meaning normal loads on the wheels cause no frictional forces during vehicle motion. So, effecively, the Simulink model is fixed to be parallel to the slope, because changes in normal forces produce no change in it's motion. To match this, the bottom of the Solidworks Motion vehicle chassis was set to be parallel to the surface of the slope.

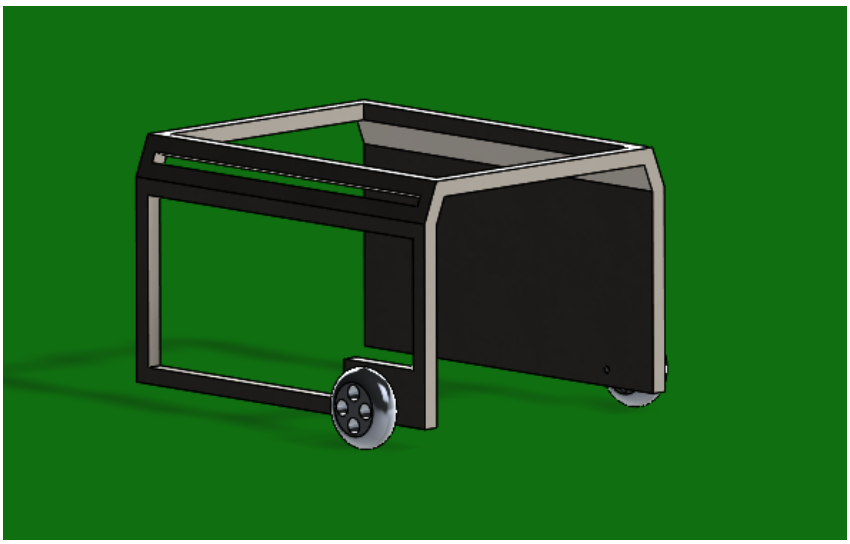

Figure 4.25: *Solidworks test vehicle.*

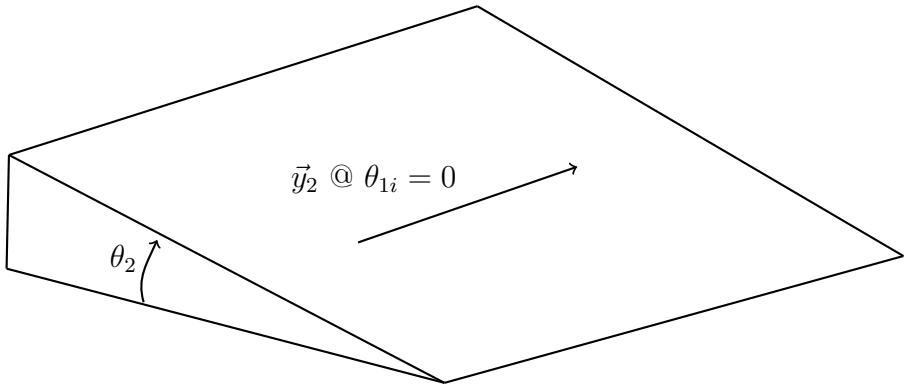

Figure 4.26: *Slope with initial heading equal to zero.*

Table 4.3: Solidworks test vehicle dimensions, mass, and inertia.

r_1 (m)	$2L_2$ (m)	d_1 (m)	L_1 (m)	M_G (kg)	I_G (kgm^2)	I_w (kgm^2)
0.25	2.25	0.793	0.395	1570.31	2075.15	0.9

Table 4.4: Solidworks test values for drive torques (τ_1 and τ_2), initial vehicle heading (θ_{1i}) and slope angle (θ_2). τ_1 = left wheel drive torque and τ_2 = right wheel drive torque.

Test	τ_1 (Nm)	τ_2 (Nm)	θ_{1i} (rad)	θ_2 (°)
1	100	100	0	0
2	-100	-100	0	0
3	25	250	0	0
4	-100	100	0	0
5	100	100	0	2
6	-100	-100	0	2
7	25	250	0	2
8	-100	100	0	2

Table 4.5: Solidworks Motion solver settings.

Parameter	Type/Value
Accuracy	0.001
Initial Integration Step	0.0000001
Max Integration Step	0.001
Min Integration step	0.001
Frame Rate	1000
Jacobian Matrix Evaluation	Every iteration
Max Iterations	25
Solver	GSTIFF

Upon initial inspection, the general motion of the vehicles are a good match, even when the trajectory is more complex (Figures 4.28, 4.30, 4.32, and 4.34). Any discrepancies could be due to how Soliworks Motion models the wheel-ground contacts. They are modelled as solid body contacts where as the Simulink model assumes a non-slip condition.

Initial trajectories did not match as well as the final ones shown. The dynamic and static coefficiant of fricion (COF) in the Solidworks model was initially set at 1 (with a restitution coefficient of 0.00001 to reduce vibration) to provide maximum traction,

and because it was assumed the contact patch of wheel-ground contacts was negligible. However, reducing the static and dynamic COF to 0.25 gave a much better match with the Simulink model. Therefore, it was concluded the contact patch in the Solidworks model was not in fact negligible. Contact patch radius is normally accounted for in the Simulink model, but it is based off tire pressure and a normal load. This does not match how contacts are modelled in Solidworks and thus it was ignored in the Simulink model. This caused the discrepancy between the frictional tire forces of the two models. The COF was not dropped below 0.25 in the Solidworks model, because traction needed to be maintained at all times to match the non-silp condition assumed by the Simulink model.

Differences in the solvers could also be a source of discrepancy. The Simulink study used the Runge Kutta 4th order solver (with a fixed time step of 0.001 s), whereas the GSTIFF integration method was used in Solidworks. GSTIFF was developed by C.W.Gear and is a variable order, variable step size integration method.

Though not an exact match, no major discrepancies between the two models are observed, meaning good agreement exists between the Simulink model and Solidworks Motion.

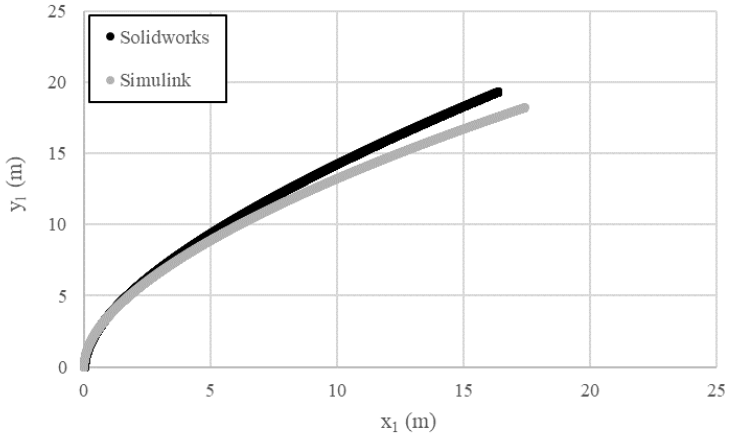

Figure 4.27: *Test 1, equal positive drive torques on level ground.*

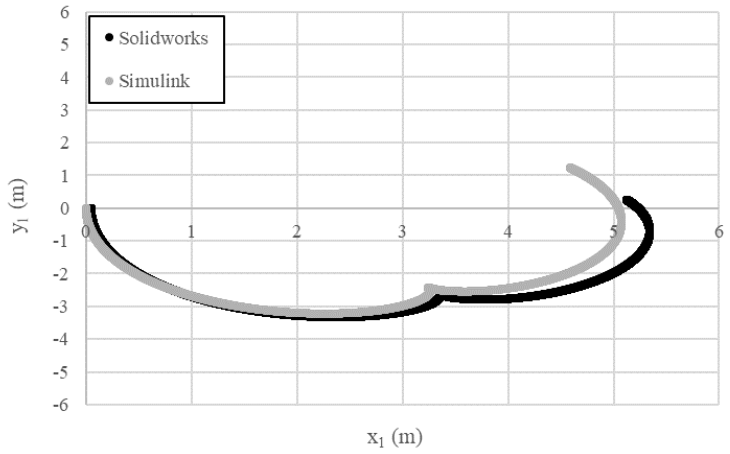

Figure 4.28: *Test 2, equal negative drive torques on level ground.*

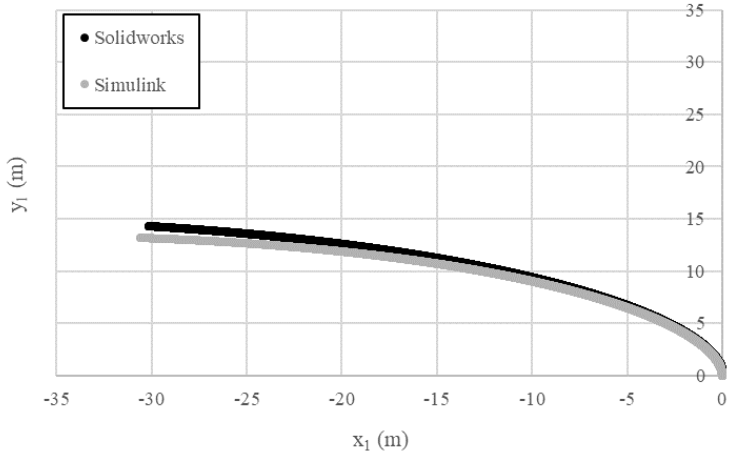

Figure 4.29: *Test 3, unequal positive drive torques ($\tau_1 < \tau_2$) on level ground.*

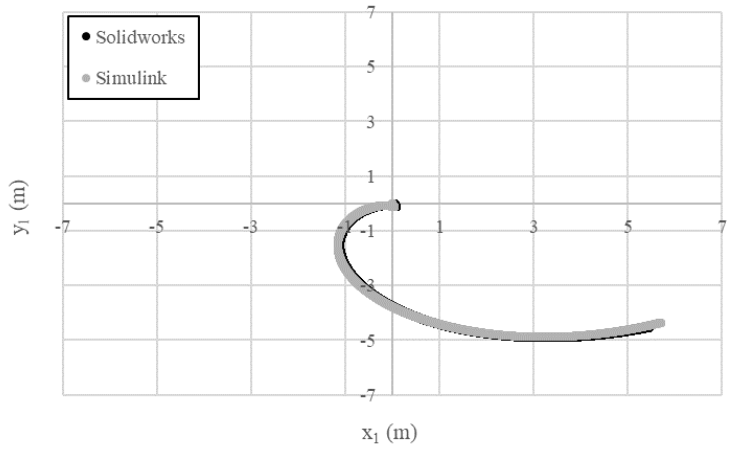

Figure 4.30: *Test 4, equal and opposite drive torques on level ground.*

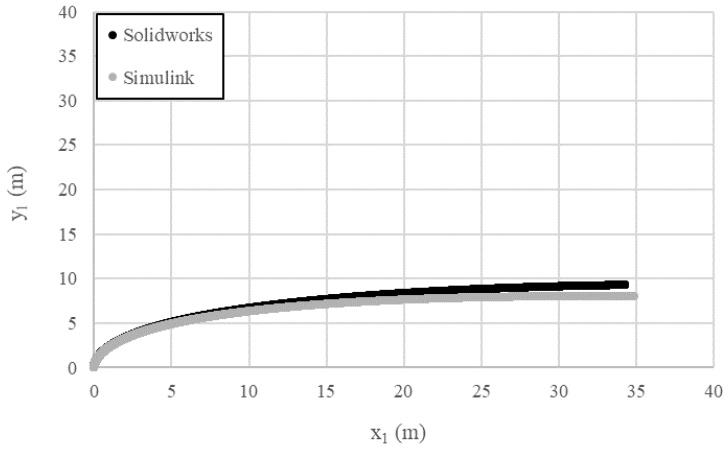

Figure 4.31: *Test 5, equal positive drive torques on slope.*

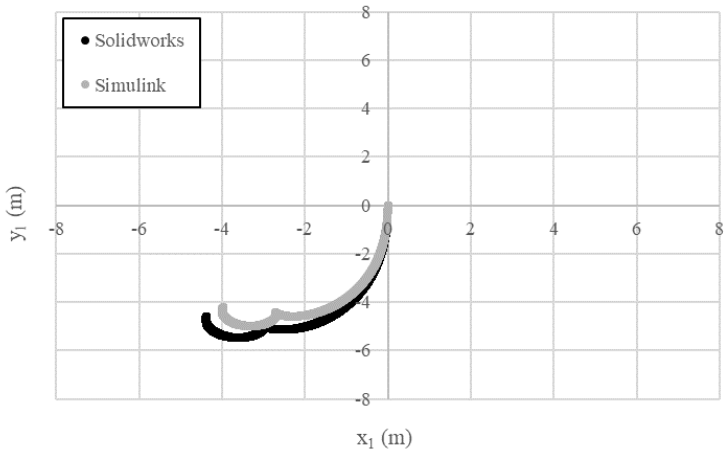

Figure 4.32: *Test 6, equal negative drive torques on slope.*

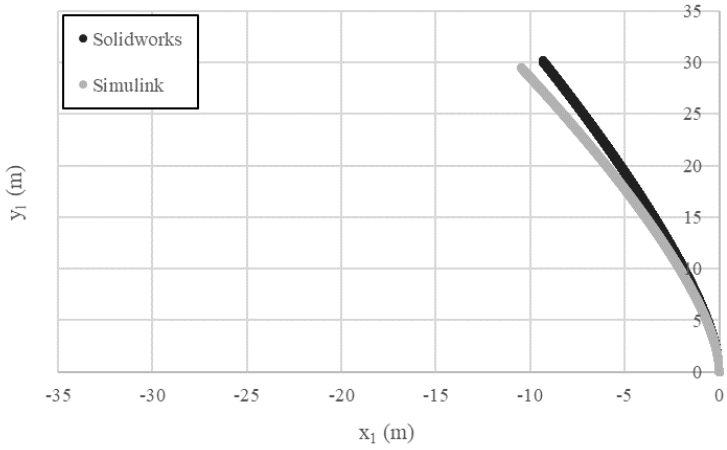

Figure 4.33: *Test 7, unequal positive drive torques ($\tau_1 < \tau_2$) on slope.*

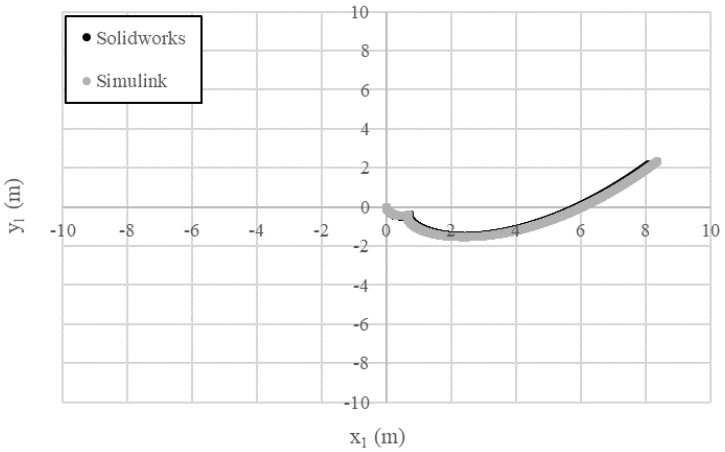

Figure 4.34: *Test 8, equal and opposite drive torques on slope*

4.2.2 Comparison of Solidworks Motion and Simulink for Caster Reaction Forces

The Simulink caster model was compared against a Solidworks simulation of the caster experiment (Figure 4.35). The Solidworks Motion experiment was modelled as a steel wheel on a steel floor to minimise "tire" deflection. Results were first compared to the Simulink model with $\theta_{F_{11,12max}} = 14.5°$. Note, the peak longitudinal reaction force of the Simulink model was adjusted (by changing caster load) to match Solidworks to allow an easier comparison. Rolling resistance was removed from caster model due to difficulties in modelling rolling resistance in the Solidworks model. It is clear that $\theta_{F_{11,12max}}$ is much smaller (3°) in the Solidworks simulation (Figures 4.36 and 4.37). This not surprising considering the material used for the wheel and floor (steel), highlighting the effect of the material properties of a tire.

With $\theta_{F_{11,12max}}$ adjusted to 3° in the Simulink model, results match much better (Figure 4.36 - 4.39). If observed closely, there is small change in the Solidworks longitudinal force vs time curve similar to the one caused by $\theta_{F_{11,12max}}$ in the Simulink model in the regions where the curve flattens out to zero (Figure 4.39). This suggests the Solidworks model uses material properties (or experimental factors) to define a $\theta_{F_{11,12max}}$ like point at which the force definition for $F_{14,16}$ changes. All forces match match well with $\theta_{F_{11,12max}} = 3°$. Showing that Simulink caster model can be used in place of Solidworks provided $\theta_{F_{11,12max}}$ is selected correctly.

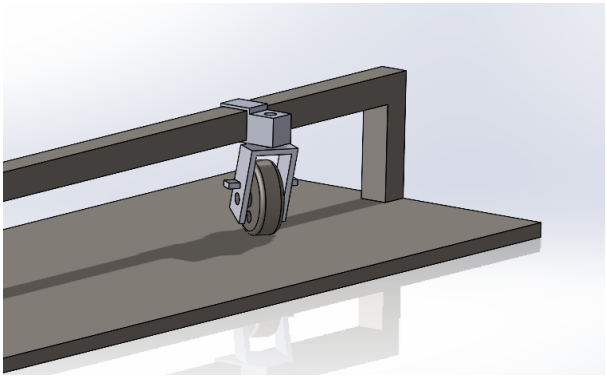

Figure 4.35: *Solidworks simulation model.*

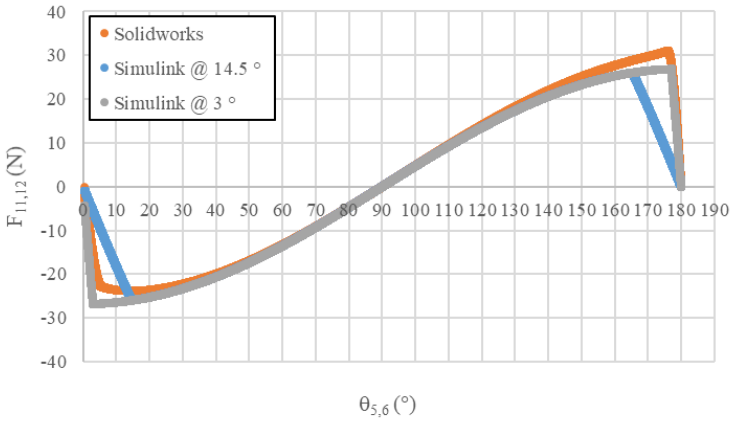

Figure 4.36: *Lateral reaction force vs caster angle with $\theta_{F_{11,12max}} = 14.5°$ and $\theta_{F_{11,12max}} = 3$ °.*

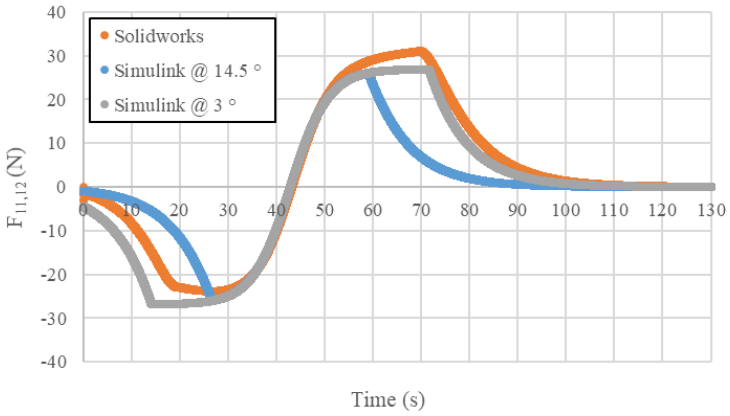

Figure 4.37: *Lateral reaction force vs time with* $\theta_{F_{11,12max}} = 14.5°$ *and* $\theta_{F_{11,12max}} = 3$ *°.*

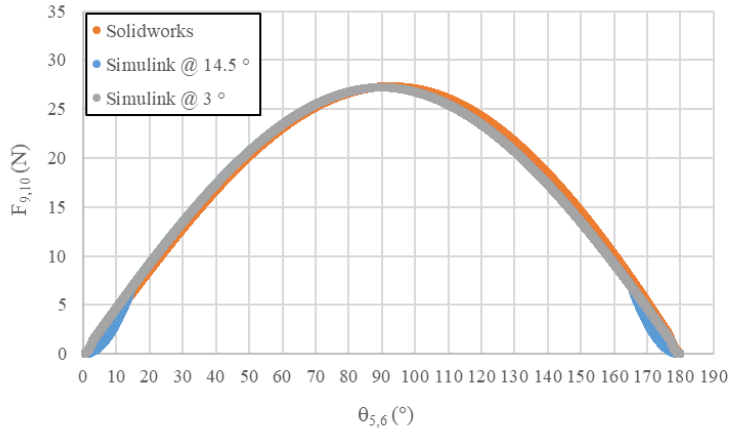

Figure 4.38: *Longitudinal reaction force vs caster angle with* $\theta_{F_{11,12max}} = 14.5°$ *and* $\theta_{F_{11,12max}} = 3$ *°.*

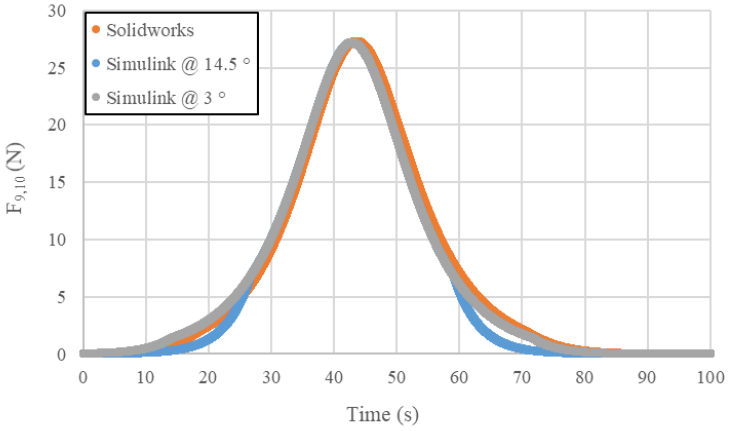

Figure 4.39: *Longitudinal reaction force vs time with* $\theta_{F_{11,12max}} = 14.5°$ *and* $\theta_{F_{11,12max}} = 3$ *°.*

The Simulink model is a very useful because computation times are low. This is a

key benefit of simplified mathematical models over motion software packages such as Solidworks Motion. The accuracy of the caster model is key to understanding how caster design (namely caster dimensions) affects the performance of DDMRs and the loads applied to the chassis, which in turn is important because DDMRs almost exclusively use casters. Both this Solidworks comparison and the caster experiment have shown the caster model is a good approximation of instantaneous caster reaction forces.

4.3 Field Testing

Field testing was conducted to assess the ability of the vehicle model to predict the motion of an existing DDMR in a real world environment.

4.3.1 Nico Bot

The "Nico Bot" is a mid size research DDMR designed to conduct surveying on farmland (Figure 4.40). This vehicle was used to conduct initial testing, and was chosen for validation because it is small and easy to use. The vehicle was driven on different trajectories, and motor current and wheel speeds were measured. Torque output from the motors was then determined from the measured current, and wheel velocities were converted into linear and angular velocities of the vehicle. Mass, inertia, and key dimensions of the Nico Bot can be seen in tables 4.6 and 4.7. See Figure 3.4 for reference.

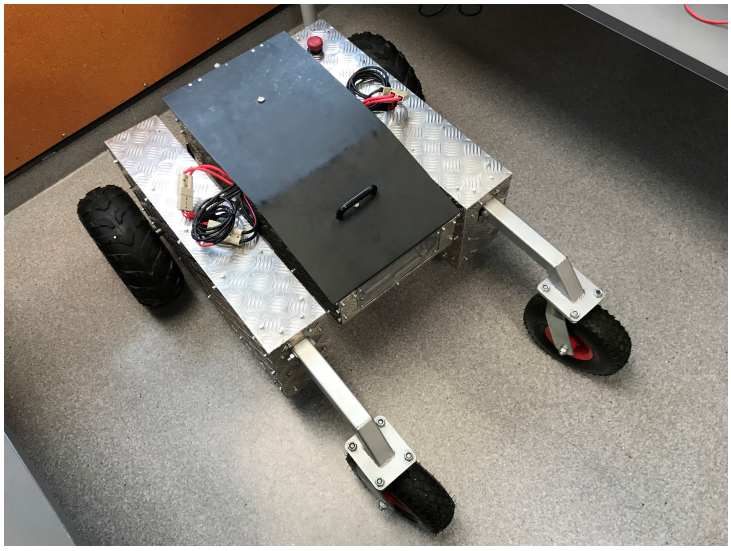

Figure 4.40: *The "Nico Bot".*

Table 4.6: Nico Bot dimensions.

d_1 (m)	d_3 (m)	d_4 (m)	L_1 (m)	$2L_2$ (m)	$2L_3$ (m)	r_1 (m)
0.257	0.86	0.0525	0	0.836	0.552	0.167

Table 4.7: Mass, inertia and other properties of the Nico Bot

M_G (kg)	I_G (kgm^2)	Caster Tire (kpa)	Drive Tire Pressure (kpa)
86.1	13.1	90	29

4.3.1.1 Setup and Calibration

A dynamic COF of 0.81 was used for an asphalt surface, and a COF for concrete of 0.77 [88][89][90][91][92][93][88]. To allow estimation of rolling resistance the drive wheels were decoupled from the drive shafts and allowed to roll freely on their bearings. The vehicle was then pulled along a flat concrete surface with a digital load cell. The total coefficient of rolling resistance of the bot was found to be approximately 0.0314. It was assumed that the caster and drive wheels both have the same coefficient. The torque vs current relationships (Figure 4.41) were determined by operating the motors while applying a

torque to the drive shafts and measuring the current drawn (unfortunately minimal data existed for the motors, making the experiment necessary). Note, no load current was 2.75 and 2.55 A for the right and left motor respectively, and these values were subtracted from the results to give a no-load current of 0 A.

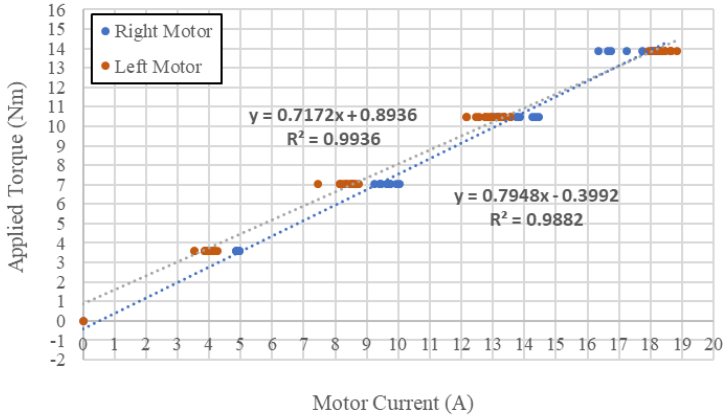

Figure 4.41: *Drive shaft torque vs motor current.*

To calibrate the vehicle, it was driven forward on flat smooth concrete. The initial trajectory, wheel velocities, and drive forces can be seen in Figures 4.42-4.44. The Simulink trajectories were found by plugging the measured drive torques in the forward dynamic model. Drive forces were obtained by plugging in the wheel velocities into the inverse model. The model predicts a distance traveled of approximately 5.7 m. The actual vehicle traveled approximately half the distance at 2.7 m (4.42). Predicted drive forces (Figure 4.44) are lower and drive wheel velocities (Figure 4.43) are higher than expected, meaning the model predicts less resistance to acceleration. This suggests there are extra forces in the vehicle that the Simulink model does not account for. The design of the vehicles power train was not ideal. Drive shafts and bearings did not line up properly with the gearbox. Even though the current-torque relationship was calculated by applying torques to the ends of the drive shafts (which should mean resistances in the power train are taken into account), it may be the resistances in the power train are different when the vehicle is fully assembled and in operating condition. The mass of the vehicle could be a poor estimation, but this is unlikely as the vehicle was weighed twice. It is also unlikely that rolling resistances of the tires were measured inaccurately, as these were also measured twice, with two different digital load cells.

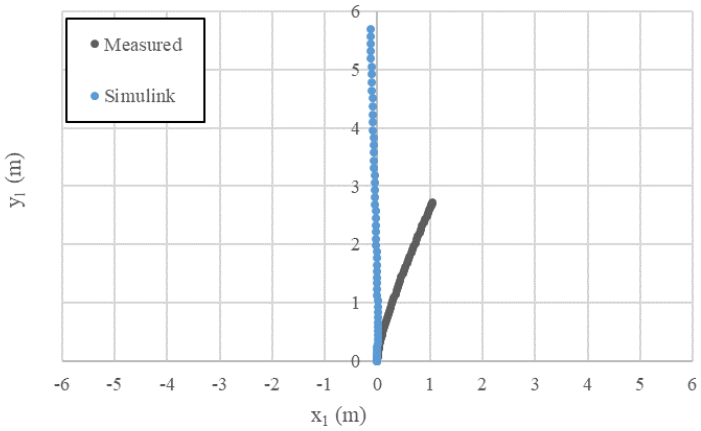

Figure 4.42: *Initial calibration run trajectories.*

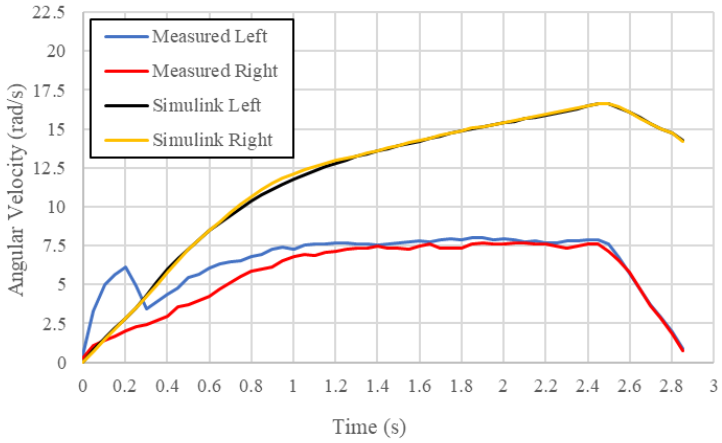

Figure 4.43: *Angular velocities of left and right drive wheels ($\dot{\theta}_3$ and $\dot{\theta}_4$).*

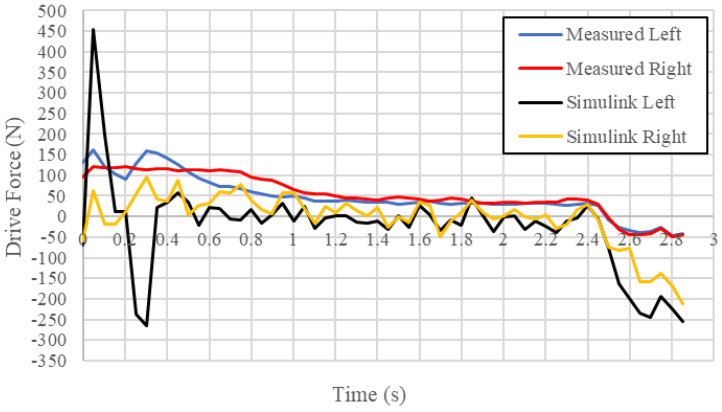

Figure 4.44: *Drive forces of left and right drive wheels (F_1 and F_2).*

To simulate the extra resistance in the drive train, the rolling resistances of the drive wheels were increased to 0.1338 and the resulting trajectory can be seen in Figure 4.45. The linear distance traveled (y_2) for both the model and vehicle are now equivalent, but the angular displacements (θ_1) show a large discrepancy (a consistent discrepancy across multiple tests). Figure 4.47 shows a large spike in the measured angular velocity of the left drive wheel. This affects the angular velocity of the vehicle (Figure 4.46). This discrepancy is most prominent at the start of the vehicles motion. A greater drive force was measured for the left drive wheel of the vehicle during the initial period of the vehicles motion (Figure 4.48). This must be the cause of velocity spike for the left wheel. It is unclear why this has occurred. It may be a higher PWM signal is momentarily given to the left motor, but this unlikely as no discrepancies were found in the Arduino script. Components of the right hand drive train (particularly the drive shaft) may have slipped (due to the poor design), causing the current to be lower, but a sudden drop in drive wheel force and a sudden increase in wheel velocity should be seen, but this not observed. Note, slippage of the drive shaft would cause a perceived increase in wheel velocity because the encoder is connected to the gear box, not the wheel.

When the vehicle reaches a steady velocity it continues to veer off to the right (but at a lower rate than at the start) (Figures 4.45 and 4.46). This suggests an imbalance exists in rolling resistance or the resistance between the left and right drive trains. Caster imbalances could be a contributor, but this is less likely because the mechanical construction of the casters will be more consistent than the drive trains. The pressure in the right hand caster was 2 psi (14000 Pa) higher than the left, but it is unlikely this would be enough to cause the vehicle to veer to the right, and is likely to be counteracted by the pressure imbalance in the drive wheels (Right being 0.5 psi (3400 Pa) lower than the left). Note, casters were set at an initial angle of approximately 0 ° before each test to remove the fishtail effect, so this rules out instability due to casters.

The modelled and measured drive forces are a better match with the increased rolling resistance of 0.1338 (Figure 4.48). Note, when comparing the drive forces, only the rough average of the Simulink forces can be evaluated against measured values. Velocities from the experiments were sampled at 50 ms. Because the inverse model is computed from the

measured velocities, large spikes are observed in the computed torques. If the data had been measured at a much faster rate, the computed torques would be smoother allowing for a better comparison. The measured current was also sampled at 50 ms. This course sample rate also affects the velocity outputs from the forward model, though the effect is not detrimental. So, for this study, simulated drive forces are deemed to be a good match if the rough average follows the measured data.

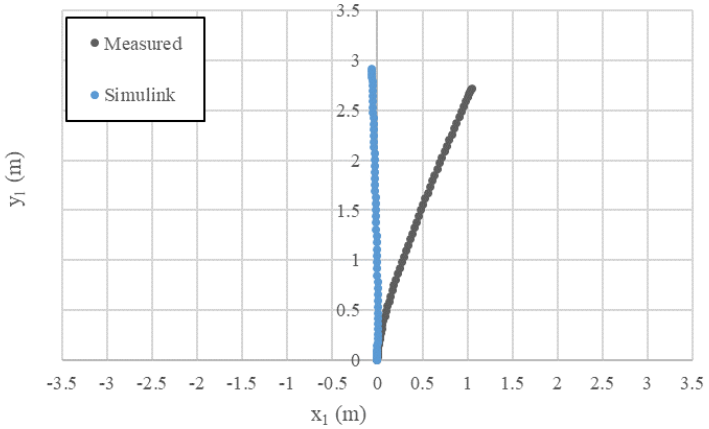

Figure 4.45: *Trajectory with rolling resistance of 0.1338.*

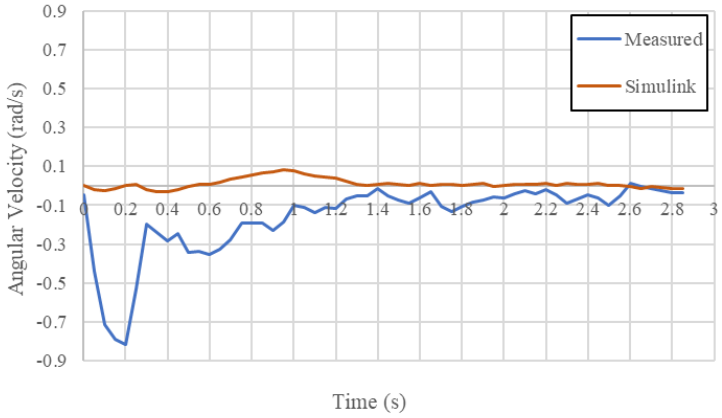

Figure 4.46: *Angular velocity of vehicle ($\dot{\theta}_1$) with rolling resistance of 0.1338.*

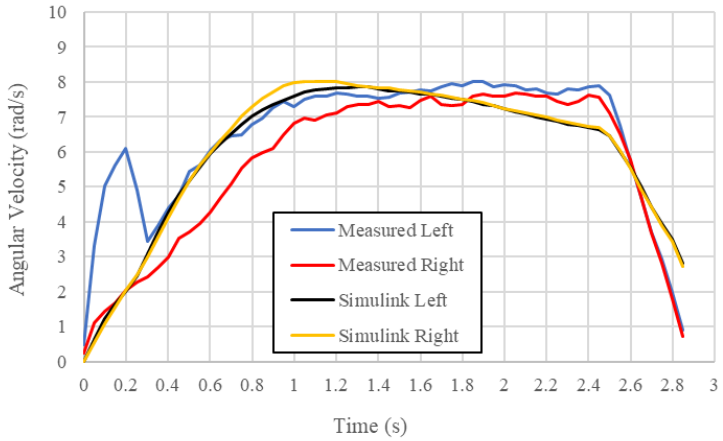

Figure 4.47: *Angular velocities of left and right drive wheels ($\dot{\theta}_3$ and $\dot{\theta}_4$) with rolling resistance of 0.1338.*

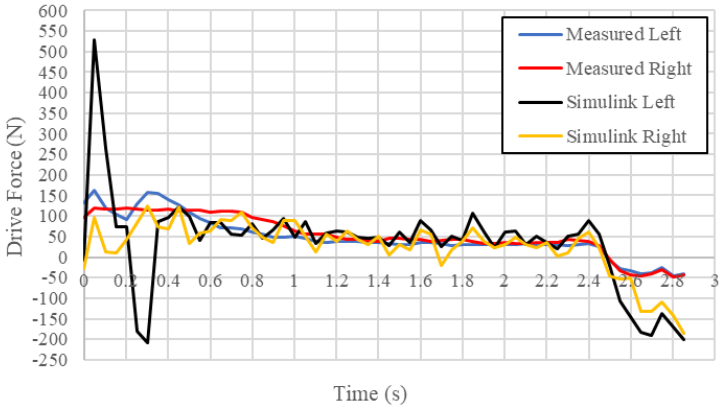

Figure 4.48: *Drive forces of left and right drive wheels (F_1 and F_2) with rolling resistance of 0.1338.*

The reaction torques applied to the drive tires by the ground were investigated to asses their accuracy. If simulated values are too large, they could prevent the vehicle from turning . Equation (4.3) is an alternative form of (3.60) and was used to calculate the expected contact patch radius of the drive wheels.

$$M_{1,2} = \frac{2\pi\mu p R^3}{3} \tag{4.3}$$

The expected drive wheel contact patch radii (based of wheel load and pressure) were found to be 0.0567 m. Actual contact patches of the drive wheels were measured and

were found to be 76.8 % of expected. The measured radius was plugged back into (4.3) and the torque was found to be 45 % of simulated. Therefore, the simulated/expected reaction torques were reduced by 55 %. The casters were also checked, and the actual contact patch (average of 0.0189m) was found to be 98 % of expected. Torque calculated using the actual contact patch is 94 % of simulated, so the simulated/expected values were left unchanged.

To finish calibration, the rolling resistances of each drive wheel were adjusted until the simulated angular velocity matched the angular velocity of the vehicle toward the end of its motion (to be in the steady state region). Results with rolling resistances $k_{1L} = 0.096$ (left wheel) and $k_{1R} = 0.172$ (right wheel) can be seen in Figures 4.49 and 4.51.

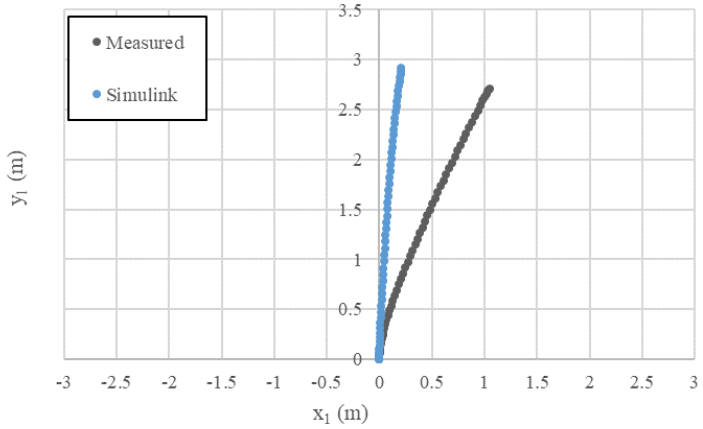

Figure 4.49: *Trajectory with rolling resistance of* $k_{1L} = 0.096$ *and* $k_{1R} = 0.172$.

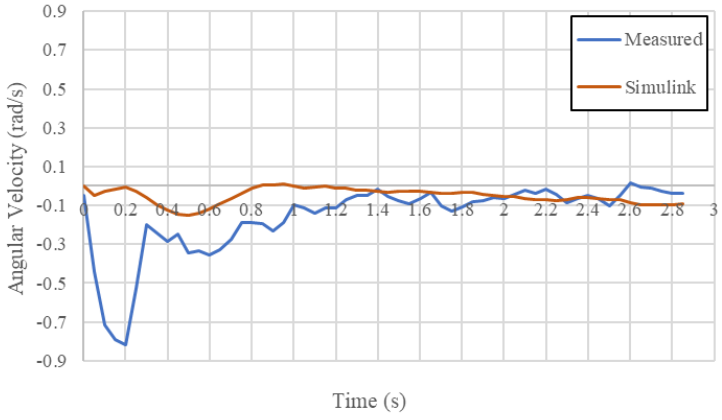

Figure 4.50: *Angular velocity of vehicle with rolling resistance of* $k_{1L} = 0.096$ *and* $k_{1R} = 0.172$.

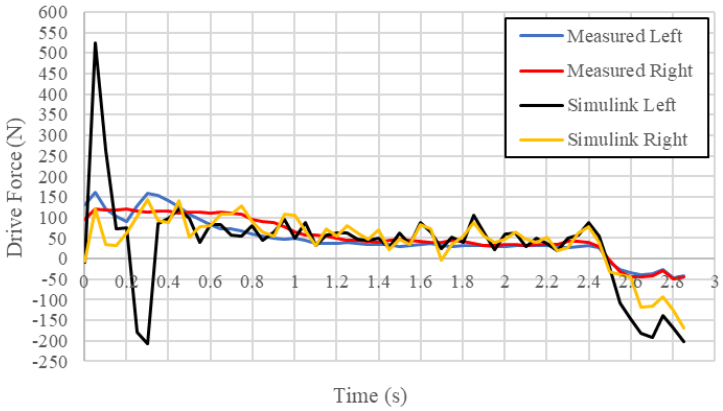

Figure 4.51: *Drive forces of left and right drive wheels with rolling resistance of* $k_{1L} = 0.096$ *and* $k_{1R} = 0.172$.

After calibration, the vehicle was driven on various slopes and trajectories. It was found that the measured slopes driven upon could not be described with only one angle. Therefore, gravitational forces on the vehicle were adjusted to include another angle (see equations (4.4) and (4.5)). θ_2 has now become θ_{2p} (primary slope) and the secondary slope is θ_{2s} (Figure 4.52). Nico Bot tests on slopes can be seen in table 4.8.

$$F_8 = m_G g \sin\theta_{2p} \sin\theta_1 + m_G g \sin\theta_{2s} \cos\theta_1 \tag{4.4}$$

$$F_7 = m_G g \sin\theta_{2p} \cos\theta_1 - m_G g \sin\theta_{2s} \sin\theta_1 \tag{4.5}$$

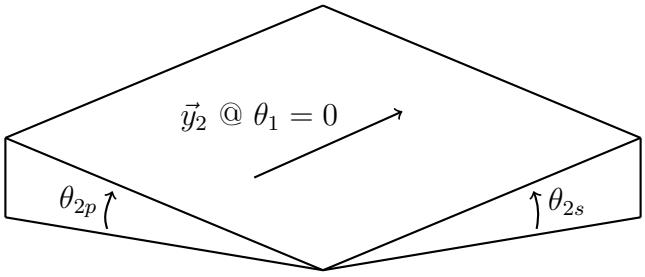

Figure 4.52: *Slope defined by two angles.*

Table 4.8: Nico Bot tests on slopes. θ_{1i} = initial heading of vehicle.

Trajectory	θ_{1i} (°)	θ_{2p} (°)	θ_{2s} (°)
1	0	4.05	0.6
2	π	4.05	0.6
3	$\frac{\pi}{2}$	4.05	0.6
4	$\frac{\pi}{2}$	4.05	0.6
5	$\frac{\pi}{2}$	4.05	0.6
6	$\frac{\pi}{2}$	4.05	0.6
7	$\frac{\pi}{2}$	2.4	-0.4
8	$\frac{\pi}{2}$	6.6	-0.89
9	$\frac{\pi}{2}$	6.6	-0.89
10	π	6.6	-0.89
11	0	6.6	-0.89

4.3.1.2 Analysis of Test Results

The first test shows a significant discrepancy between measured and simulated trajectories (Figure 4.53). Drive forces behave in a similar fashion but diverge toward the end of the test (Figure 4.54). Initial velocities match well to start but quickly diverge (Figure 4.55).

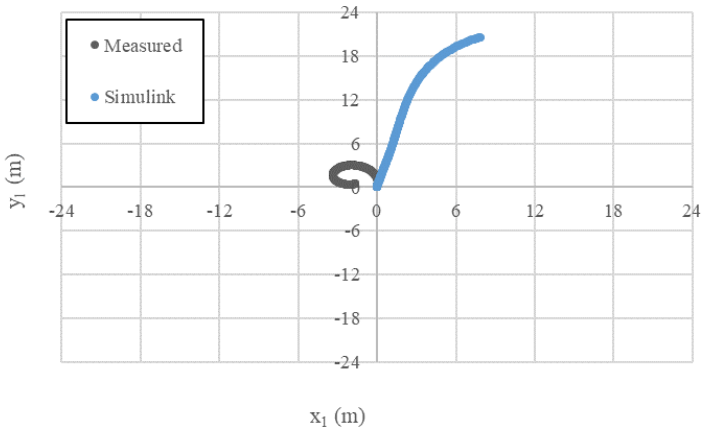

Figure 4.53: *Nico Bot test 1 trajectory.*

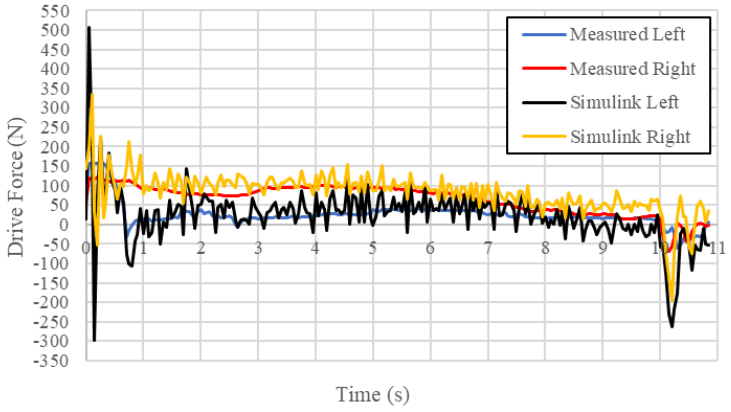

Figure 4.54: *Nico Bot test 1 drive wheel forces.*

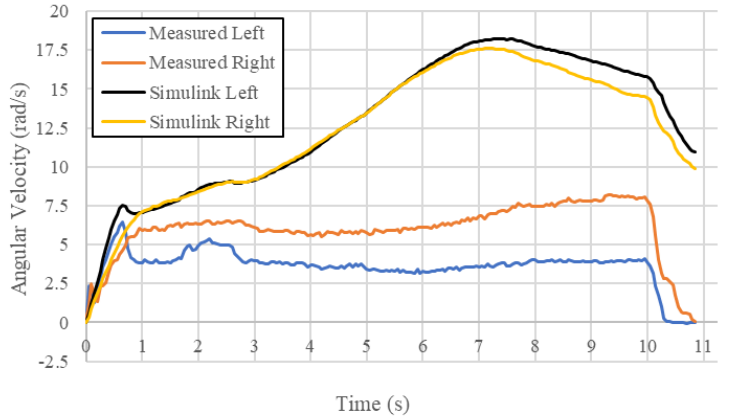

Figure 4.55: *Nico Bot test 1 wheel velocities.*

The trajectory of the second test matches better but still shows a large discrepancy later in the test (see Appendix B for all graphs not shown here). The drive forces again behave similarly but show quite different magnitudes for large portions of the test. Wheel velocities diverge greatly after 3 s. For test 4, the overall motion of vehicle trajectories show the best match of all the tests but the final positions obtained differ greatly (Figure 4.56). Drive forces behave similarly but with quite different magnitudes in middle portion of the test (Figure 4.57). Velocities show better agreement but with large discrepancies in the middle portion of the test (Figure 4.58).

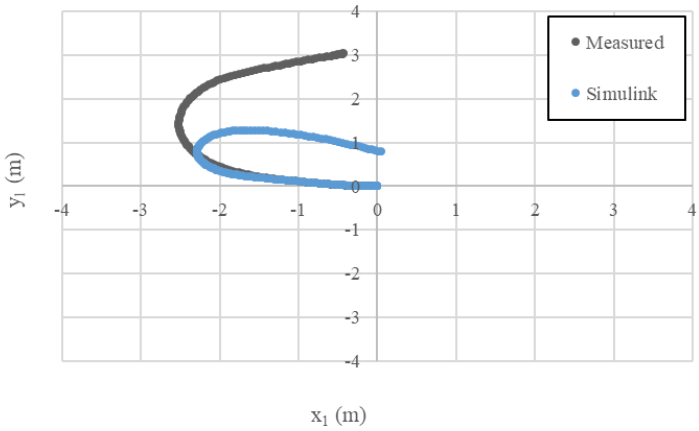

Figure 4.56: *Nico Bot test 4 trajectory.*

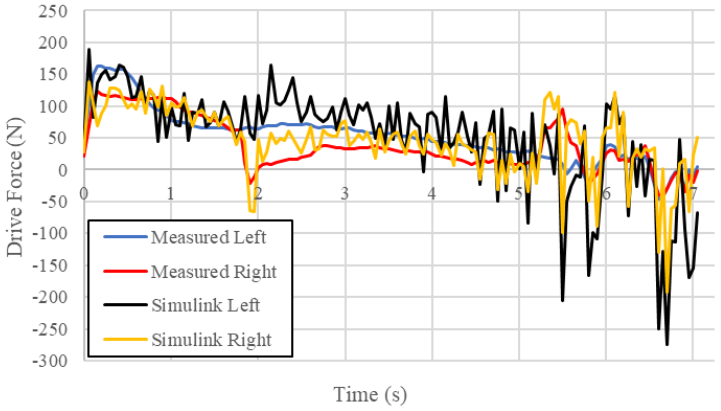

Figure 4.57: *Nico Bot test 4 drive wheel forces.*

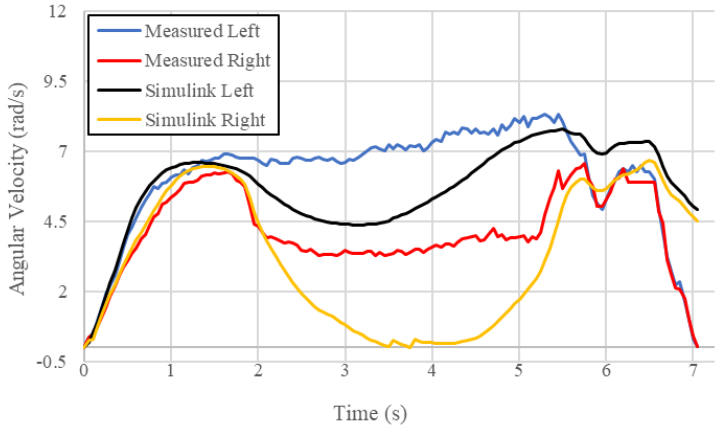

Figure 4.58: *Nico Bot test 4 wheel velocities.*

For test 3, the trajectories match very well for as far the Simulink model travels, but the Simulink model fails to make it up to the top of the slope. The drive forces match quite well for most of the test. Wheel velocities diverge drastically after 1 s.

A strange trajectory for the Simulink model is observed in test 5 (Figure 4.59). The vehicle has reversed with a positive angular velocity upon reaching the top of the slope (Figures 4.62 and 4.63). This is due to the abrupt change in measured drive forces at around 6.5 s (Figure 4.60). Drive forces show excellent agreement except at 6.5 s. Wheels velocities both show a sudden drop at 6.5 s but with Simulink showing a much larger drop for the left drive wheel (Figure 4.61). Both trajectories for test 6 are similar but the Simulink model turns sooner because it takes longer to climb the slope. Drive forces show less agreement. Wheel velocities diverge quickly after approximately 1.8 s.

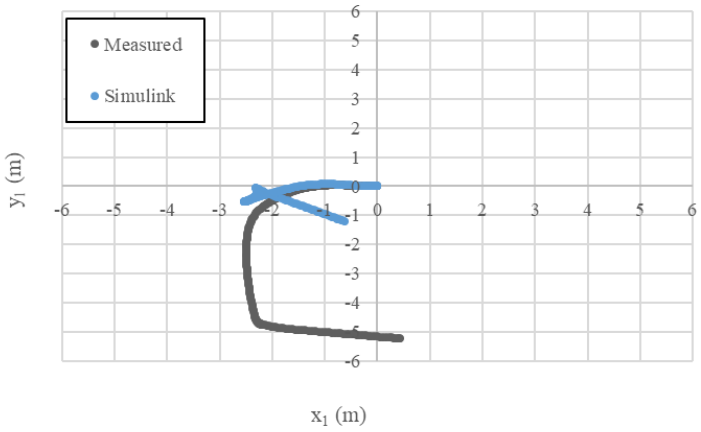

Figure 4.59: *Nico Bot test 5 trajectory.*

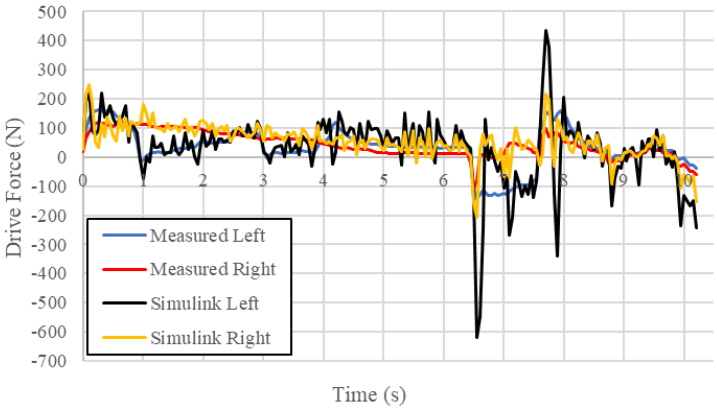

Figure 4.60: *Nico Bot test 5 drive wheel forces.*

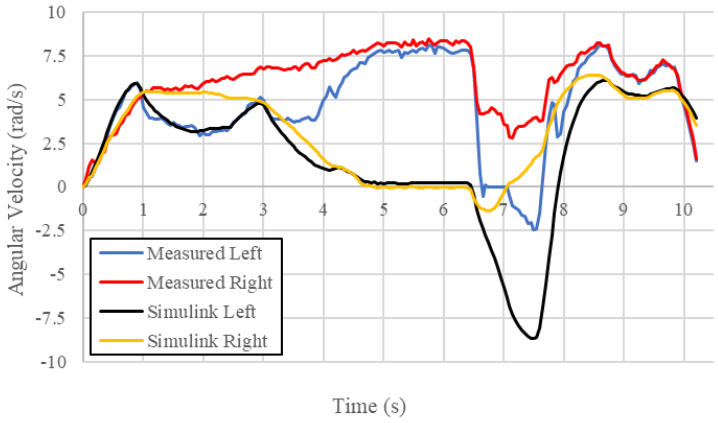

Figure 4.61: *Nico Bot test 5 wheel velocities.*

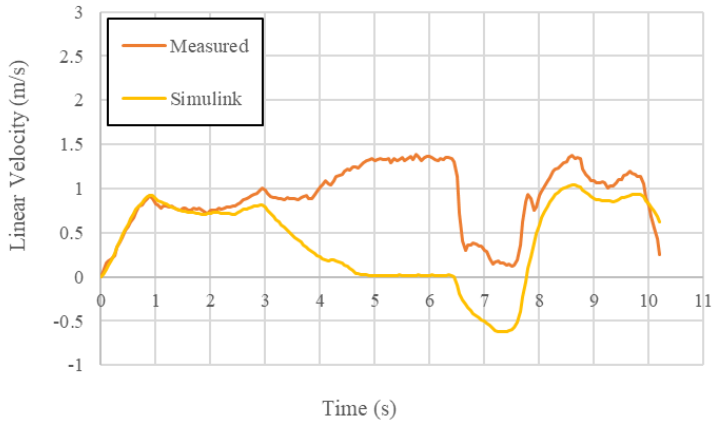

Figure 4.62: *Nico Bot test 5 linear velocities of vehicles.*

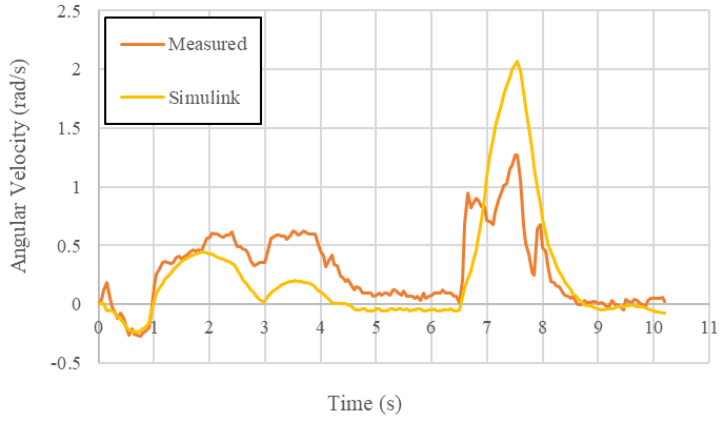

Figure 4.63: *Nico Bot test 5 angular velocities of vehicles.*

During the first six tests, the model does not match well when the vehicles initial heading is adjacent to the slope (Tests 1 and 2). Trajectories are more similar when the vehicle drives straight up the slope and makes a turn (tests 3, 4, 5, and 6). Trajectories 8-11 do not match well at all (see Appendix B). The slope angle is larger on these trajectories and the it may be that the vehicle is operating near maximum capability at a slope angle of 6.6 °. If this is the case, any inaccuracy in the Simulink model could have a large effect on the simulated trajectory. For test 7 (turning on the spot on a slope), the trajectories also do not match well but the drive forces show similar behaviour (Figure 4.64).

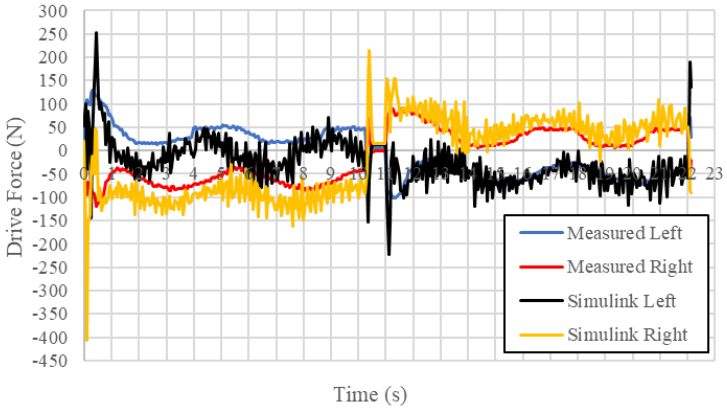

Figure 4.64: *Nico Bot test 7 drive wheel forces.*

The tests in this study do not match well enough to provide a source of validation. However, this does not mean the model is not adequate for design optimisation. Due to mechanical inconsistencies (namely in the drive train), the Nico Bot is not an ideal test vehicle. Also, the vehicle is not a perfect representation of a DDMR with an infinitely stiff chassis (the dynamic model assumes a rigid chassis) because it's chassis is split into 3 parts (see Figure 4.40). The three units are joined together via two shafts. This design allows for each side to pivot and adjust for uneven terrain but is not an ideal match for the Simulink model. Data sampling rate was also an issue. The vehicle was driven and the sensors were read using one script on one Arduino board. This meant the data could not be sampled at a high rate, due to high computation times. Another thing to consider is the inherent error in all measurements regarding the vehicle and its environment. The slopes were measured with a digital level and a straight edge, but the straight edge can still sit in localised hollows etc. Also, the rotational inertia of the robot is only an estimation.

Unless an accurate 3D model of a vehicle exists (or if vehicle geometry is very simple), rotational inertia is a difficult parameter to estimate accurately. Finally, it was realised that the initial conditions of the model and the actual experiments do not match for tests 1-6. The model assumes the vehicle starts on a slope, but during tests 1-6 the vehicle was actually started on a flat portion of ground at the bottom of the slope. This is a clear oversight and highlights the need to ensure initial conditions are the same.

These experiments have highlighted the difficulty of matching a theoretical model to an actual vehicle, particularly when the vehicle has not been designed for experimentation. If repeated, faster sampling rates would be used and initial conditions would be kept consistent. It is recommended that a purpose built test vehicle be used to allow greater accuracy of vehicle parameter estimation. If a purpose built vehicle was used, motors with sufficient information to build the required motor curves could be selected, and a more appropriate drive train built.

4.4 Model Validation Summary

Mixed results were obtained from the validation studies. The Solidworks Motion comparison results for the simplified dynamic model show a good match. Caster reaction forces show an excellent match between theory and measured results. Vehicle field tests did not show good agreement between theory and reality. However, the model was only going to be a rough approximation of the test due to the issues outlined regarding vehicle design, sampling rates, and initial conditions. The model in this study is deemed to be valid for design optimisation based on the Solidworks Motion and Simulink comparisons, and the caster reaction force experiment results. The simulations used to determine dimensional sensitivity and vehicle stability will now be described.

Chapter 5

Dimensional Sensitivity and Vehicle Stability: Implementation and Experimental Setup

This section describes the simulations used to analyse the effects of different vehicle dimensions on peak drive force, energy consumption and forces applied to the chassis of the vehicle. A study on the effect of caster trail and the lateral position of the COM on vehicle stability is also outlined. Over-arch vehicles intrinsically have greater rotational inertia due to the majority of structural material being positioned far from the COM. Therefore, increasing vehicle track width to gain greater turning torque may be counteracted by increased chassis inertia. The investigation of this potential issue is described. Finally, a case study conducted on Archie Junior is explained. Archie Junior was used as a test bed for all simulations, and Archie's mass, inertia and dimensions were estimated from the CAD model (Figure 5.1). Default mass, inertia and dimensions for Archie Junior can be seen in tables 5.1 and 5.2. Note, A coefficient of friction (COF) needed to be estimated for the tests. The COF for agricultural tires was estimated to be 0.7 from traction studies (vehicle was assumed to be driving on grass on firm ground) [94][95][96], and this value was used for the dynamic and static COF to achieve worst case dynamic friction. Rolling resistances of 0.09 and 0.06, and tire pressures of 5 and 11 psi

were chosen for the drive wheels and casters respectively based on wheels in a study by Petterson and Gooch [97]. As seen in section section 4.1, an angle exists that defines the point of maximum lateral caster reaction force ($\theta_{F_{11,12max}}$). This was found to be 14.5 ° for the caster wheel used in section 4.1. It was assumed this value approximated the value for both Archie Junior's and Nico Bot's caster wheels.

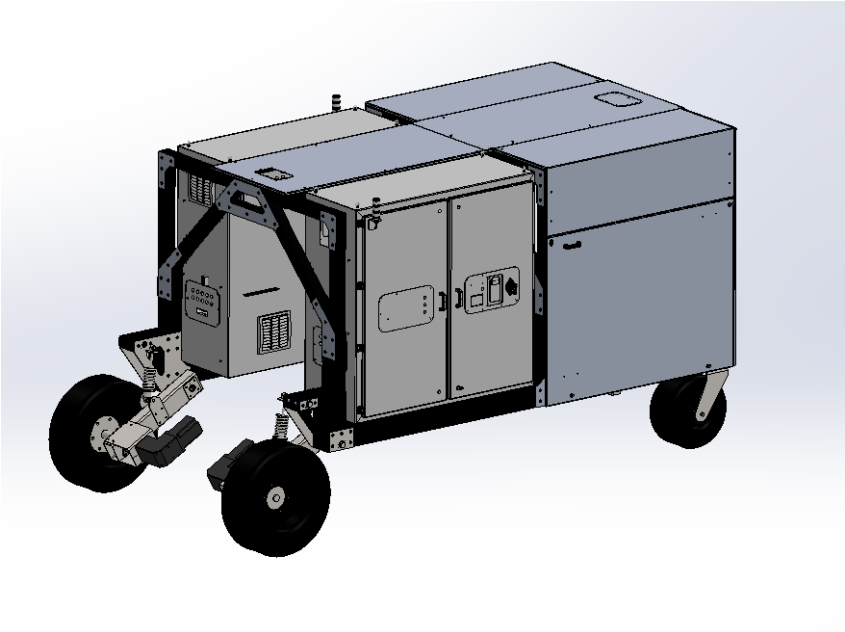

Figure 5.1: *Archie Junior CAD model.*

Table 5.1: Archie Junior dimensions. r_1 = drive wheel radius, $2L_2$ = track width of drive wheels, $2L_3$ = track width of casters, d_1 = longitudinal position of the COM, L_1 = lateral position of the COM, h_1 = height of the COM, d_4 = caster trail, and d_3 = wheel base.

r_1 (m)	$2L_2$ (m)	$2L_3$ (m)	d_1 (m)	L_1 (m)	h_1 (m)	d_4 (m)	d_3 (m)
0.38	1.882	1.514	1.632	0	1.164	0.130	3.727

Table 5.2: Archie Junior mass and inertia values. M_G = mass of vehicle, I_G = rotational inertia of vehicle about the COM, and I_w = rotational inertia of the drive wheels about the horizontal axis x_2.

M_G (kg)	I_G (kgm^2)	I_w (kgm^2)
1042	2153	2.75

5.1 Model Implementation

In this study, the model was implemented in Simulink and was solved via numerical integration. The fixed step 4th order ode Runge Kutta solver was used at an integration time step of 0.001 s.

5.2 Vehicle Trajectory

In order to study the dynamic motion of a vehicle, a trajectory needs to be chosen. Over-arch differential drive agricultural vehicles are typically designed to drive over a crop row or trellis. The vehicles are required to drive down over the trellis and turn around at the end to travel down the adjacent trellis. Therefore, an s-shaped trajectory (see Figure 5.2) was one of the trajectories selected to perform the analysis in this study. Agricultural landscapes are not always level, meaning vehicle designs need to account for slopes. The s-shaped path will be placed in 4 different orientations on a slope (Figure 5.2). Archie Junior was designed for use in vineyards. Therefore, the path was built based on vineyard dimensions, namely twice the distance between vine trellises (2 x 2.12 m, gathered from onsite measurements). Twice the distance was used because there is not enough room for the vehicle to turn down the adjacent trellis, it must turn down the next closest trellis. Note, it was assumed that there is enough room for the vehicle to directly turn around in one manoeuvre (no three-point turn) at the end of the trellis (not always the case in reality). Vineyards in New Zealand are typically grown on slopes of no more than 5 ° [98], so 5 ° was used for the sloped trajectories. Slope angle (θ_2) and path combinations can be seen in table 5.3, totaling seven trajectories.

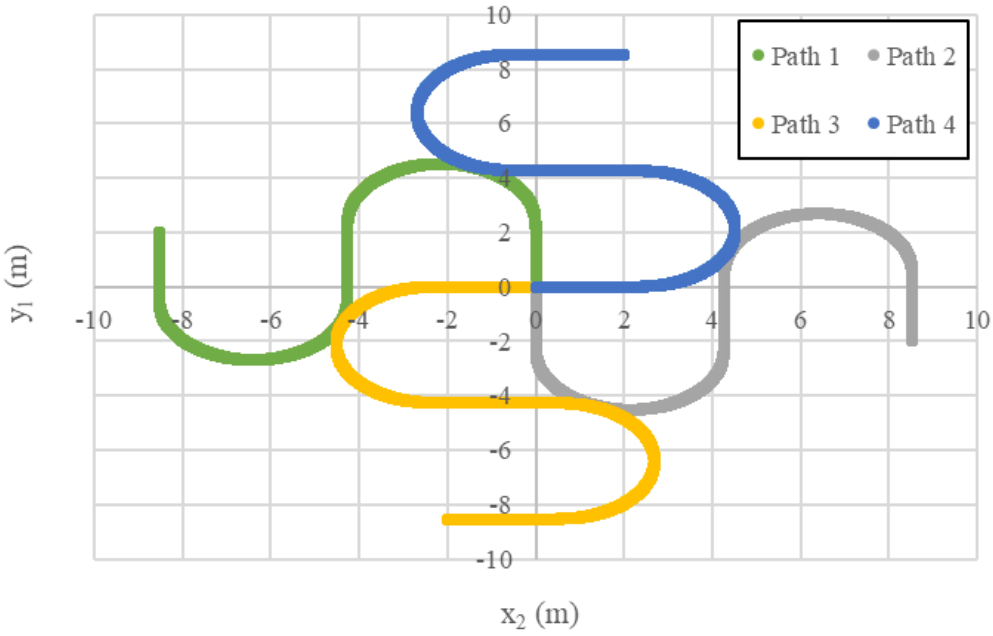

Figure 5.2: *Path 1* $\theta_{1i} = 0$, *Path 2* $\theta_{1i} = \pi$, *Path 3* $\theta_{1i} = \frac{\pi}{2}$, *Path 4* $\theta_{1i} = \frac{3\pi}{2}$

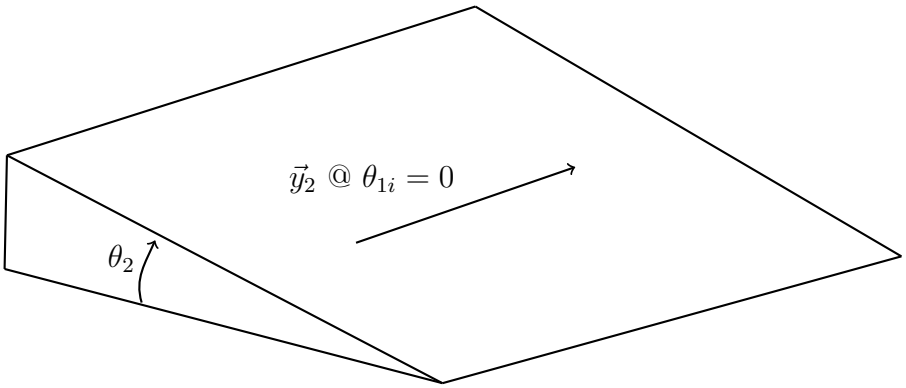

Figure 5.3: *Trajectory slope.*

Table 5.3: Vehicle trajectories for dimensional sensitivity study.

Trajectory	θ_2 (°)	Path
1	0	1
2	5	1
3	5	2
4	5	3
5	5	4
6	0	On the spot anti-clockwise
7	5	On the spot anti-clockwise

5.3 Dimensional Sensitivity Study

5.3.1 Dimensional Sensitivity of large Scale Vehicles

For this study, dimensional sensitivity is defined as the degree to which a change in a vehicle dimension affects the variable of interest (peak drive force and energy consumption etc). The key dimensions for this study were the longitudinal position of the center of mass (COM) (d_1), wheel base (d_3), the lateral position of the COM (L_1), track width ($2L_2$) and caster trail (d_4) (see Figures 3.4 and 3.5 for reference). These were incremented one at a time while the vehicle was traversing a trajectory i.e. simulations were done with a range of values for one dimension (with the range repeated for trajectories 1-7, table 5.3) while the other dimensions were kept constant at their default/actual values. For each increment of the dimension being studied, the peak drive force required from the any of the two drive wheels, the total energy consumed, and the peak forces applied to the chassis were plotted against the dimension being changed. This allowed the sensitivity of forces and energy consumption to different dimensions to be assessed. Note, peak forces means either peak drive wheel force or peak brake force. Power output is sometimes found to be negative (negative wheel torque but positive wheel rotation), meaning the vehicle gained energy due to "regenerative braking". This was left unchanged because it

is reasonable to assume large scale DDMRs will utilise regenerative braking in the future (as energy consumption is a concern). The range of values used for each dimension can be seen in 5.4. It was assumed chassis width did not change with $2L_2$ i.e. the drive wheels were extended outside or recessed into the chassis.

A linear speed of 0.13 m/s (giving an angular speed of 0.061 rad/s during each turn) was used for trajectories 1-5 with a maximum linear and angular acceleration of 0.1 m/s^2 and 0.01 rad/s^2 respectively. An angular velocity of 0.061 rad/s was used for trajectories 6 and 7 with a maximum angular acceleration of 0.01 rad/s^2. These values were chosen because 0.13 m/s was the approximate speed used when Archie Junior was first field tested. The low values of acceleration were chosen to simulate smooth operation of the vehicle. Trajectories 1 through 5 take take 160 s (real time not simulation time) to complete using the stated velocities and accelerations. Trajectories 6 and 7 were run for 106 s (to do just over one full rotation).

Table 5.4: Value ranges for used key dimensions.

Dimension	Range Values (m)
d_1	0, 0.2, 0.4.....2
d_3	2, 2.15, 2.3.....3.5
d_4	0.001, 0.04, 0.08.....0.6
L_1	0, 0.1, 0.2.....1
$2L_2$	0.4, 0.7, 1.....4

Not all values in the ranges used for the dimensions are practical in reality, and in some cases the vehicle would have tipped over i.e. $2L_2 = 0.4$. The center of mass was always kept within the boundary of the vehicles track width and wheel base, but would not be in the extreme positions tested (i.e. $L_1 = 0.9$). Extreme values were used to ensure a wide range of values were obtained, which creates a more robust trend.

5.3.2 Dimensional Sensitivity of Large Scale vs Small Scale Vehicles

Dimensional sensitivity simulations for peak drive force were also done for the Nico Bot for trajectories on which dimensions had the most influence on Archie Junior. This was done so that a comparison can be done the between large scale vehicles (Archie Junior) and smaller scale vehicles (Nico Bot). If dimensional sensitivities of both vehicles are similar, then the findings for Archie Junior can be used as a guide for smaller vehicles also. See dimension ranges in table 5.7 for the Nico Bot.

Table 5.5: Nico Bot default dimensions.

d_1 (m)	d_3 (m)	d_4 (m)	L_1 (m)	$2L_2$ (m)	$2L_3$ (m)	r_1 (m)
0.257	0.86	0.0525	0	0.836	0.552	0.167

Table 5.6: Mass, inertia and other properties of the Nico Bot.

M_G (kg)	I_G (kgm^2)	Caster Tire (kpa)	Drive Tire Pressure (kpa)
86.1	13.1	90	29

Table 5.7: Value ranges used for key dimensions of Nico Bot.

Dimensions	Range Values (m)
d_1	0, 0.075, 0.15.....0.75
d_3	0.3, 0.36, 0.42.....0.9
d_4	0.001, 0.03, 0.06.....0.45
L_1	0, 0.04, 0.08.....0.4
$2L_2$	0.2, 0.32, 0.44.....1.64

The ratio of peak drive force and initial peak drive force ($\frac{|F_{1,2max}|}{|F_{1,2max}|_i}$) was plotted against the ratios of the dimension value and default dimension ($\frac{d_1}{d_{3default}}$, $\frac{d_3}{d_{3default}}$, $\frac{d_4}{d_{4default}}$, $\frac{L_1}{L_{2default}}$ and $\frac{2L_2}{2L_{2default}}$) for both Archie Junior and Nico Bot. The dimension ratios allow the relative dimensions of the vehicles to be taken into account, and creates a better comparison. $d_{3default}$ was chosen for the d_1 ratio and d_3 ratio because they are a good indication of vehicle size and are in the same direction as d_1 and d_3. $L_{2default}$ was chosen for the L_1 ratio and $2L_2$ for the $2L_2$ ratio for the same reason. $d_{4default}$ is also an indicator of vehicle size, but not to the same degree. However, it was chosen for consistency.

5.4 Chassis Loading and Vehicle Instability Study

From section 4.1 it is clear caster trail has an effect on the magnitudes of caster reaction forces. As observed in current DDMR's at the university, these forces can cause chassis deformation and vehicle instability. So, in this study, the Simulink vehicle was driven forward with worst case caster angles, and maximum vehicle deviation and maximum chassis loading were analysed. The effect of the lateral position of the COM on stability was also assessed.

For the caster trail vs stability test, a drive force of 850 N was applied to each drive wheel for 6 s with a range of casters trail values with the vehicle in four different initial orientations (table 5.8, Figure 5.4). The different orientations were to compare stability with casters leading and casters trailing (caster positions are represented by thick black lines). Maximum deviations of x_1 and θ_1 were plotted against caster trail. Sample trajectories from the tests were also plotted. x_1 and θ_1 are the global lateral coordinate and vehicle heading respectively.

Table 5.8: Caster trail vs vehicle stability test parameters. d_4 = caster trail, F_1 and F_2 = drive force for the left and right drive wheels respectively, $\theta_{5,6i}$ = initial caster positions, and θ_{1i} initial = vehicle heading.

Test	d_4 (m)	F_1 (N)	F_2 (N)	$\theta_{5,6i}$ (°)	θ_{1i} (°)
1	0.1, 0.15, 0.2, 0.25....1	850	850	175	0
2	0.1, 0.15, 0.2, 0.25....1	850	850	185	0
3	0.1, 0.15, 0.2, 0.25....1	-850	-850	-5	180
4	0.1, 0.15, 0.2, 0.25....1	-850	-850	5	180

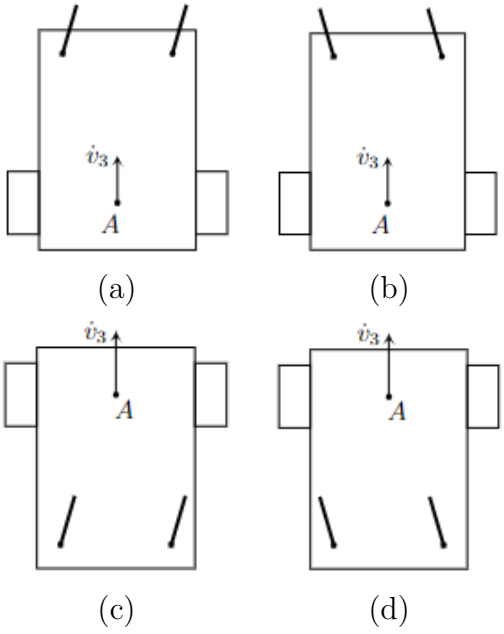

Figure 5.4: *Initial vehicle and caster orientations. (a) for test 1. (b) for test 2. (c) for test 3. (d) for test 4.*

To analyse the effect of the COM position on stability, drive forces of 447.3 N were applied to the vehicle for 14.14 s. This was done so that a default trajectory of 10 m was achieved with L_1 in its default position ($L_1 = 0$). The vehicle was then positioned in two different orientations (Figure 5.5) and the same drive forces were applied for 14.14 s with different values of L_1. Details for the tests can be seen in table 5.9. Maximum deviations of x_1 and θ_1 were plotted against L_1. Sample trajectories from the tests were also plotted.

Table 5.9: Lateral position of the COM vs vehicle stability test parameters. L_1 = lateral position of the COM, F_1 and F_2 = drive force for the left and right drive wheels respectively, $\theta_{5,6i}$ = initial caster positions, and θ_{1i} initial = vehicle heading.

Test	L_1 (m)	F_1 (N)	F_2 (N)	$\theta_{5,6i}$ (°)	θ_{1i} (°)
1	0.1, 0.2, 0.3, 0.4....0.9	447.3	447.3	0	0
2	-0.1, -0.2, -0.3, -0.4....-0.9	447.3	447.3	0	0
3	-0.1, -0.2, -0.3, -0.4....-0.9	-447.3	-447.3	180	180
4	0.1, 0.2, 0.3, 0.4....0.9	-447.3	-447.3	180	180

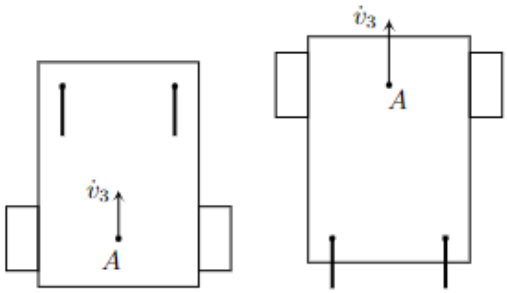

(a) (b)

Figure 5.5: *Vehicle orientations for tests 1-4. (a) for tests 1 and 2 (COM leading). (b) for tests 3 and 4 (COM trailing).*

To assess maximum differential caster loads on the vehicle chassis, drive forces were applied to accelerate the vehicle at 0.1 m/s^2, with the casters placed in two initial positions, turned in (Figure 5.6a) and turned out (Figure 5.6b). Exact caster angles can be seen in table 5.10. Maximum negative and positive values of F_{18} were plotted against caster trail for both orientations. A negative force means the frame is being splayed, and a positive force means the frame is being compressed.

Table 5.10: Worst case chassis loading tests parameters. θ_{5i} = initial position of left caster and θ_{6i} = initial position of right caster.

Test	d_4 (m)	θ_{5i} (°)	θ_{6i} (°)
1	0.001, 0.01, 0.03, 0.06.....0.3	175	185
2	0.001, 0.01, 0.03, 0.06.....0.3	185	175

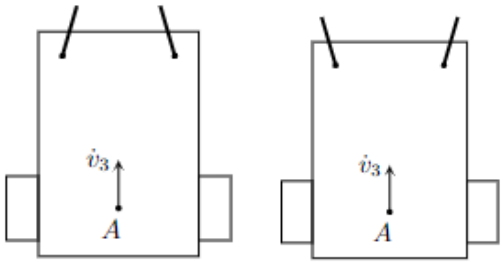

(a) (b)

Figure 5.6: *Initial caster positions for Tests 1 (a) and 2 (b).*

5.5 Chassis Inertia Study

The effect of track width on required drive forces will be assessed in this section. This is different to section 5.3 because the track with ($2L_2$) was changed without adjusting the total width of the vehicle (thus rotation inertia was left unchanged). In this study, an over-arch frame was mocked up in Solidworks (Figures 5.7a and 5.7b) and each time the track width was incremented the frame width was also increased and the new rotational inertia was computed. The vehicle was accelerated anticlockwise on the spot at 0.01 rad/s^2 at each different track width and chassis combination with zero slope angle, and peak drive forces were then plotted against track width. See table 5.11 for track width and inertia values etc. The initial track width of the casters was taken to be the same as the drive wheels ($2L_2 = 2L_3$), and the initial width of the chassis was taken to be the same as the caster track width ($2L_3$). The simulations were then repeated, but the chassis width and inertia was not increased with track width (see table 5.12).

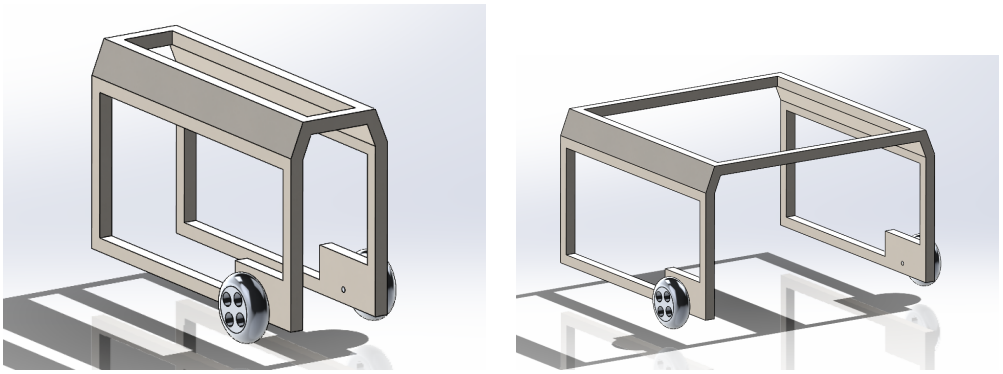

(a) (b)

Figure 5.7: *Most narrow (a) and most wide (b) chassis width.*

Table 5.11: Effect of chassis inertia on peak drive force test 1 parameters (varying chassis width, mass and inertia). $2L_2$ = drive wheel track width and $2L_3$ = caster track width.

$2L_2$ (m)	$2L_3$ (m)	d_1 (m)	I_G (kgm^2)	M_G (kg)
1.05	1.05	0.71	738.75	936.97
1.25	1.25	0.71	826.48	947.77
1.45	1.45	0.72	933.16	958.57
1.65	1.65	0.72	1059	969.37
1.85	1.85	0.72	1204.23	980.17
2.05	2.05	0.72	1369.06	990.97
2.25	2.25	0.72	1553.71	1001.77
2.45	2.45	0.72	1758.38	1012.57
2.65	2.65	0.72	1983.31	1023.37
2.85	2.85	0.73	2229.4	1034.51

Table 5.12: Effect of chassis inertia on peak drive force test 2 parameters (constant chassis width, mass and inertia). $2L_2$ = drive wheel track width and $2L_3$ = caster track width.

$2L_2$ (m)	$2L_3$ (m)	d_1 (m)	I_G (kgm^2)	M_G (kg)
1.05	1.05	0.71	738.75	936.97
1.25	1.05	0.71	738.75	936.97
1.45	1.05	0.72	738.75	936.97
1.65	1.05	0.72	738.75	936.97
1.65	1.05	0.72	738.75	936.97
1.85	1.05	0.72	738.75	936.97
2.05	1.05	0.72	738.75	936.97
2.25	1.05	0.72	738.75	936.97
2.45	1.05	0.72	738.75	936.97
2.85	1.05	0.73	738.75	936.97

5.6 Archie Junior Case Study

In this study, the limitations of Archie Junior were estimated with it's default dimensions, and the vehicle was optimised if it failed to perform the desired trajectory. The vehicle was tested on level and sloped ground. The points at which the drive force required was greater than the maximum drive forces available from the motors were investigated, as well as the points where the vehicle lost traction. Key dimensions were adjusted if the vehicle failed to perform. Maximum drive force required was typically observed when the vehicle was turning on the spot (from dimensional sensitivity study), so trajectories 6 and 7 were used for this study. As this portion of the study was analysing the limitations of the vehicle, a low COF was used to obtain a worse case traction scenario. A COF of 0.37 was used based on traction studies assuming the vehicle is driving on soft/wet soil [96][99][100][101]. The gearbox used for each motor on Archie Junior has an efficiency of approximately 95%. To account for uncertainties in the efficiencies of other drive train components, an efficiency of 80% was used for the analysis.

5.7 Implementation and Experimental Setup Summary

The simulations conducted for dimensional sensitivity, vehicle stability, vehicle optimisation, and the effect of chassis inertia have now been described. The following chapter presents and analyses study results.

Chapter 6

Dimensional Sensitivity and Vehicle Stability: Analysis

In this chapter, results are analysed and discussed. The results include dimensional sensitivity, vehicle stability, chassis loading and the effect of increasing inertia with track width.

6.1 Dimensional Sensitivity Study

6.1.1 Peak Drive Force

The effect of a change in the longitudinal position of the COM on peak drive/brake force ($|F_{1,2max}|$) can be seen in Figure 6.1. Increasing the longitudinal distance (d_1, see Figure 6.2) between the COM and the point between the drive wheels (point A) causes an increase in the peak drive/brake force required from any of the two drive wheels. These results are similar to results in the study by Huang and Sprigle [58]. The relationship is non-linear, which is expected due to d_1 being raised to the power of 2 in the model (due to the parallel axis theorem). This means the COM should be kept close to point A to enable the vehicle to turn more easily. The vehicle is most sensitive to d_1 on trajectories

6 and 7. The angles of the casters relative to longitudinal axis of the chassis (θ_9 and θ_{10}, see Figure 6.3) are at much higher values on these trajectories, meaning lateral reaction forces ($F_{11,12}$) are higher. Increasing d_1 puts more load on the casters (increasing reaction forces even further) and it also gives gravitational forces from the slope a greater lever arm to act upon about point A, creating a larger torque on the vehicle. Therefore, d_1 should be kept small. These sensitivity observations also provide insight into DDMR configuration. To reduce peak drive forces as much as possible, d_1 should be 0. However, in this condition, the vehicle will tip over backwards as soon as it accelerates forward. However, if the drive wheels are placed in the center of the chassis and two casters placed at the front and back of the vehicle (giving a total of 4 casters), this would make $d_1 = 0$ while preventing the vehicle from tipping. After this, the main decision left is whether to put suspension on the casters or drive wheels.

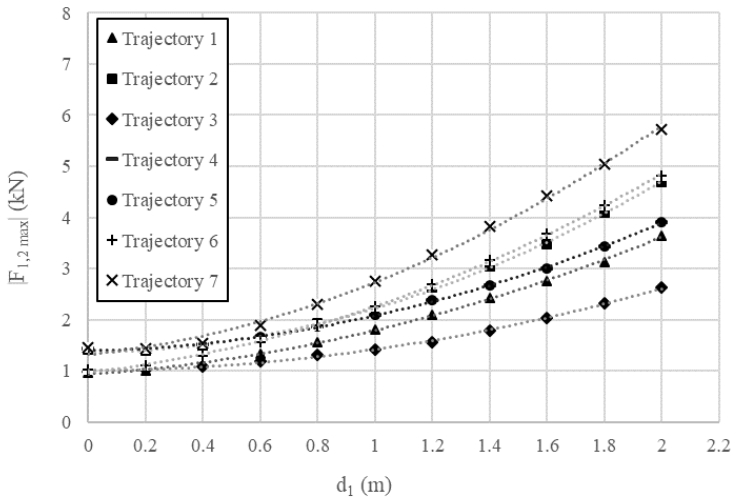

Figure 6.1: *Peak drive force vs longitudinal position of the COM (d_1) for trajectories 1-7.*

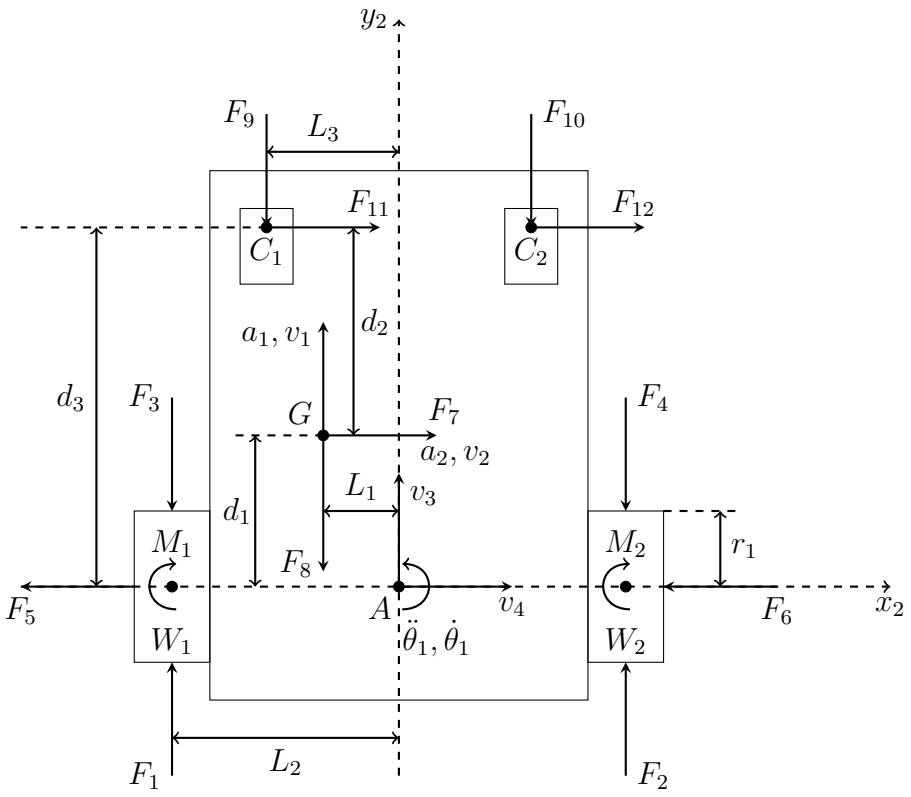

Figure 6.2: *Dimensions for reference.*

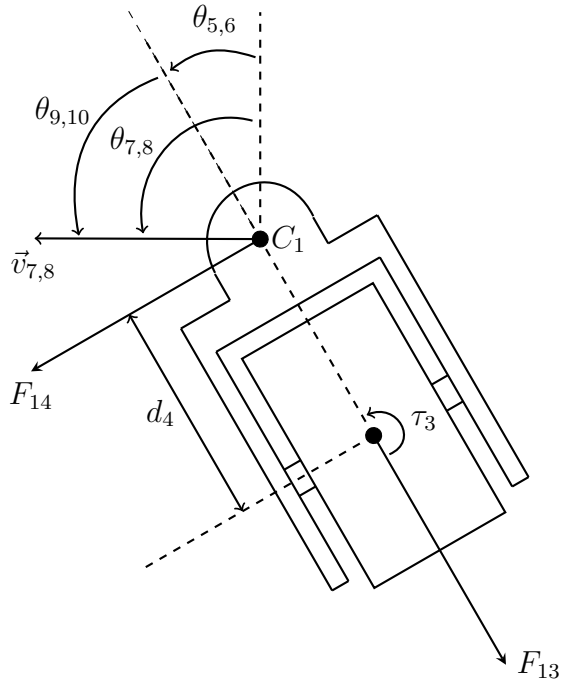

Figure 6.3: *Caster angles for reference.*

Increments of vehicle wheel base (d_3) generate a small increase in peak drive forces for trajectories 1-5, but cause a decrease for trajectories 6 and 7 (Figure 6.4). Increasing d_3 creates a longer lever arm for caster reaction forces to act upon, thus increasing drive forces required. However, increasing d_3 also reduces the load on the casters. Reduced loading on the casters gives a greater decrease in caster reaction forces when θ_9 and θ_{10} are large (trajectories 6 and 7), and if this decrease is more significant than the increase from the longer lever arm, it explains the reduction of peak drive force on trajectories 6 and 7. The relationship is slightly non-linear on trajectories 6 and 7, which is expected because the caster loads are risen to the power of 1.5 in tire reaction torque calculation (equation (3.48)). So, d_3 should generally be kept on the longer side.

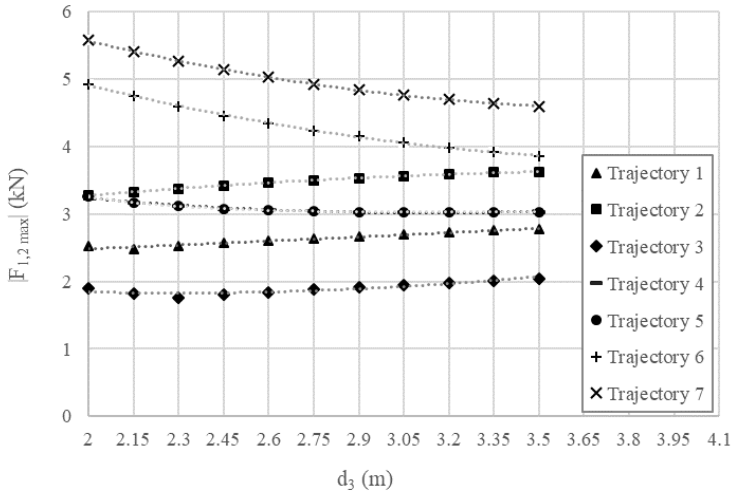

Figure 6.4: *Peak drive force vs wheel base (d_3) for trajectories 1-7.*

The sensitivity of peak drive force to changes in caster trail (d_4, Figure 6.3) is seen in Figure 6.5. Increases of d_4 decrease forces required. This results agrees with Kauzlarich et al [3]. Again, due to θ_9 and θ_{10} being larger for trajectories 6 and 7, the vehicle is far more sensitive to d_4 on these trajectories. A non-linear relationship is observed. This is no surprise considering a factor of $\frac{1}{d_4}$ is found in the model describing the caster reaction forces (equation (3.46)). Based on these results, d_4 should be kept larger to reduce peak drive forces. It should be noted that this study does not take caster shimmy into consideration, and it should not be ignored when choosing a caster trail value.

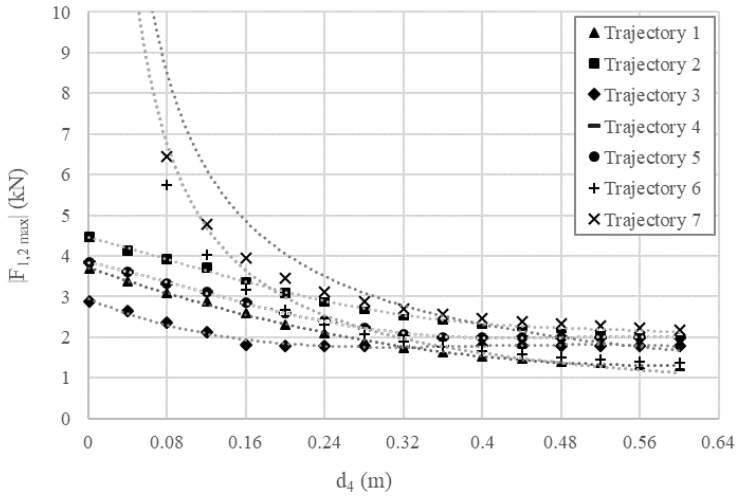

Figure 6.5: *Peak drive force vs caster trail (d_4) for trajectories 1-7.*

Similar to d_1, increasing the lateral position of the COM (L_1, Figure 6.2) increases peak drive force required in a non linear fashion(Figure 6.6). Increasing L_1 shifts load to one side of the vehicle, creating more resistance to motion on that side (due to increased friction force and rolling resistance, as well imbalanced inertia), thus increasing peak drive force required from the wheel on that side. Gravitational forces generate a larger moment on the vehicle with larger values of L_1. Based on these observations, the lateral position of the COM should be kept as central as possible.

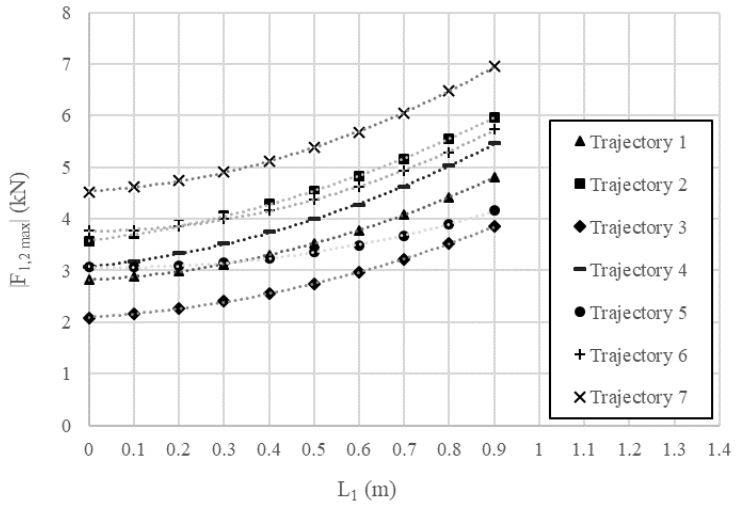

Figure 6.6: *Peak drive force vs lateral position of the COM (L_1) for trajectories 1-7.*

The effect of changing vehicle track width ($2L_2$) on peak drive force is seen in Figure 6.7. Increases of track width cause a decrease in peak drive force in a non-linear fashion because a factor of $\frac{1}{L_2}$ is in the dynamic model (equation (3.37)). Note, for practical reasons, $2L_2$ would ever be as small as 0.4 m for a vehicle the size of Archie Junior, so the influence is not practically as high as the trend suggests (the same goes for d_4, which would never be as small as 1mm). Track width should clearly be kept as wide as practically possible to reduce peak drive forces.

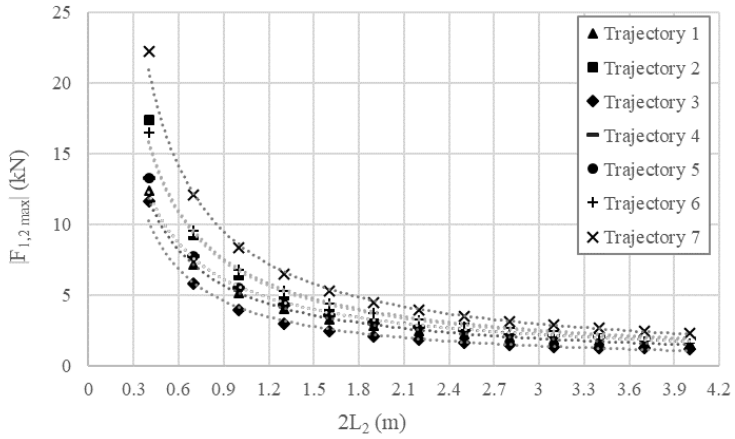

Figure 6.7: *Peak drive force vs track width ($2L_2$) for trajectories 1-7.*

All dimensional sensitivities can been seen compared in Figure 6.8 for trajectory 1. Trajectory 1 is expected to be a very common trajectory for over-arch DDMRs in a level vineyard. When determining the relative influences of different dimensions, it is done by looking at the influence of the dimensions close to their default values. This is done because in many cases the upper and lower values tested would not be practical in reality. Therefore, when discussing relative sensitivities, points on the trend lines close to default values are being analysed.

From greatest to least, the order of dimensions with regard to dimensional sensitivity for peak drive force on trajectory 1 is d_4, d_1, $2L_2$, L_1, and d_3. Note, the default value for L_1 is approximately zero (and is not likely to move around much), making its practical influence much lower than an initial glance at the trend suggests. These results show that for trajectories such as trajectory 1, d_4 should be optimised first.

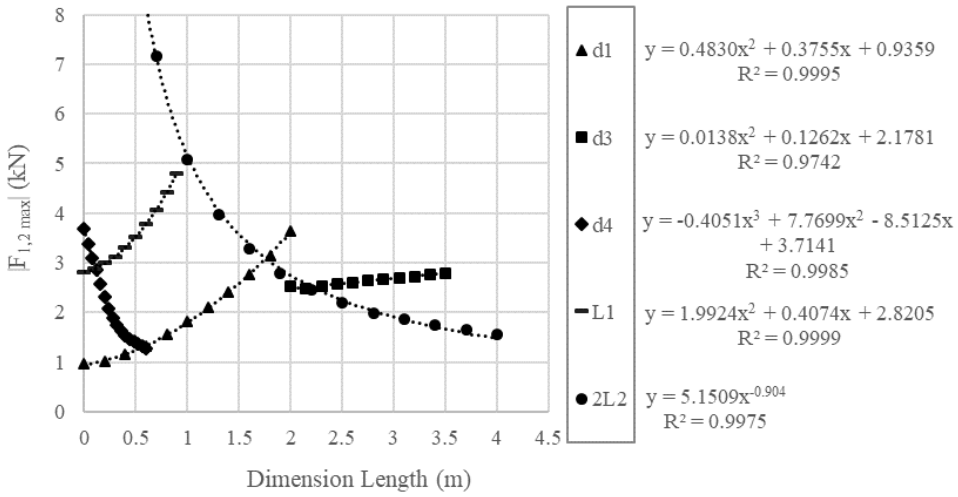

Figure 6.8: *Peak drive force vs dimension length for trajectory 1 for dimensions* d_1*,* d_3*,* d_4*,* L_1 *and* $2L_2$*.*

The trajectories on which d_1, d_3, d_4, L_1 and $2L_2$ are most influential are 7, 6, 6, 4, and 7 respectively. Trajectories 2-7 represent the rest of expected trajectories in a vineyard (including vineyards with slopes up to 5 °). From greatest to least, the order of dimensions with regard to dimensional sensitivity for peak drive force on trajectory 1 is d_4, d_1, $2L_2$, L_1, and d_3 (Figure 6.9). Therefore, sensitivities are in the same order as trajectory 1, with the notable difference being d_4 and d_3. d_4 has a much higher influence at lower values. This is due to θ_9 and θ_{10} having greater values on trajectory 6 (see Figure 6.3 for a reminder of caster angle definition). The influence of d_3 has changed direction (see discussion of Figure 6.4 for the explanation). So, d_4 should be adjusted first to reduce peak drive forces, followed by d_1 and then $2L_2$. Very small values of d_4 should definitely be avoided. To illustrate the significance of these dimensional sensitivities, increasing d_4 from 0.13 to 0.33 m, decreasing d_1 from 1.632 to 1.432 m, and increasing $2L_2$ from 1.882 to 2.082 m provides a decrease in peak drive force of 56.4 %, 13.9 %, and 9.37 % respectively.

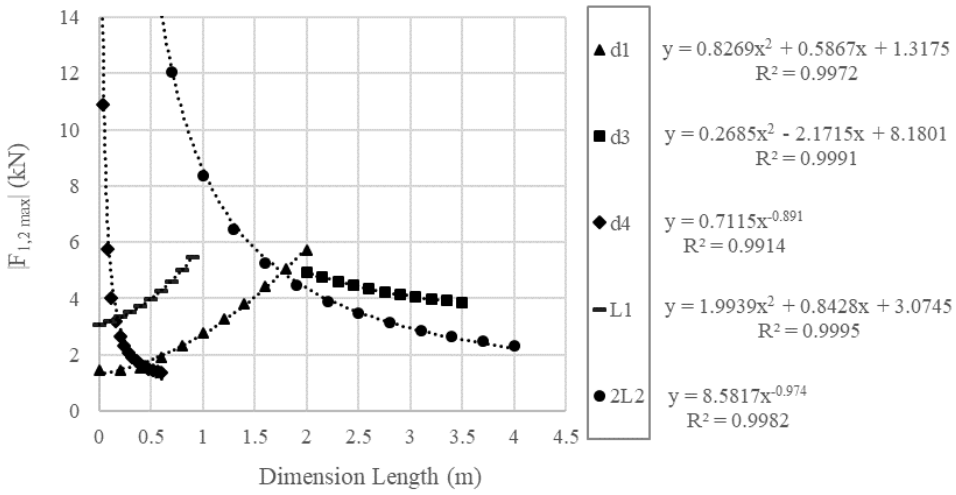

Figure 6.9: *Peak drive force vs dimension length for each dimension (d_1, d_3, d_4, L_1 and $2L_2$). The plot for each dimension was taken from the trajectory on which the dimension had the highest influence.*

6.1.2 Energy Consumption

Total energy consumed drops as d_1 is increased for trajectories 1-5, but overall the influence is low (Figure 6.10). This decrease in energy consumption is not expected, because an increase in d_1 increases the rotation inertia of the vehicle about point A, which should increase energy consumed during the periods of angular acceleration. When $d_1 = 0$, all of the vehicle's weight is on the drive wheels. It could be that total frictional forces and rolling resistances (non-conservative forces) are greater in this condition (larger tire contact patch etc) and are reduced as more weight is shifted onto the casters via an increase of d_1. Energy consumption goes up on trajectories 6 and 7, which makes more sense because θ_9 and θ_{10} are larger and therefore caster reaction forces are higher. Based on these observations d_1 should generally be increased to reduce energy consumption.

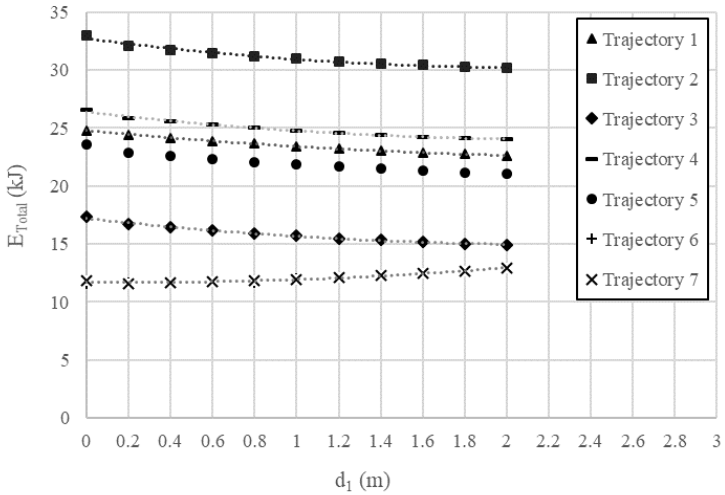

Figure 6.10: *Total energy consumed vs longitudinal position of the COM (d_1) for trajectories 1-7.*

The influence of d_3 on energy consumed can be seen in Figure 6.11. It is observed that increases of d_3 generate an increase in total energy consumption. Increases in d_3 create a longer lever arm for the caster frictional forces to resist vehicle rotation, increasing energy consumption. Also, more weight is shifted onto the drive wheels, potentially increasing total friction forces due to an increase of drive wheel contact patch radius. It is assumed that d_3 shifts independently from the main chassis, so d_1 is assumed to be constant, which is why more weight is shifted onto the drive wheels as d_3 is increased. The relationship is slightly non-linear, which is due to the reaction torque calculation for the casters and drive wheels (equations (3.48) and (3.61)). Based on these observations d_3 should be kept small to reduce energy consumption.

Energy consumption increases with d_4, though the amount is negligible (Figure 6.12). This small increase is no surprise. As d_4 is increased the casters take longer to reach an equilibrium position after a change in direction (θ_9 and θ_{10} take longer to reduce in magnitude), meaning the frictional reaction forces have an effect for longer periods of time. Therefore, changing d_4 is a poor way to reduce energy consumption.

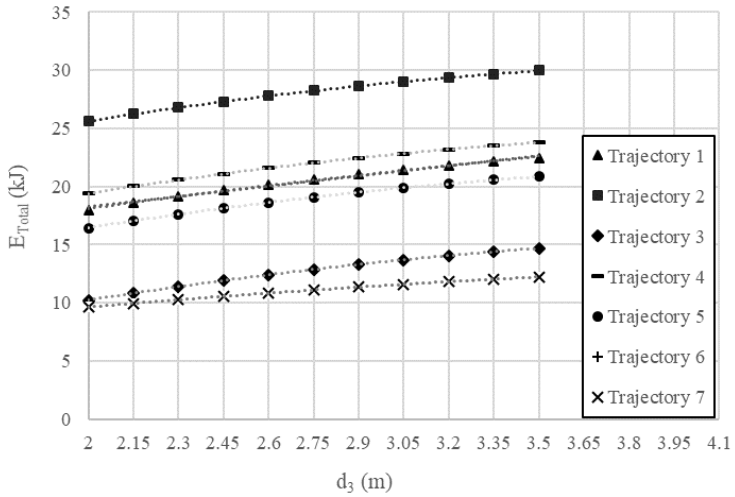

Figure 6.11: *Total energy consumed vs wheel base (d_3) for trajectories 1-7.*

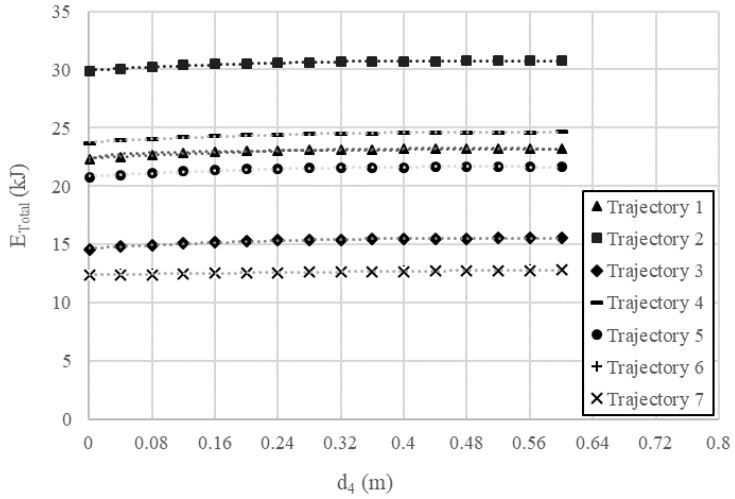

Figure 6.12: *Total energy consumed vs caster trail (d_4) for trajectories 1-7.*

A small increase in energy consumption is observed as L_1 increases (Figure 6.13). This is expected because of the parallel axis theorem describing the rotational inertia of the vehicle. Due to the low influence, changing L_1 is not a good optimisation strategy with regards to energy consumption.

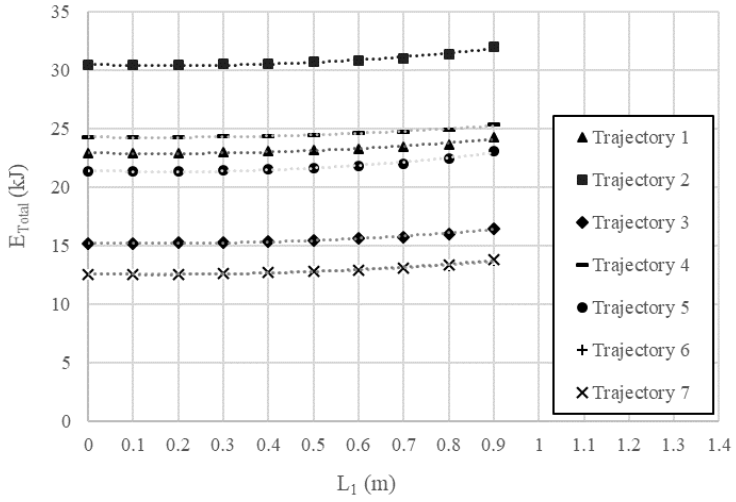

Figure 6.13: *Total energy consumed vs lateral position of the COM (L_1) for trajectories 1-7.*

The sensitivity of total energy consumption to $2L_2$ can be seen in Figure 6.14. No significant increase or decrease in energy consumed is observed for trajectories 1-5. However, a steep increase is observed for trajectories 6 and 7 (trend for 6 hidden behind 7). This is due to the fact that drive wheel rolling resistances have a greater lever arm to act upon and resist the rotation of the vehicle as $2L_2$ is increased. Trajectories 6 and 7 are purely rotational (not made up of curved and liner sections like the other trajectories), thus any extra non-conservative resistances to rotation will increase total energy consumption significantly. Therefore, significant gains in energy reduction can be obtained by reducing $2L_2$ if trajectories of pure rotation are common.

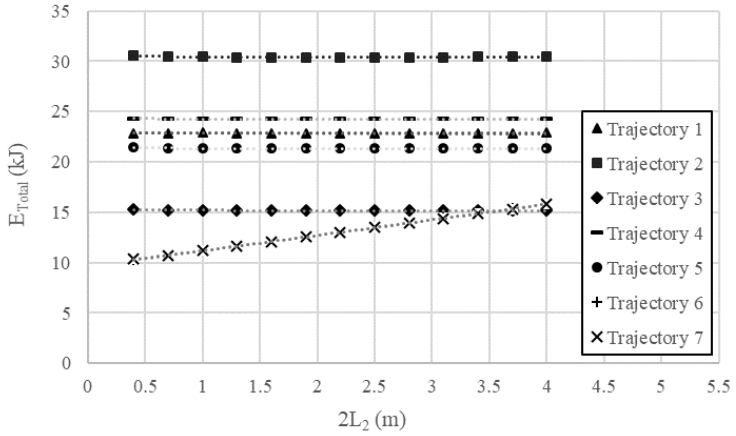

Figure 6.14: *Total energy consumed vs track width ($2L_2$) for trajectories 1-7.*

From greatest to least, the order of dimensions with regard to dimensional sensitivity for energy consumption on trajectory 1 is d_3, d_4, d_1, L_1, and $2L_2$. Therefore, in order to reduce energy consumption on trajectory 1, wheel base (d_3) should be reduced first.

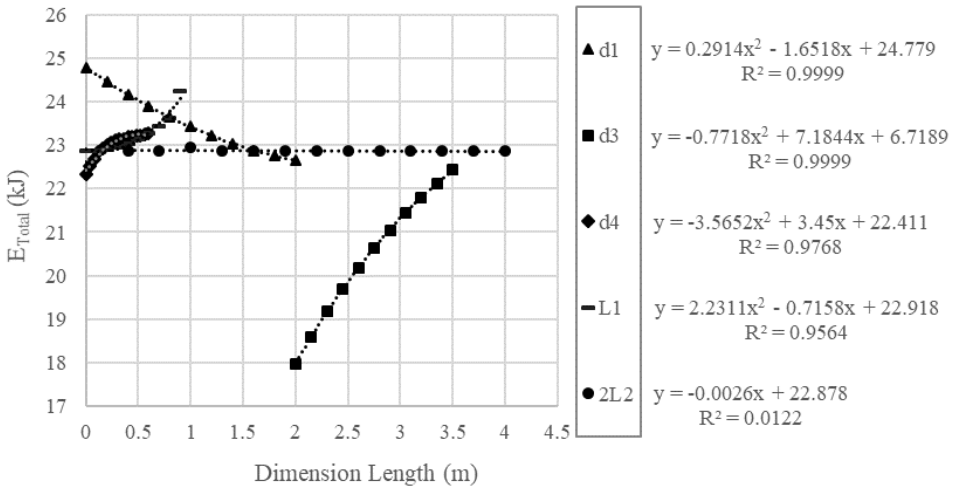

Figure 6.15: *Total energy consumed vs dimension length for trajectory 1 for dimensions d_1, d_3, d_4, L_1 and $2L_2$.*

The trajectories on which d_1, d_3, d_4, L_1 and $2L_2$ are most influential are 2, 3, 4, 3, and 7 respectively (though a lot of them are very similar). Ranked from highest to lowest, the dimensions with the most practical influence are d_3, $2L_2$, d_4, d_1, and L_1 (Figure 6.16). This means that d_3 should be adjusted first to reduce energy consumption, with $2L_2$ a close second. Decreasing d_3 from 3.5 to 3.3 m provides a reduction of 2.73 %. Increasing $2L_2$ from 1.882 to 2.082 m gives an increase in energy consumption of 2.44 %. These values are not trivial because over long duty cycles (which is likely for agricultural DDMRs) they could reduce energy consumption significantly, reducing cost and emissions (reduction in emissions will vary depending on the source of electricity generation for charging).

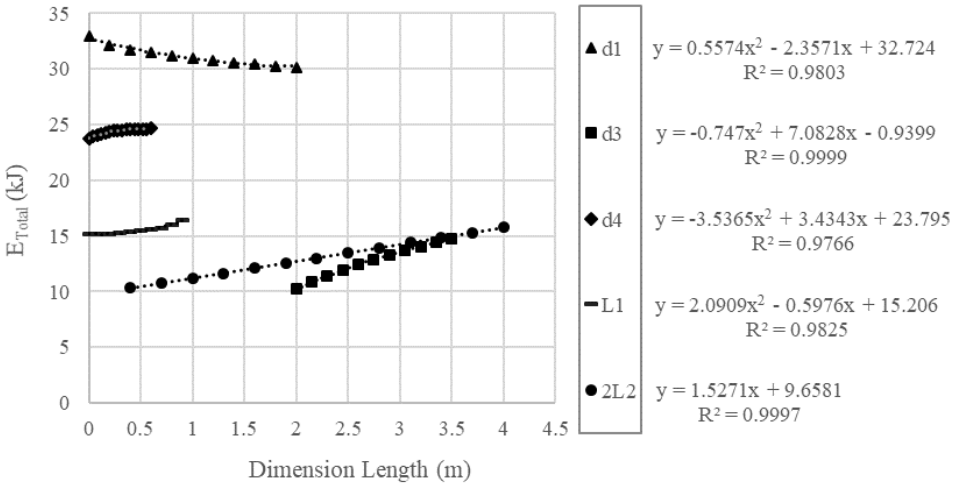

Figure 6.16: *Total energy consumed vs dimension length for each dimension (d_1, d_3, d_4, L_1 and $2L_2$). The plot for each dimension was taken from the trajectory on which the dimension had the highest influence.*

6.1.3 Peak Shear Force on Chassis

The effect of increasing d_1 can be seen in Figure 6.17. Increasing d_1 increases peak shear forces ($|F_{17max}|$) in a non-linear fashion. This is no surprise because peak values for F_{17} always occurred during periods of angular acceleration, and increases in d_1 cause a non-linear increase in rotational inertia. Therefore, to reduce stresses in the frame and excess deflection, d_1 should be kept low. If less stress is induced, a lighter less stiff chassis can be used, reducing energy consumption and material costs.

Increments of d_3 generate an increase in shear force for trajectories 1-5, but cause a decrease for trajectories 6 and 7 (Figure 6.18). The reasons for the difference will be very similar to the peak drive force because F_{17} is very closely linked with F_1 and F_2 (equation (3.77)). Increasing d_3 creates a longer lever arm for caster reaction forces to act upon, thus increasing drive forces required. However, shifting d_3 also reduces the load on the casters. Reduced loading on the casters gives a greater decrease in caster reaction forces when θ_9 and θ_{10} are large (trajectories 6 and 7), and if this decrease is more significant than the increase from the longer lever arm, it explains the reduction of shear force on trajectories 6 and 7. The relationship is non-linear on trajectories 6 and 7, which is expected because wheel loads are risen to the power of 1.5 in the caster and drive wheel reaction torque

calculation (equations (3.48) and (3.61)). So, for trajectories similar to 6 and 7, d_3 should be kept on the longer side to reduce twisting of the frame. For trajectory 1, d_3 should be kept smaller.

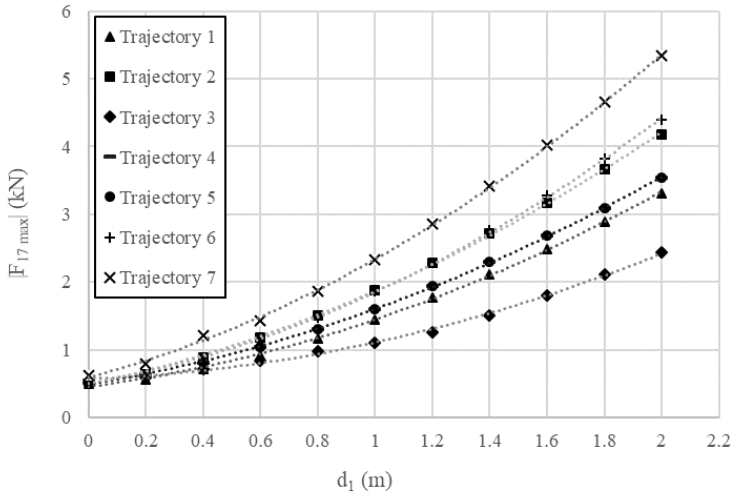

Figure 6.17: *Peak shear force on chassis vs longitudinal position of the COM (d_1) for trajectories 1-7.*

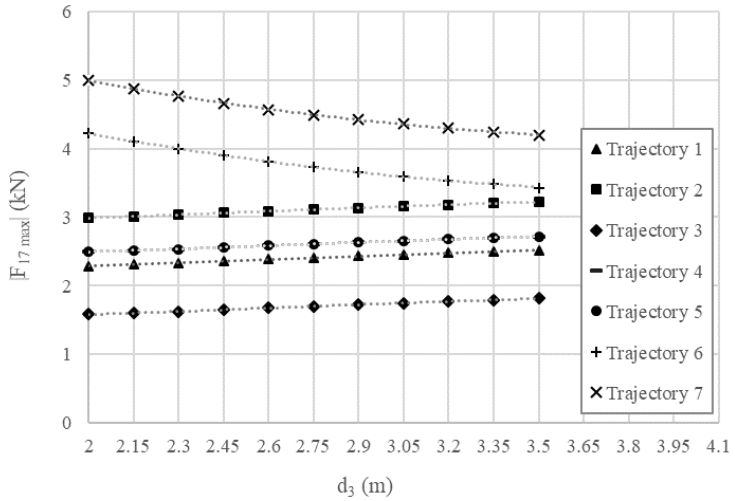

Figure 6.18: *Peak shear force on chassis vs wheel base (d_3) for trajectories 1-7.*

The influence of d_4, L_1 and $2L_2$ on peak shear force can be seen in Figures 6.19-6.21. It can be seen that their affect on peak shear force is very similar to their effect on peak drive force, and the reasons for their behaviour will be the same. Therefore, to reduce shear forces on the frame, d_4 should be kept larger, L_1 smaller, and $2L_2$ larger.

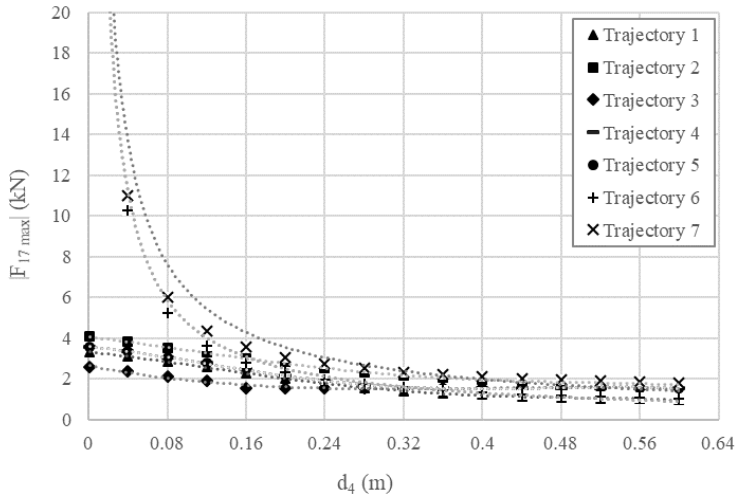

Figure 6.19: *Peak shear force on chassis vs caster trail (d_4) for trajectories 1-7.*

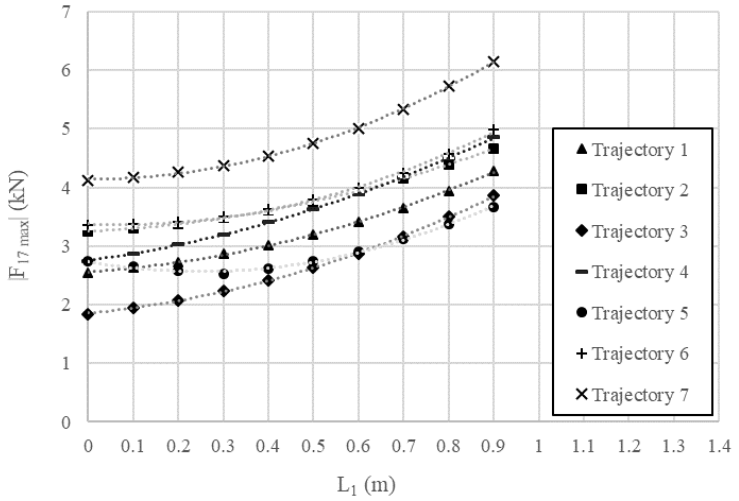

Figure 6.20: *Peak shear force on chassis vs lateral position of the COM (L_1) for trajectories 1-7.*

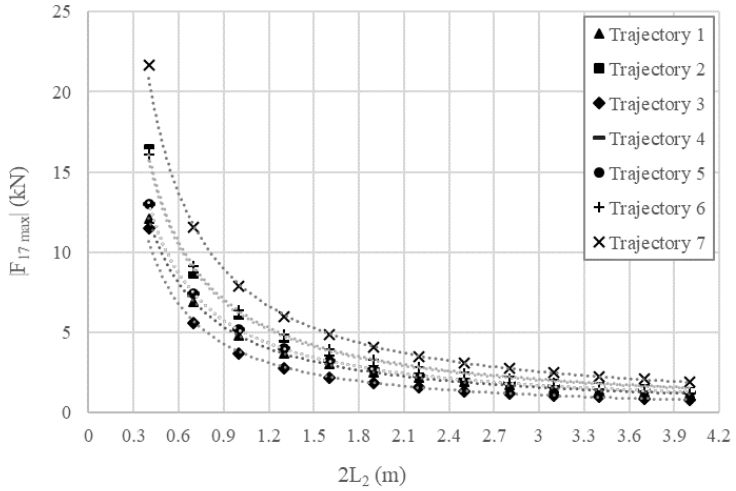

Figure 6.21: *Peak shear force on chassis vs track width ($2L_2$) for trajectories 1-7.*

From greatest to least, the order of dimensions with regard to dimensional sensitivity for peak shear force on trajectory 1 is d_4, d_1, $2L_2$, L_1, and d_3 (Figure 6.22). This is expected because the the trend for d_4 is very steep around the default value (0.13 m), and d_1 increases the rotational inertia of the vehicle. Therefore, in order to reduce peak shear force on trajectory 1, caster trail (d_4) should be reduced first, followed by d_1.

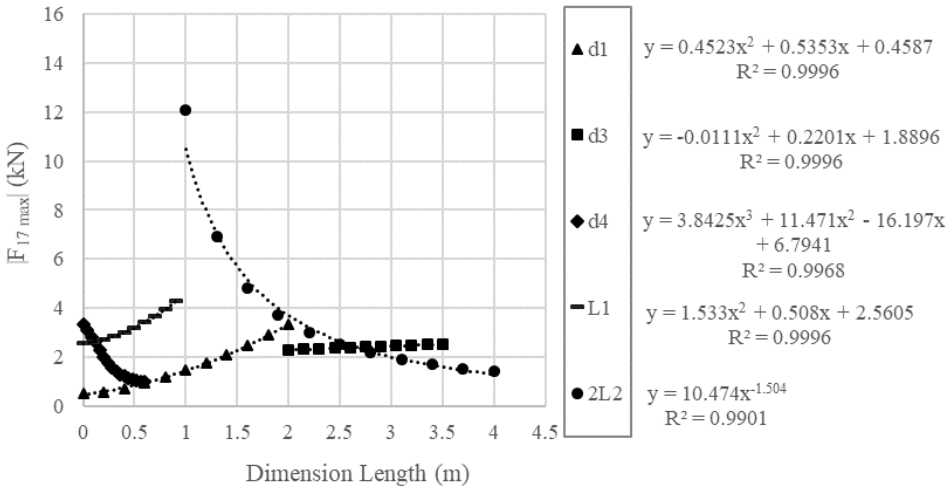

Figure 6.22: *Peak shear force vs dimension length for trajectory 1 for dimensions d_1, d_3, d_4, L_1 and $2L_2$.*

The trajectories on which d_1, d_3, d_4, L_1 and $2L_2$ are most influential are 7, 6, 6, 3, and 7 respectively. Sensitivities for the dimensions of the vehicle are similar to trajectory 1. Ranked highest to lowest, the order of dimensions with regard to dimensional sensitivity

for peak shear force across trajectories 2-7 is d_4, d_1, L_1, $2L_2$ and d_3 (Figure 6.23). Wheel base now has a more significant affect (compared to trajectory 1) but is inverted, and L_1 now has more influence than $2L_2$. Increasing d_4 from 0.13 to 0.33 m, and decreasing d_1 from 1.632 to 1.432 m, creates a decrease in peak shear force of 58.0 % and 15.0 %respectively. Increasing L_1 from 0 to 0.2 m generates an increase of 11.3 %. Based on these results, caster trail should be adjusted first, followed by d_1.

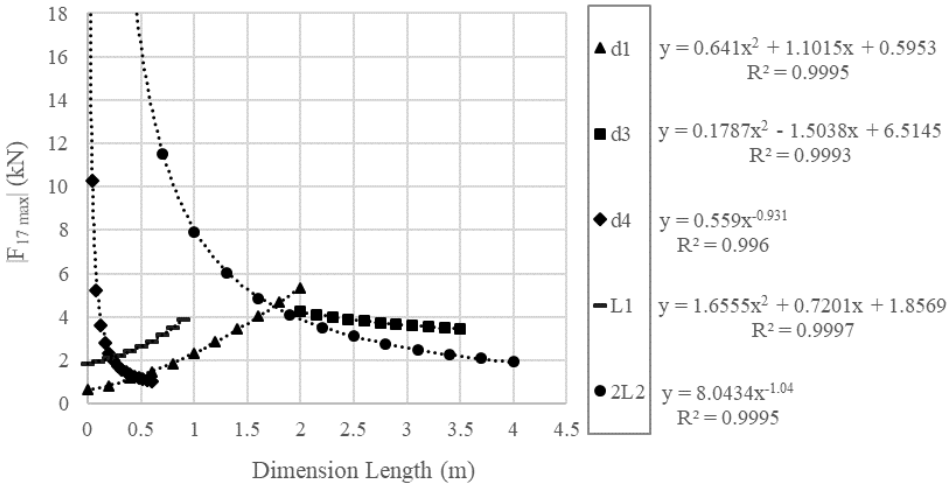

Figure 6.23: *Peak shear force on chassis vs dimension length for each dimension (d_1, d_3, d_4, L_1 and $2L_2$). The plot for each dimension was taken from the trajectory on which the dimension had the highest influence.*

6.1.4 Peak Splay Force on Chassis

The sensitivity of peak splay/compression force to increases in d_1 is seen in Figure 6.24. peak splay force increases with d_1 in a linear and non-liner fashion. Caster reaction forces increase as increases of d_1 place a higher load on the front of the vehicle. If this was the only change, $|F_{18max}|$ should stay constant as it is calculated from the difference between the lateal reaction forces F_{11} and F_{12} (equation (3.78)). However, if the vehicle is in a turn, centripetal forces cause more load to be distributed to the outside of the vehicle, and if the center of mass is moved forward by increasing d_1, more load is put onto the front outside caster, thus increasing the difference between caster reaction forces. This explains the increase of $|F_{18max}|$. So, to reduce splay forces and lateral deflection of the chassis, d_1 should be kept small.

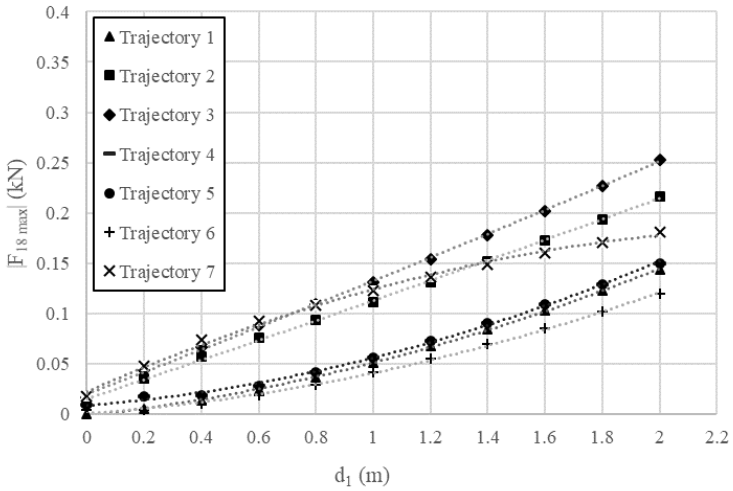

Figure 6.24: *Peak splay force on chassis vs longitudinal position of the COM (d_1) for trajectories 1-7.*

Increasing d_3 (assuming negligible increase in total chassis length) shifts weight back onto the drive wheels, effectively shortening the relative length of d_1. This explains the reduction of splay force with an increase of d_3 (Figure 6.25), because the magnitudes of caster reaction forces decrease with the reductions of caster load. So, increasing d_3 is beneficial to decreasing stress and deflection in the chassis. The relationship is non-linear, which is due to the normal forces being raised to the power of 1.5 to account for the change in contact patch radius.

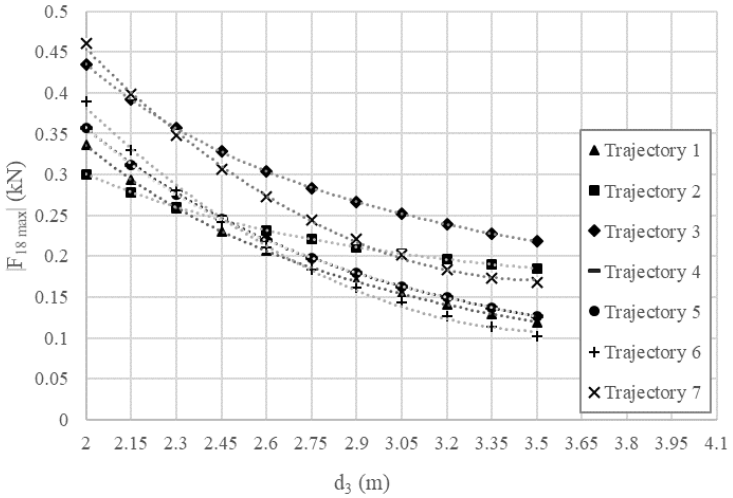

Figure 6.25: *Peak splay force on chassis vs wheel base (d_3) for trajectories 1-7.*

Longer caster trails reduce the peak splay force (Figure 6.26). This is no surprise as $F_{11,12}$ is directly influenced by caster trail. Larger splay forces are observed for trajectories 6 and 7 due to larger values of θ_9 and θ_{10}. Therefore, caster trails should be kept larger.

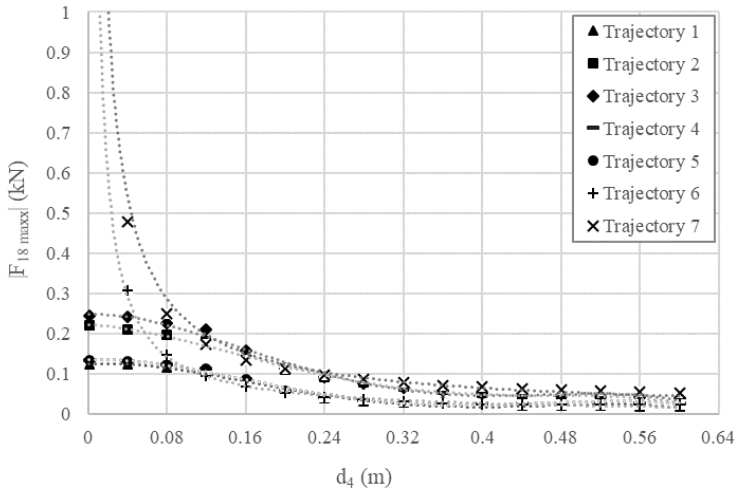

Figure 6.26: *Peak splay force on chassis vs caster trail (d_4) for trajectories 1-7.*

The influence of L_1 on peak splay/compression force can be seen in Figure 6.27. Increases of L_1 clearly generate larger splay forces on the chassis. Shifting the COM away from the center of the vehicle creates an imbalance between the normal forces of the left and right side of the vehicle. This generates a Large difference between the caster reaction forces, thus making splay forces extremely sensitive to L_1. In reality, L_1 is normally very close to zero, but it still should not be ignored during design of over-arch DDMRs i.e. it would be a poor design decision to put all battery packs on one side of vehicle.

Upon inspecting Figure 6.28, quite different influences from L_2 are observed. The differences are not due to larger values of θ_9 and θ_{10} because the sensitivities for trajectories 6 and 7 are very different. Trajectories 2, 3 and 7 show similar large sensitivities. For these trajectories, angular accelerations of the vehicle occur when θ_1 is 0 or 180°. At these orientations gravitational forces from the slope cause a significant imbalance in weight distribution between the two sides of the vehicle (F_7 is large, Figure 6.2). This, coupled with a greater centripetal force due to the angular acceleration, creates a much more significant difference between F_{11} and F_{12} than trajectories 1, 4, 5 and 6. If $2L_2$ is increased, load imbalances due to gravity and centripetal acceleration are reduced, thus

decreasing the difference between F_{11} and F_{12}. Note, in this study L_3 was not increased with $2L_2$, but the normal force model assumes $2L_3 = 2L_2$ (otherwise it would be statically indeterminate). Therefore, the reduction of the normal force imbalance on the casters (from an increase of $2L_2$) will in reality be less than suggested by Figure 6.28. Based on these results, $2L_2$ should be kept large to reduce splay forces.

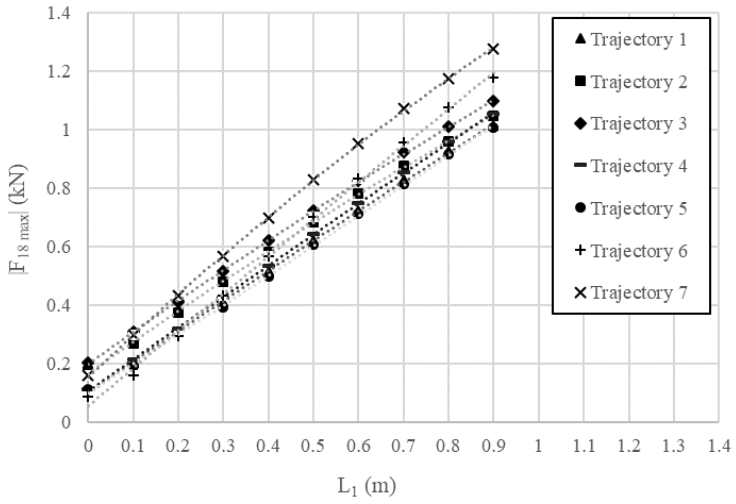

Figure 6.27: *Peak splay force on chassis vs lateral position of the COM (L_1) for trajectories 1-7.*

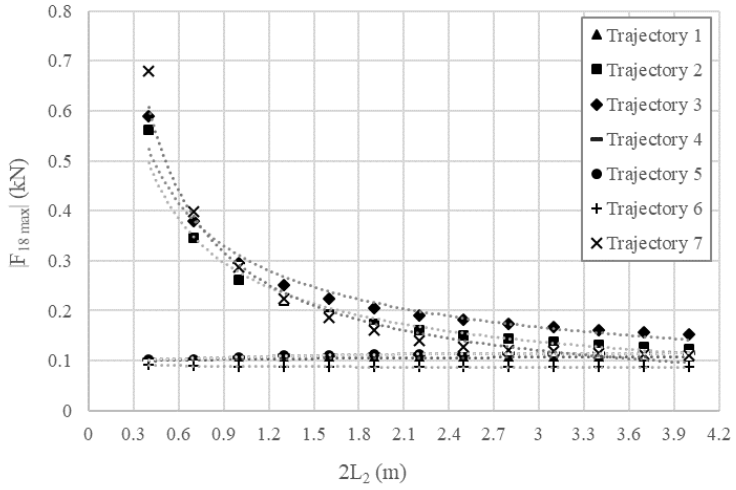

Figure 6.28: *Peak splay force on chassis vs track width ($2L_2$) for trajectories 1-7.*

From greatest to least, the order of dimensions with regard to dimensional sensitivity for peak splay force on trajectory 1 is L_1, d_4, d_1, d_3, and $2L_2$ (Figure 6.29). Sensitivity to $2L_2$ is negligible. Therefore, for a standard trajectory in a level vineyard, L_1 and d_4 should be adjusted first to reduce peak splay forces.

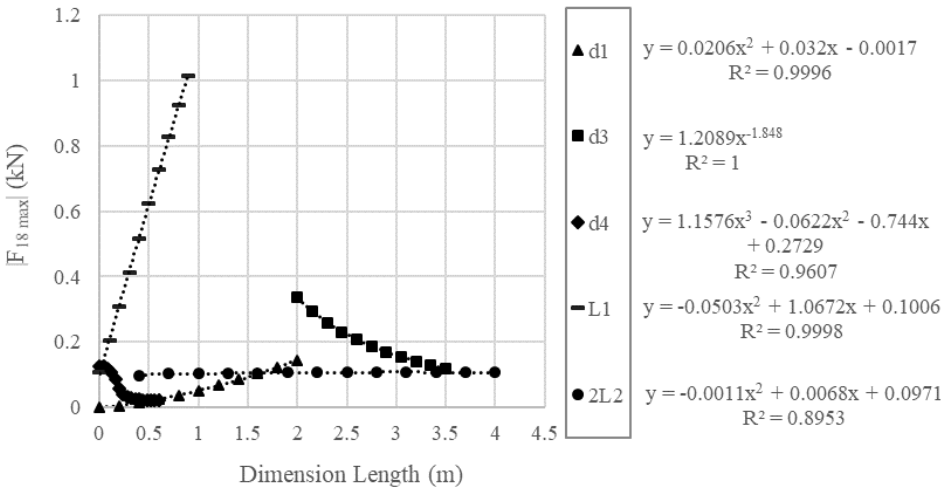

Figure 6.29: *Peak splay force vs dimension length for trajectory 1 for dimensions d_1, d_3, d_4, L_1 and $2L_2$.*

The trajectories on which d_1, d_3, d_4, L_1 and $2L_2$ are most influential are 3, 7, 7, 6, and 7 respectively. Placed highest to lowest, the order of dimensions with regard to dimensional sensitivity for peak splay force across trajectories 2-7 is L_1, d_4, d_1, $2L_2$ and d_3 (Figure 6.30). Increased sensitivity to d_1 is observed, but the most significant difference is the sensitivity to $2L_2$. A slight increase in sensitivity to d_3 is also observed. Therefore, to optimise for all environments tested in this study, L_1 and d_4 should be adjusted first, followed by d_1, $2L_2$, and lastly d_3. Increasing d_4 from 0.13-0.33 m, decreasing d_1 from 1.632 to 1.432 m, and increasing $2L_2$ from 1.882 to 2.082 reduces peak splay forces by 57.4 %, 11.5 %, and 7.79 % respectively. Increasing L_1 from 0 to 0.2 m increases peak splay force by 447 %.

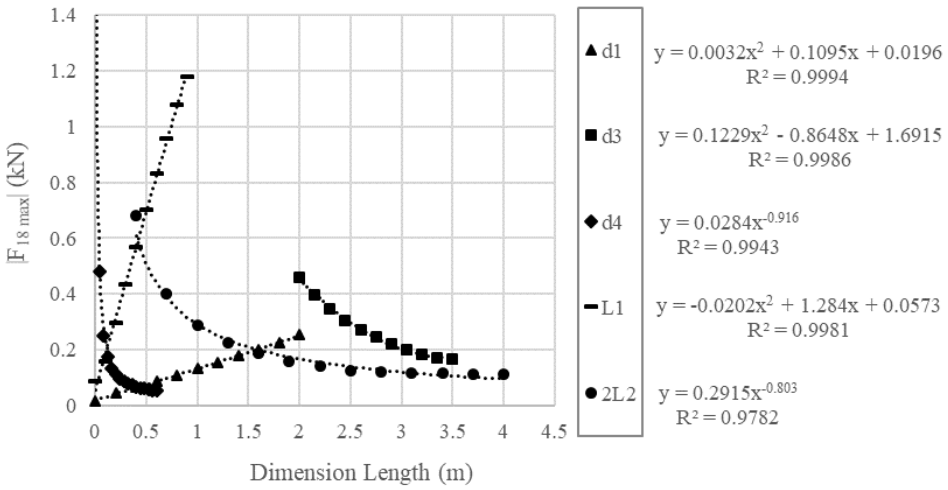

Figure 6.30: *Peak splay force on chassis vs dimension length for each dimension (d_1, d_3, d_4, L_1 and $2L_2$). The plot for each dimension was taken from the trajectory on which the dimension had the highest influence.*

6.1.5 Archie Junior vs Nico Bot

A similar is trend is seen for Archie Junior and Nico Bot regarding the effects of d_1 on peak drive forces (Figure 6.31). Both are non-linear and increasing. Overall, Archie Junior is much more sensitive to this dimension, with peak drive force increasing to 4.4 times the initial (Nico Bot only 2.4 times).

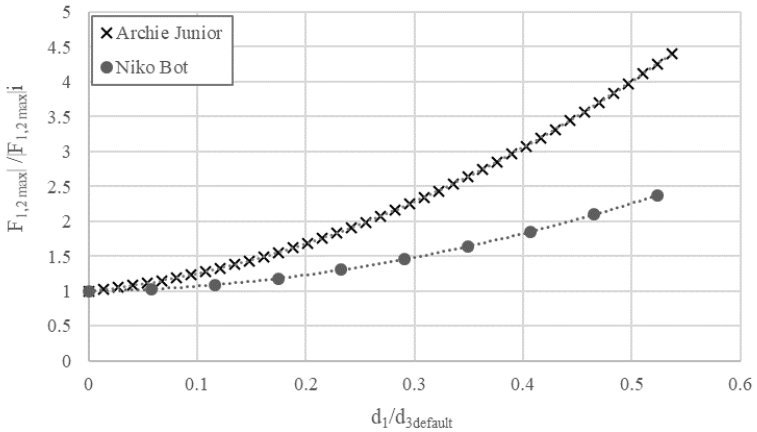

Figure 6.31: $\frac{|F_{1,2max}|}{|F_{1,2max}|_i}$ *vs* $\frac{d_1}{d_{3default}}$ *for Archie Junior and Nico Bot.*

Both trends are also similar for d_3 (Figure 6.32), with Nico Bot showing a slightly higher sensitivity. Archie Junior exhibits a higher sensitivity to d_4 (Figure 6.33), but again, both trends are similar. Sensitivities for L_1 show excellent agreement (Figure 6.34). The Nico Bot shows a higher sensitivity to $2L_2$ than Archie Junior (Figure 6.35), but the trends are similar. These results show that dimensional sensitivities for Archie Junior can be applied as a guideline for smaller vehicles.

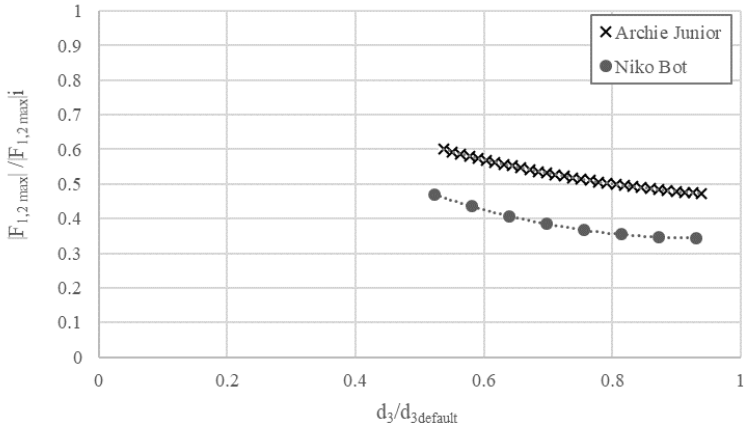

Figure 6.32: $\frac{|F_{1,2max}|}{|F_{1,2max}|_i}$ *vs* $\frac{d_3}{d_{3default}}$ *for Archie Junior and Nico Bot.*

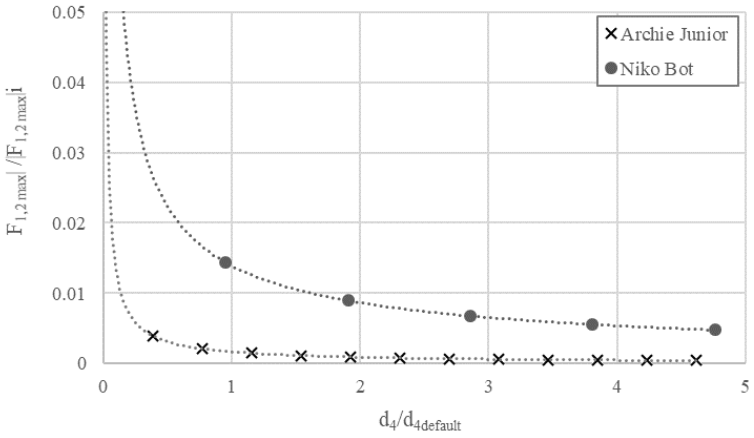

Figure 6.33: $\frac{|F_{1,2max}|}{|F_{1,2max}|_i}$ *vs* $\frac{d_4}{d_{4default}}$ *for Archie Junior and Nico Bot.*

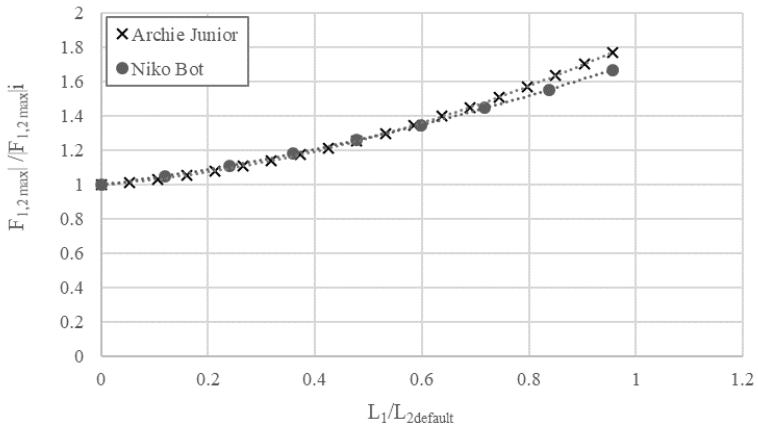

Figure 6.34: $\frac{|F_{1,2max}|}{|F_{1,2max}|_i}$ *vs* $\frac{L_1}{L_{2default}}$ *for Archie Junior and Nico Bot.*

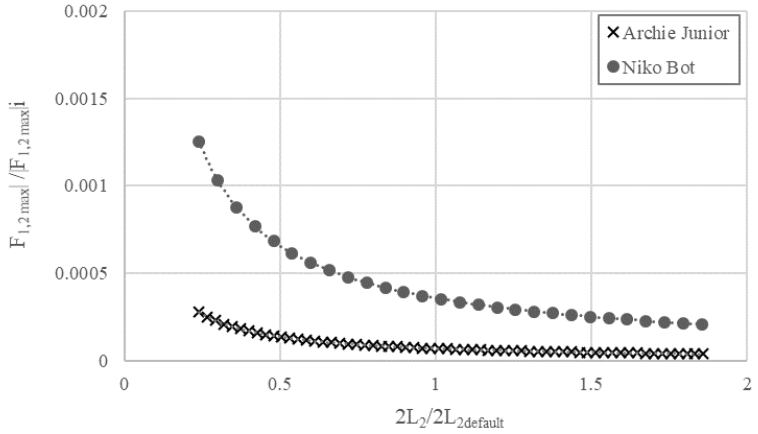

Figure 6.35: $\frac{|F_{1,2max}|}{|F_{1,2max}|_i}$ *vs* $\frac{2L_2}{2L_{2default}}$ *for Archie Junior and Nico Bot.*

6.2 Chassis Loading and Vehicle Instability Study

6.2.1 Vehicle Stability

6.2.1.1 Effect of Caster Trail on Stability

For tests 1 and 2, a minimal initial deviation of x_1 (-0.11 and 0.11 m) is observed at the lowest caster trail but increases quickly to a maximum of approximately -0.6 and 0.6 m at a caster trail of 0.15 m (Figure 6.36). Deviation then gradually reduces to approximately zero at a caster trail of 0.7 m, after which small deviations are observed in

the opposite direction. It was observed that the casters flip around in opposite directions when $d_4 = 0.1$ m. The initial deviation of the vehicle generated by initial caster angles must occur in a way that causes two different directions in caster rotation as the vehicle travels forward. This would account for the small deviation seen at $d_4 = 0.1$ m, because apposing caster rotations generate apposing lateral reaction forces. The change in the direction of deviation at longer caster trails was not expected. At longer caster trails, tire-ground reaction torques have less of an effect compared to rolling resistance (which remains constant), which could be the cause of the shift in direction at longer caster trails. The $\hat{i}$ (lateral) components of the rolling resistances F_{13} and F_{15} are always in the opposite direction of the reaction forces (F_{14} and F_{16}). Therefore, the difference between the effect of tire-ground reaction torques and rolling resistances is the cause.

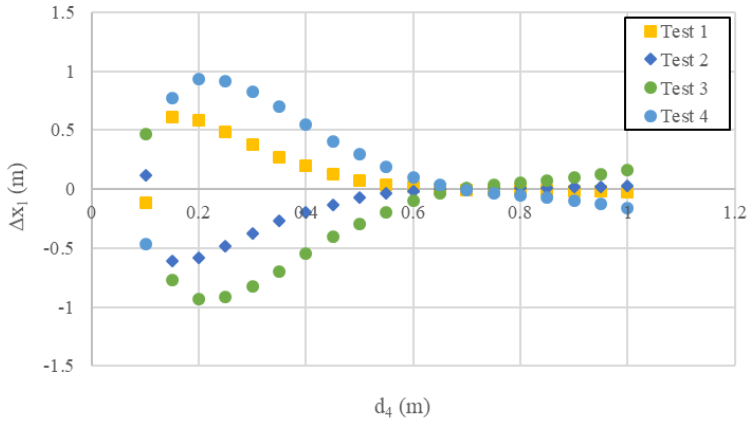

Figure 6.36: *Maximum deviation of x_1 vs caster trail. Test 1, casters leading with $\theta_{5,6i} = 175^\circ$. Test 2, casters leading with $\theta_{5,6i} = 185^\circ$. Test 3, casters trailing with $\theta_{5,6i} = -5^\circ$. Test 4, casters trailing with $\theta_{5,6i} = 5^\circ$.*

The same instability trends are seen for the maximum deviations of vehicle angle (Figure 6.37). Therefore, at first glance, a very small or large caster trail is desirable for stability. However, caster reaction forces increase significantly with very small caster trails, which means a larger caster trail is more desirable. Very large caster trails should be avoided due to excessive moments on the caster king pins. Therefore, a medium caster trail is best for improving stability. Note, caster shimmy has not been considered in this study and should not be forgotten.

For tests 3 and 4, deviation trends for x_1 are θ_1 are very similar but have higher maximum values of deviation. Deviation at $d_4 = 0.1$ is in the opposite direction to $d_4 = 0.15$. This is caused by the different directions of caster rotation at $d_4 = 0.1$. Based on the larger values of deviation, caster stability results suggest that a DDMR driven with casters trailing behind is less stable than one with casters leading. Therefore, to reduce work for the motor controllers, DDMR's should be driven with casters leading, using casters with a medium caster trail.

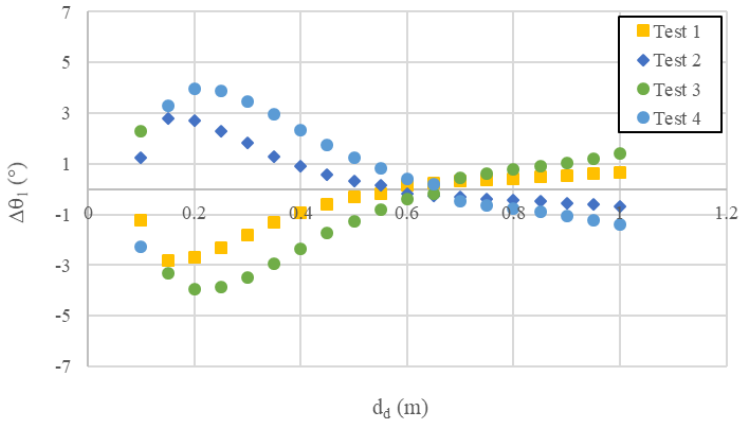

Figure 6.37: *Maximum deviation of θ_1 vs caster trail. Test 1, casters leading with $\theta_{5,6i} = 175^\circ$. Test 2, casters leading with $\theta_{5,6i} = 185^\circ$. Test 3, casters trailing with $\theta_{5,6i} = -5^\circ$. Test 4, casters trailing with $\theta_{5,6i} = 5^\circ$.*

Sample trajectories agree with maximum deviations (Figures 6.38 and 6.39). A medium caster trail (0.5 m) provides the least eccentric deviation, while other values actually change the direction of motion. These eccentric motions will be caused by changes in the directions of F_{11} and F_{12} i.e. if θ_5 and θ_6 are greater than 90 °, F_{11} and F_{12} are positive, and if less than 90 °, F_{11} and F_{12} are negative. As caster trail is increased, the degree to which these changes in force direction have an effect reduces, because the magnitudes of F_{11} and F_{12} reduce.

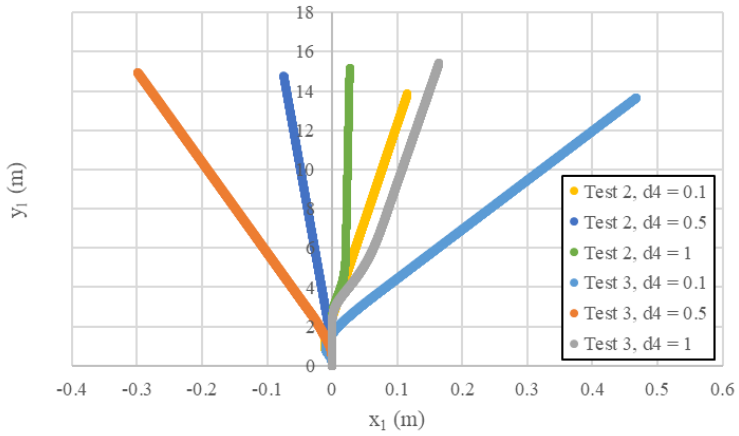

Figure 6.38: *Sample trajectories from tests 2 and 3. Test 2, casters leading with* $\theta_{5,6i} = 185\,^{\circ}$. *Test 3, casters trailing with* $\theta_{5,6i} = -5\,^{\circ}$.

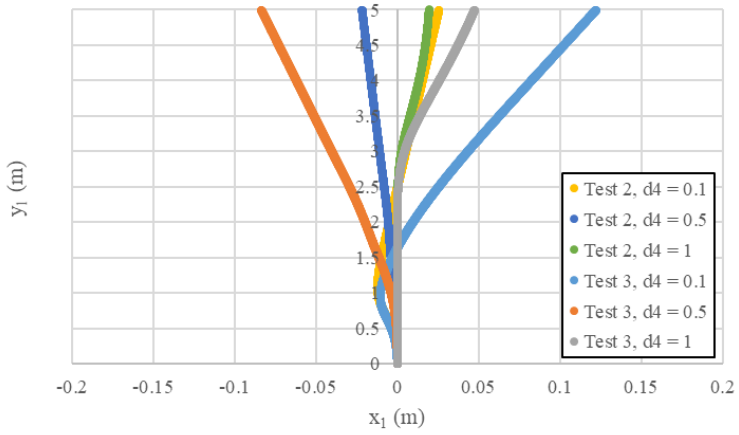

Figure 6.39: *Sample trajectories from tests 2 and 3 enlarged.*

6.2.1.2 Stability and the Lateral Position of the Center of Mass

Maximum deviation of x_1 and θ_1 increase as L_1 is increased (Figures 6.40 and 6.41). Quite large deviations are observed, with $\Delta\theta_1$ as high as 90 ° and Δx_1 as much as 4 m. Tests 3 and 4 show the largest maximum deviations, suggesting that to improve vehicle stability, the vehicle should not be driven forwards with the COM trailing. Sample trajectories agree with maximum deviations (Figure 6.42). They are also less eccentric than instability caused by casters.

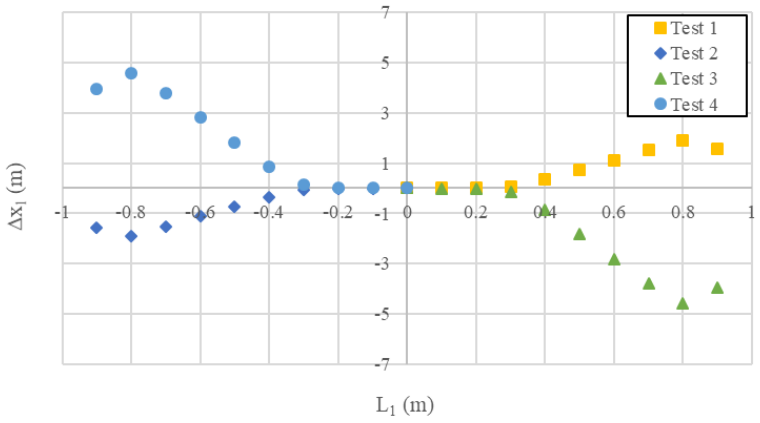

Figure 6.40: *Maximum deviation of x_1 vs lateral position of COM. Test 1, positive L_1, COM leading. Test 2, negative L_1, COM leading. Test 3, negative L_1, COM trailing. Test 4, positive L_1, COM trailing.*

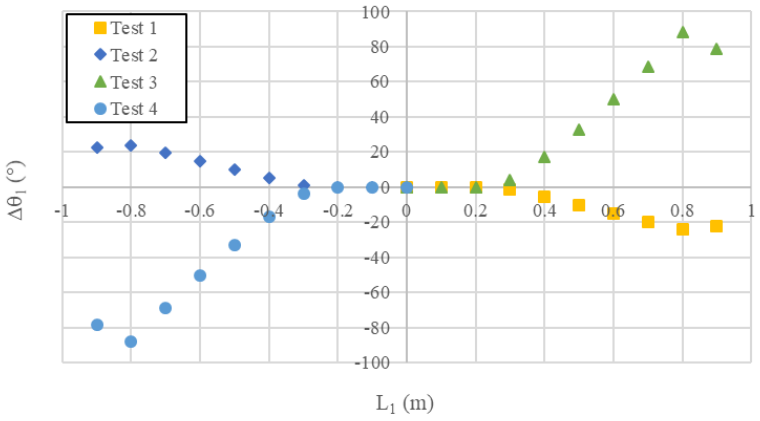

Figure 6.41: *Maximum deviation of θ_1 vs lateral position of COM. Test 1, positive L_1, COM leading. Test 2, negative L_1, COM leading. Test 3, negative L_1, COM trailing. Test 4, positive L_1, COM trailing.*

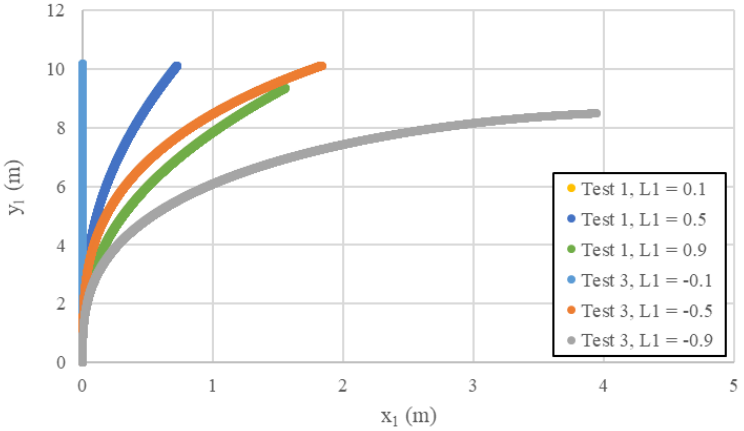

Figure 6.42: *Sample trajectories from tests 1 (COM leading) and 3 (COM trailing).*

6.2.2 Vehicle Stability Summary

Appropriate motor control would help to remove instabilities caused by caster trail and center of mass position, provided enough traction exists etc. However, results in this study show that the amount (and complexity) of stability control required can be reduced through vehicle design.

6.2.3 Worst Case Chassis Splay and Compression Force

As could be expected, worst case splay forces decrease with longer caster trails (Figure 6.43). However, reduction of splay force becomes insignificant for caster trails larger than approximately 0.12 m. Positive and negative values of splay force show very similar magnitudes, and the directions the caster flip (both outward or both inward) has negligible affect. Therefore, caster trail should be kept on the larger side to reduce maximum splay forces.

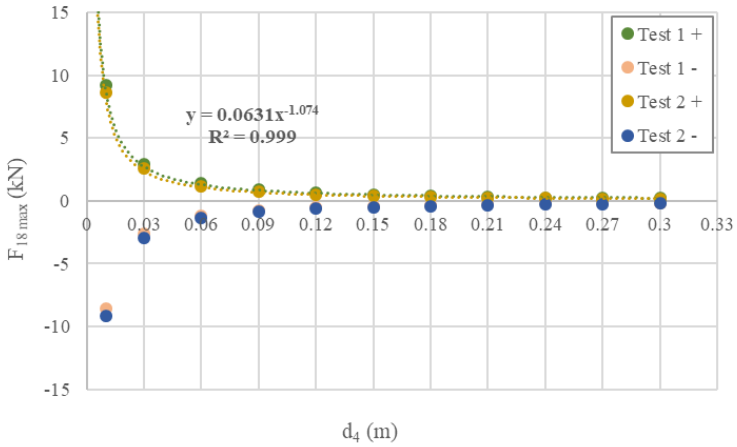

Figure 6.43: *Splay/compression force applied to chassis from casters vs caster trail. Test 1 +, maximum positive force for casters turned in. Test 1 -, maximum negative force for casters turned in. Test 2 +, maximum positive force for casters turned out. Test 2 -, maximum negative force for casters turned out.*

6.3 Chassis Inertia Study

Peak drive forces are less sensitive to $2L_2$ if the chassis width is also increased with $2L_2$ (Figure 6.44). Therefore, if $2L_2$ is to be used to reduce drive forces required during turning maneuvers, an over-arch chassis should be kept at the same width if possible i.e. the drive wheels should be extended outward from the chassis when increasing track width.

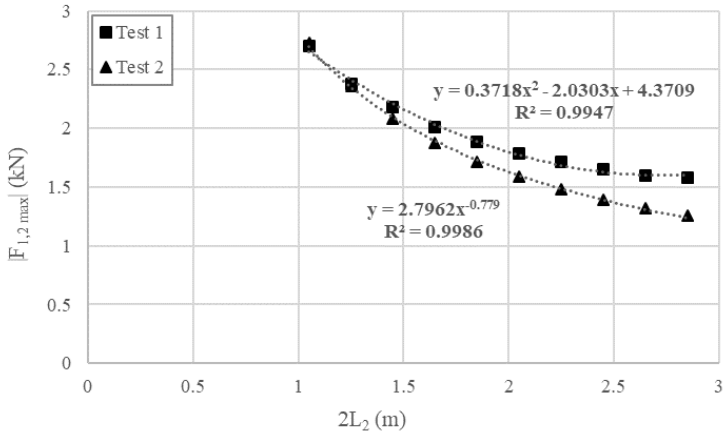

Figure 6.44: *Peak drive force vs track width with constant and varying chassis width. Test 1, varying chassis width. Test 2, constant chassis width.*

6.4 Archie Junior Case Study

For Archie Junior with default dimensions driving on trajectory 6, the drive forces for the left and right wheels both exceeded traction force (F_{tr}) and nominal motor force ($F_{m,nominal}$) during the acceleration phase. This means the vehicle lost traction during acceleration. However, drive forces were well below maximum available motor drive forces ($F_{m,max}$), and steady state drive forces are significantly below nominal motor forces. Caster trail (d_4) was lengthened to 0.25 m, but it was found that the vehicle still lost traction. So, the longitudinal position of the COM (d_1) was shortened to 1.2 m. With the adjusted dimensions the vehicle no longer lost traction (Figures 6.45 and 6.46). Therefore, the vehicle is now able to operate on any trajectory with zero slope and poor ground conditions, provided the required acceleration is not increased.

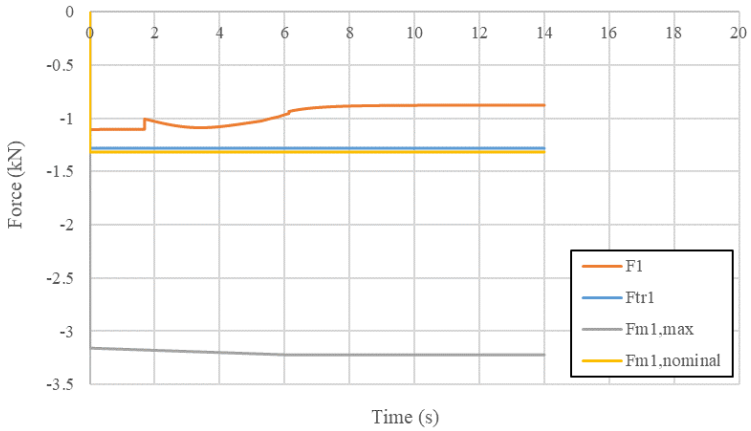

Figure 6.45: *Drive force (F_1), traction force (F_{tr1}), max motor drive force ($F_{m1,max}$) and nominal motor drive force ($F_{m1,nominal}$) vs time for left drive wheel, Trajectory 6, $d_4 = 0.25$ and $d_1 = 1.2$.*

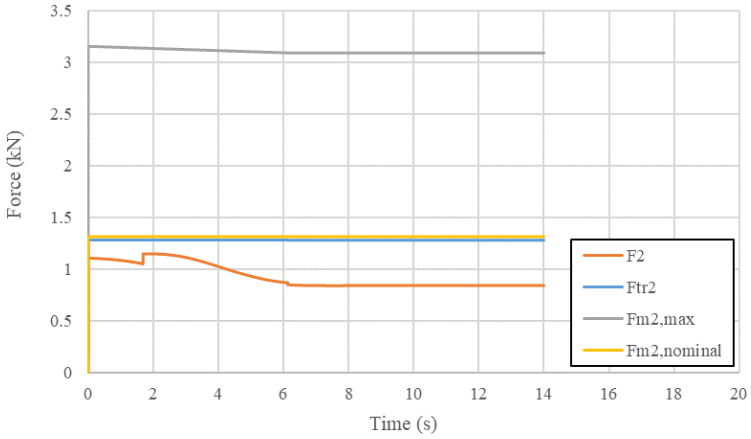

Figure 6.46: *Drive force (F_2), traction force (F_{tr2}), max motor drive force ($F_{m2,max}$) and nominal motor drive force ($F_{m2,nominal}$) vs time for right drive wheel, Trajectory 6, $d_4 = 0.25$ and $d_1 = 1.2$.*

Next, the vehicle was tested on trajectory 7 (5 ° of slope). The vehicle lost traction again. d_1 was reduced further to 0.8 m (as much as is practically feasible) and the vehicle no longer lost traction. However, the margin was extremely small, so the track width ($2L_2$) was increased to 2.4 m. The margin was still quite small for the left drive wheel. d_3 was increased to 4 m and d_4 to 0.3 m, but this had little affect. So, track width was increased further to 2.6 m, which is not ideal because this makes the vehicle quite wide. Final force profiles can be seen in Figures 6.47 and 6.48. The vehicle does not loose traction and stays below nominal motor torque for the entire maneuver. Therefore, the vehicle has

been optimised to operate in typical vineyard environments (including slopes). Note, a large portion of the vehicles weight now sits on the drive wheels (Figure 6.49), meaning that d_1 should not be reduced any further, otherwise the vehicle may tip over backwards. If interested, all plots not shown here can be found in Appendix C.

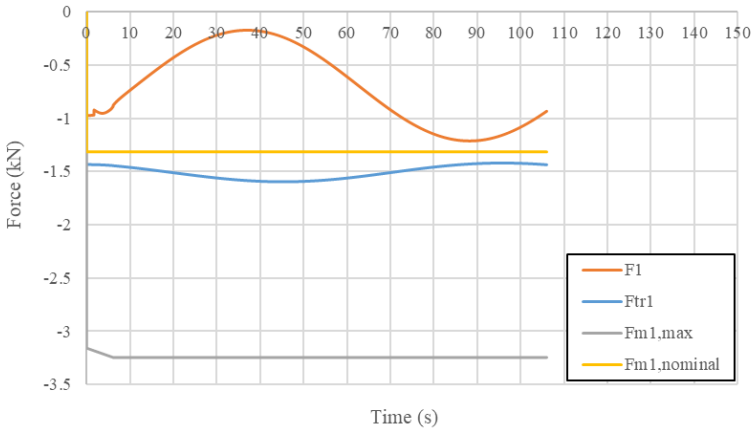

Figure 6.47: *Drive force (F_1), traction force (F_{tr1}), max motor drive force ($F_{m1,max}$) and nominal motor drive force ($F_{m1,nominal}$) vs time for Left drive wheel, Trajectory 7, $d_4 = 0.3$ and $d_1 = 0.8$, $2L_2 = 2.6$, $d_3 = 4$.*

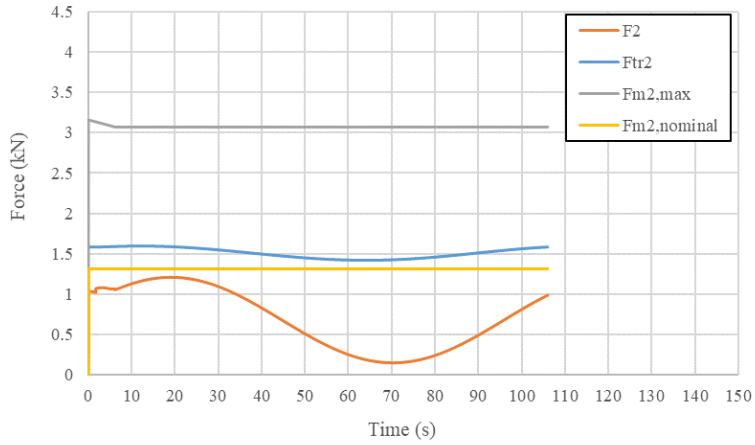

Figure 6.48: *Drive force (F_2), traction force (F_{tr2}), max motor drive force ($F_{m2,max}$) and nominal motor drive force ($F_{m2,nominal}$) vs time for right drive wheel, Trajectory 7, $d_4 = 0.3$ and $d_1 = 0.8$, $2L_2 = 2.6$, $d_3 = 4$.*

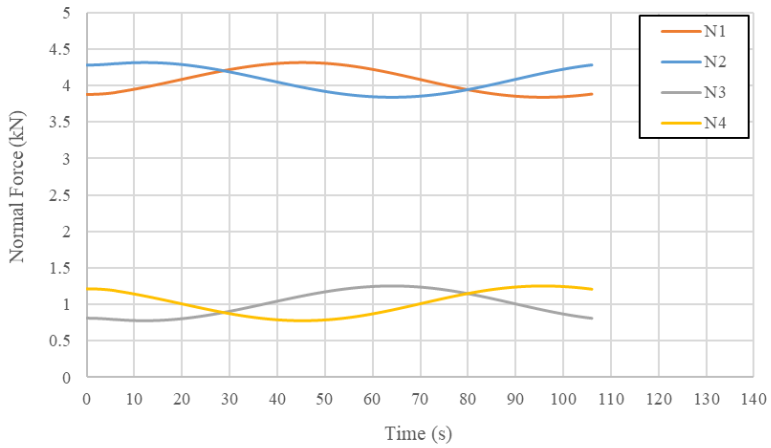

Figure 6.49: *Normal forces on vehicle wheels vs time for trajectory 7,* $d_4 = 0.3$ *and* $d_1 = 0.8$*,* $2L_2 = 2.6$*,* $d_3 = 4$*.* N_1 *= back left drive wheel,* N_2 *= back right drive wheel,* N_3 *= front left caster, and* N_4 *= front right caster.*

It should be noted that the actual physical vehicle performed better during actual testing than the model with the default dimensions. Traction for the actual vehicle was not an issue. However, the ground upon which the vehicle was tested was not worst case scenario, and it likely had a much larger coefficient of friction than 0.37. Despite this, the initial traction for the model is so low that it is likely the model is not a precise reflection of Archie Junior. Estimates for actual mass and rotational inertia could be inadequate as they were taken from the CAD model, not from the actual vehicle.

This case study has shown than dimensional optimisation very useful, and that dimensions should be adjusted to improve performance provided they remain within the functional requirements.

6.5 Analysis Summary

For easy comparison, the dimensional sensitivities of peak drive force, energy consumption, peak shear force, and peak splay force are presented in tables 6.1 and 6.2 . All dimensions were shifted 0.2 m from their default values, with the exception of wheel base (d_3), which has a default value of 3.727 m (as opposed to 3.5 m). It is clear that the performance of over-arch DDMRs are significantly sensitive to dimensions. Overall, caster trail (d_4) has

the most influence and wheel base the least. If the track width is to be widened to reduce required drive forces, chassis width should be kept constant if possible. It was also found that caster trail and the COM position do have an effect on inherent vehicle stability. Finally, dimensional optimisation has been successfully illustrated via a vehicle case study.

Table 6.1: Sensitivities for a dimensional change of ±0.2 m on trajectory 1 for peak drive force ($|F_{1,2max}|$), total energy consumed (E_{total}), peak shear force ($|F_{17max}|$), and peak splay force ($|F_{18max}|$).

Dimension Changed	$\Delta\|F_{1,2max}\|$ (%)	ΔE_{total} (%)	$\Delta\|F_{17max}\|$ (%)	$\Delta\|F_{18max}\|$ (%)
d_1 (1.632-1.432 m)	13.1	0.664	15.1	18.1
d_3 (3.5-3.3 m)	1.58	1.73	1.15	11.5
d_4 (0.13-0.33 m)	36.6	1.59	42.0	65.0
L_1 (0-0.2 m)	5.71	0.235	6.36	210
$2L_2$ (1.882-2.082 m)	8.73	0.00227	14.1	0.460

Table 6.2: Sensitivities for a dimensional change of ±0.2 m for the trajectories on which each dimension had the most influence on peak drive force ($|F_{1,2max}|$), total energy consumed (E_{total}), peak shear force ($|F_{17max}|$), and peak splay force ($|F_{18max}|$).

Dimension Changed	$\Delta\|F_{1,2max}\|$ (%)	ΔE_{total} (%)	$\Delta\|F_{17max}\|$ (%)	$\Delta\|F_{18max}\|$ (%)
d_1 (1.632-1.432 m)	13.9	0.428	15.0	11.5
d_3 (3.5-3.3 m)	1.79	2.73	1.68	3.42
d_4 (0.13-0.33 m)	56.4	1.50	58.0	57.4
L_1 (0-0.2 m)	8.08	0.236	11.3	447
$2L_2$ (1.882-2.082 m)	9.37	2.44	10.0	7.79

Chapter 7

Conclusion

Literature was reviewed regarding over-arch differential drive vehicle dynamics, and a gap was found pertaining to physical optimisation via vehicle dimensions. Therefore, a dynamic model of a large scale agricultural over-arch differential drive mobile vehicle was constructed and the dimensional sensitivity of peak drive/brake force, energy consumption, chassis shear force and lateral chassis splay/compression force was assessed. The effects of caster trail and the lateral position of the COM on stability were also assessed.

7.1 Dimensional Sensitivity of Drive Forces

For all probable trajectory types (including trajectories on slopes up to 5 °), peak drive/brake force is most sensitive to caster trail, followed by the longitudinal position of the COM and then the track with. The lateral position of the COM is the next least influential followed by the wheel base. Increasing by caster trail by 0.2 m, decreasing the longitudinal position of the COM by 0.2 m, and increasing track width by 0.2 m provides a decrease in peak drive force of 56.4 %, 13.9 % and 9.37 % respectively. These values highlight the fact that the dimensional sensitivity of peak drive/brake force is not trivial. Therefore, dimensional optimisation is very valuable.

It was also found that increasing track width while keeping the width of the chassis the same provides a greater reduction of peak drive/brake force than if the chassis body is widened with the track width. Therefore, extending the track width out past the chassis is the ideal way to reduce drive forces via track width.

7.2 Dimensional Sensitivity of Energy Consumption

Wheel base has the highest influence on energy consumption followed by the track width and then caster trail. The longitudinal position of the COM and lateral position of the COM are the 2nd to least and least influential. Decreasing the wheel base by 0.2 m provides a reduction of 2.73 %. Increasing the track width by 0.2 m gives an increase in energy consumption of 2.44 %. These values are not trivial due to the typically large duty cycle of agricultural vehicles. Therefore, optimisation of energy consumption via vehicle dimensions should not be ignored.

7.3 Dimensional Sensitivity of Chassis Loading

Peak chassis shear force is most sensitive to caster trail and then the longitudinal position of the COM. The lateral position of the COM has the next least effect on peak shear force, followed by track width and then wheel base. Increasing caster trail by 0.2 m and decreasing longitudinal position of the COM by 0.2 m provides a decrease in peak drive force of 58.0 % and 15.0 % respectively. Increasing the lateral position of the COM generates an increase of 11.3 %. These values are not insignificant, particularly the influence of caster trail. Therefore, dimensions should not be ignored during chassis design.

Peak splay/compression force is most influenced by the lateral position of the COM, followed by caster trail. The longitudinal position of the COM is the 3rd least influential, followed by track width and then wheel base. Increasing caster trail by 0.2 m, decreasing

longitudinal position of the COM by 0.2 m, and increasing track width by 0.2 m reduces peak splay force by 57.4 %, 11.5 %, and 7.79 % respectively. Increasing the lateral position of the COM by 0.2 m increases peak splay force by 447 %. Maximum splay/compression force occurs during vehicle motions that cause both casters to flip inwards towards the center of the chassis or outwards away from the chassis i.e when the casters flip in opposite directions. These findings show that dimensional optimisation should not be neglected during optimisation of an over-arch chassis.

7.4 Dimensional Sensitivity of Large Vehicles vs Small Vehicles.

Dimensional sensitivities for peak drive/brake force were also assessed for a model of a small scale vehicle (vehicle mass of 86 kg) and the results show similar trends to the main large scale test vehicle (vehicle mass of 1042 kg). Overall, the larger vehicle is more sensitive to dimensions, with a change in the longitudinal position of the COM increasing peak drive forces by nearly twice as much the smaller vehicle. These results show that dimensional sensitivities from this study can be applied as a guide for smaller vehicles.

7.5 Vehicle Stability

Inherent vehicle stability is indeed affected by caster trail and the lateral position of the COM. Large or very small caster trails provide the most stability. The lateral position of the COM should be kept directly on the longitudinal axis of the vehicle and the vehicle should be driven with the casters and COM leading if maximum stability is desired. Therefore, to increase stability, caster trail the COM position should not be neglected.

7.6 Concluding Remarks

A case study was conducted on a Simulink model of a DDMR designed for operating in vineyards. Dimensional optimisation was successfully performed such that the vehicle was able to operate adequately in the simulated vineyard environment. The case study illustrates that dimensional sensitivity is useful for the optimisation of a vehicle for its intended working environment.

This study has shown that optimisation of over-arch DDMR dimensions is worthwhile, because peak drive force, energy consumption, stability, and chassis loading are significantly affected by vehicle dimensions. Reducing peak drive force and chassis loading cuts down component and material costs. The improvements seen in stability will make control and path tracking easier. Caster trail is most influential dimension overall, and wheel base is the least. Findings from this study add to the study of over-arch DDMRs, broadening this area of research. They aid the building of cheaper, more efficient, and more environmentally friendly over-arch differential drive vehicles. This progresses the process of increasing food production and filling the labour gap, thus giving the world a better chance of obtaining zero hunger by 2030.

7.7 Future Work

Now that the dimensional sensitivity of over-arch differential drive dynamics has been determined, it would be useful to ascertain the dimensional sensitivity of other agricultural vehicles that use steering systems such Ackermann steering, skid steering, and 4 wheel drive Ackermann, so that they also can be more easily optimised. Also, by adjusting the dynamic model in this study such that it can be changed from a DDMR to these other steering systems, the performance of the different steering systems could be compared, thus allowing the best vehicle type for the job to be selected.

It has been shown that dimensions have an effect on inerrant vehicle stability. The exact degree to which this instability affects the control of these vehicles should be assessed.

Chassis loading has been shown to be affected by vehicle dimensions. However, the results have not been compared to real world data, which would be a useful because it would aid the assessment of model accuracy.

Finally, the model in this study was compared to an actual differential drive mobile robot, but the experiment was unsuccessful for various reasons. This was unfortunate because full vehicle validation would further confirm results in this study. This could be done by building a test vehicle specifically designed with validation in mind.

References

[1] Stats NZ. Which industries contributed to new zealand's gdp? `https://www.stats.govt.nz/tools/which-industries-contributed-to-new-zealands-gdp`, November 2020.

[2] Adlerteg Casper and Sen Adem. Navigation with variable point of reference for 3dof differential drive mobile robot, 2021.

[3] JJ Kauzlarich, T Bruning, and JG Thacker. Wheelchair caster shimmy and turning resistance. *Journal of rehabilitation research and development*, 21(2):15–29, 1984.

[4] Dan Ding, Rory A Cooper, Songfeng Guo, and Thomas A Corfman. Analysis of driving backward in an electric-powered wheelchair. *IEEE transactions on control systems technology*, 12(6):934–943, 2004.

[5] Renato Vidoni, Marco Bietresato, Alessandro Gasparetto, and Fabrizio Mazzetto. Evaluation and stability comparison of different vehicle configurations for robotic agricultural operations on side-slopes. *Biosystems engineering*, 129:197–211, 2015.

[6] United Nations. Population. `https://www.un.org/en/global-issues/population`, July 2022.

[7] Mission. https://www.wfp.org/overview.

[8] Ministry of Business Innovation & Employment. iRSLG handover report: Otago 2021 - Key labour market highlights. Technical report, Ministry of Business, Innovation & Employment, 2021.

[9] Ministry of Business Innovation & Employment. Handover document: Hawke's Bay region. Technical report, Ministry of Business, Innovation & Employment, May 2021.

[10] Ministry of Business Innovation & Employment. Marlborough Local Insights Report: February 2022. Technical report, Ministry of Business, Innovation & Employment, February 2022.

[11] Ministry of Business Innovation & Employment. Handover document: Taranaki region. Technical report, Ministry of Business, Innovation & Employment, May 2021.

[12] Ministry of Business Innovation & Employment. Waikato interim Regional Skills Leadership Group: Summary report. Technical report, Ministry of Business, Innovation & Employment, August 2021.

[13] Mohd Saiful Azimi Mahmud, Mohamad Shukri Zainal Abidin, Abioye Abiodun Emmanuel, and Hameedah Sahib Hasan. Robotics and automation in agriculture: present and future applications. *Applications of Modelling and Simulation*, 4:130–140, 2020.

[14] John deere reveals fully autonomous tractor at ces 2022. https://www.deere.com/en/news/all-news/autonomous-tractor-reveal/.

[15] The Editors of Encyclopaedia. tractor | Definition, History, Types, Examples, & Facts | Britannica, December 2021.

[16] SR Verma. Impact of agricultural mechanization on production, productivity, cropping intensity income generation and employment of labourstatsnz. *Status of farm mechanization in India*, 2006:133–153, 2006.

[17] Making sustainable farming economically superior. https://www.monarchtractor.com/.

[18] John Deere. Skid Steers | John Deere US. `https://www.deere.com/en/loaders/skid-steers/`, April 2022.

[19] naio Technologies. Ted, the versatile vineyard weeding robot. https://www.naio-technologies.com/en/news/ted-the-versatile-vineyard-weeding-robot/, July 2022.

[20] Owen Bawden, David Ball, Jason Kulk, Tristan Perez, and Raymond Russell. A lightweight, modular robotic vehicle for the sustainable intensification of agriculture. In *Proceedings of the 16th Australasian Conference on Robotics and Automation 2014*, pages 1–9. Australian Robotics and Automation Association (ARAA), 2014.

[21] Sergio Cubero, Ester Marco-Noales, Nuria Aleixos, Silvia Barbé, and Jose Blasco. Robhortic: A field robot to detect pests and diseases in horticultural crops by proximal sensing. *Agriculture*, 10(7):276, 2020.

[22] Mohammed AH Ali, Wan Azhar BW Yusoff, Zamzuri B Hamedon, Zulkifli BM Yussof, and Musa Mailah. Mechatronic design and development of an autonomous mobile robotics system for road marks painting. In *2016 IEEE Industrial Electronics and Applications Conference (IEACon)*, pages 336–341. IEEE, 2016.

[23] Anh Son Tran and Ha Quang Thinh Ngo. Research and manufacture of automated guided vehicle for the service of storehouse. *Science & Technology Development Journal-Engineering and Technology*, 1(1):5–12, 2018.

[24] Jarrod M Snider, Amy E Snider, and Robert N Riggins. Vasilius: The design of an autonomous ground robotic vehicle. *Journal of Robotic Systems*, 21(9):481–492, 2004.

[25] Lisa Wasko DeVetter, Wei Qiang Yang, Fumiomi Takeda, Scott Korthuis, and Changying Li. Modified over-the-row machine harvesters to improve northern highbush blueberry fresh fruit quality. *Agriculture*, 9(1):13, 2019.

[26] William S Barbosa, Adalberto IS Oliveira, Gustavo BP Barbosa, Antonio C Leite, Karla T Figueiredo, Marley MBR Vellasco, and Wouter Caarls. Design and development of an autonomous mobile robot for inspection of soy and cotton crops. In *2019 12th International Conference on Developments in eSystems Engineering (DeSE)*, pages 557–562. IEEE, 2019.

[27] James Underwood, Alexander Wendel, Brooke Schofield, Larn McMurray, and Rohan Kimber. Efficient in-field plant phenomics for row-crops with an autonomous ground vehicle. *Journal of field robotics*, 34(6):1061–1083, 2017.

[28] DL Peterson, SS Miller, and JD Whitney. Harvesting semidwarf freestanding apple trees with an over-the-row mechanical harvester. *Journal of the American Society for Horticultural Science*, 119(6):1114–1120, 1994.

[29] Peter Biber, Ulrich Weiss, Michael Dorna, and Amos Albert. Navigation system of the autonomous agricultural robot bonirob. In *Workshop on Agricultural Robotics: Enabling Safe, Efficient, and Affordable Robots for Food Production (Collocated with IROS 2012), Vilamoura, Portugal*, 2012.

[30] AF Guo, J Li, LQ Guo, T Jiang, and YP Zhao. Structural design and analysis of an automatic pineapple picking and collecting straddle machine. In *Journal of Physics: Conference Series*, volume 1777, page 012029. IOP Publishing, 2021.

[31] Qian Wang, Zhi Peng Li, and Dao Qiang Wang. Structural design and analysis on frame of blueberry harvesters based on ansys. In *Applied Mechanics and Materials*, volume 26, pages 794–799. Trans Tech Publ, 2010.

[32] Yanmar Holdings Co. Ltd. Yanmar debuts autonomous vineyard robot. `https://www.oemoffhighway.com/electronics/smart-systems/automated-systems/press-release/21772365/yanmar-holdings-co-ltd-yanmar-debuts-autonomous-vineyard-robot`, July 2022.

[33] K Thanjavur and R Rajagopalan. Ease of dynamic modelling of wheeled mobile robots (wmrs) using kane's approach. In *Proceedings of International Conference on Robotics and Automation*, volume 4, pages 2926–2931. IEEE, 1997.

[34] Rached Dhaouadi and A Abu Hatab. Dynamic modelling of differential-drive mobile robots using lagrange and newton-euler methodologies: A unified framework. *Advances in Robotics & Automation*, 2(2):1–7, 2013.

[35] William M Silver. On the equivalence of lagrangian and newton-euler dynamics for manipulators. *The International Journal of Robotics Research*, 1(2):60–70, 1982.

[36] Douglas Cline. 6.13: The Lagrangian versus the Newtonian approach to classical mechanics. `https://phys.libretexts.org/Bookshelves/Classical_Mechanics/Variational_Principles_in_Classical_Mechanics_(Cline)/063A_Lagrangian_Dynamics/6.133A_The_Lagrangian_versus_the_Newtonian_approach_to_classical_mechanics`, November 2020.

[37] A Gentile, A Messina, and A Trentadue. Dynamic behaviour of a mobile robot vehicle with a two caster and two driving wheel configuration. *Vehicle System Dynamics*, 25(2):89–112, 1996.

[38] Barry W Johnson and James H Aylor. Dynamic modeling of an electric wheelchair. *IEEE Transactions on Industry Applications*, IA-21(5):1284–1293, 1985.

[39] S Konduri, T Edison Cobos, and P Pagilla. Study of wheel slip and traction forces in differential drive robots and slip avoidance control strategy. *ASME J. Dynamics, Measurement and Control*, 139:1–6, 2017.

[40] Chris C Ward and Karl Iagnemma. A dynamic-model-based wheel slip detector for mobile robots on outdoor terrain. *IEEE Transactions on Robotics*, 24(4):821–831, 2008.

[41] Po-Chih Chen and Han-pang Huang. 3d dynamical analysis for a caster wheeled mobile robot moving on the frictional surface. In *2006 IEEE/RSJ International Conference on Intelligent Robots and Systems*, pages 3056–3061. IEEE, 2006.

[42] Stevine O Onyango, Yskandar Hamam, Karim Djouani, and Boubaker Daachi. Modeling a powered wheelchair with slipping and gravitational disturbances on inclined and non-inclined surfaces. *Simulation*, 92(4):337–355, 2016.

[43] L Huang. Speed control of differentially driven wheeled mobile robots—model-based adaptive approach. *Journal of Robotic Systems*, 22(6):323–332, 2005.

[44] Habib Choukri Lamraoui, Zhu Qidan, and Abdeldjabar Benrabah. Dynamic velocity tracking control of differential-drive mobile robot based on ladrc. In *2017 IEEE International Conference on Real-time Computing and Robotics (RCAR)*, pages 633–638. IEEE, 2017.

[45] Khansa Bdirina, Ramdane Hedjar, Mohamed Seghir Boucherit, and Hilal Naimi. Predictive control for trajectory tracking of an electrical wheelchair. In *2015 4th International Conference on Systems and Control (ICSC)*, pages 237–242. IEEE, 2015.

[46] Aline Baudry, Sylvain Guegan, and Marie Babel. Taking caster wheel behavior into account in the kinematics of powered wheelchairs. *Modelling, measurement and control C*, 79(4):168–172, 2018.

[47] Félix Chénier, Pascal Bigras, and Rachid Aissaoui. An orientation estimator for the wheelchair's caster wheels. *IEEE Transactions on Control Systems Technology*, 19(6):1317–1326, 2010.

[48] Jitendra Singh and Prashant Singh Chouhan. A new approach for line following robot using radius of path curvature and differential drive kinematics. In *2017 6th International Conference on Computer Applications In Electrical Engineering-Recent Advances (CERA)*, pages 497–502. IEEE, 2017.

[49] Mohd Saifizi Saidonr, Hazry Desa, and Md Noor Rudzuan. A differential steering control with proportional controller for an autonomous mobile robot. In *2011 IEEE 7th International Colloquium on Signal Processing and its Applications*, pages 90–94. IEEE, 2011.

[50] Kinam Lee, Dae-Yeong Im, Bongwoo Kwak, Young-Jae Ryoo, et al. Design of fuzzy-pid controller for path tracking of mobile robot with differential drive. *International Journal of Fuzzy Logic and Intelligent Systems*, 18(3):220–228, 2018.

[51] Azaza Awatef and Ben Hamed Mouna. Dynamic modeling and inverse dynamic control of mobile robot. In *2017 International Conference on Green Energy Conversion Systems (GECS)*, pages 1–5. IEEE, 2017.

[52] Longtao Fan, Yuanheng Zhang, and Sen Zhang. Dynamic trajectory tracking control of mobile robot. In *2018 5th International Conference on Information Science and Control Engineering (ICISCE)*, pages 728–732. IEEE, 2018.

[53] Romano M DeSantis. Modeling and path-tracking control of a mobile wheeled robot with a differential drive. *Robotica*, 13(4):401–410, 1995.

[54] Alexandr Štefek, Van Thuan Pham, Vaclav Krivanek, and Khac Lam Pham. Optimization of fuzzy logic controller used for a differential drive wheeled mobile robot. *Applied Sciences*, 11(13):6023, 2021.

[55] CS Shijin and K Udayakumar. Speed control of wheeled mobile robots using pid with dynamic and kinematic modelling. In *2017 International Conference on Innovations in Information, Embedded and Communication Systems (ICIIECS)*, pages 1–7. IEEE, 2017.

[56] Dongdong Xie, Shenquan Wang, and Yuenan Wang. Trajectory tracking control of differential drive mobile robot based on improved kinematics controller algorithm. In *2018 Chinese Automation Congress (CAC)*, pages 2675–2680. IEEE, 2018.

[57] C.E. Thomas. Fuel cell and battery electric vehicles compared. *International Journal of Hydrogen Energy*, 34(15):6005–6020, August 2009.

[58] Stephen Sprigle and Morris Huang. Impact of mass and weight distribution on manual wheelchair propulsion torque. *Assistive Technology*, 27(4):226–235, 2015. PMID: 26691562.

[59] Andi Adriansyah, Badaruddin Sulle, Eko Ihsanto, and Yudhi Gunardi. Optimization of circular robot size using behavior based architecture. *Journal of Telecommunication, Electronic and Computer Engineering (JTEC)*, 9(3-7):67–72, 2017.

[60] Kaustav Mondal, Brent Wallace, and Armando A Rodriguez. Stability versus maneuverability of non-holonomic differential drive mobile robot: Focus on aggressive position control applications. In *2020 IEEE Conference on Control Technology and Applications (CCTA)*, pages 388–395. IEEE, 2020.

[61] D Elayaraja et al. Design parametric optimization of wall following robot. *Turkish Journal of Computer and Mathematics Education (TURCOMAT)*, 12(8):2072–2080, 2021.

[62] Anahita Habibian, Yalda Aslani Darandashi, Rasul Fesharakifard, Abdolreza Ohadi, and Hamed Ghafarirad. Structural and dynamic analysis of a wheeled mobile robot with different wheel configurations. In *2017 5th RSI International Conference on Robotics and Mechatronics (ICRoM)*, pages 527–533. IEEE, 2017.

[63] R Rajagopalan and N Barakat. Velocity control of wheeled mobile robots using computed torque control and its performance for a differentially driven robot. *Journal of Robotic Systems*, 14(4):325–340, 1997.

[64] Brian B Abraham, Robert I Davidson, and Garth R Johnson. Theory and validation of the motion resistance mechanism of four-caster manual vehicles. *Proceedings of the Institution of Mechanical Engineers, Part K: Journal of multi-body dynamics*, 227(3):313–326, 2013.

[65] Wieslaw M Szydlowski and Srinivas Sastry. Computer simulation of dynamical behavior of self-propelled gurney. In *International Design Engineering Technical Conferences and Computers and Information in Engineering Conference*, volume 11740, pages 89–99. American Society of Mechanical Engineers, 1993.

[66] TG Frank and EW Abel. Measurement of the turning, rolling and obstacle resistance of wheelchair castor wheels. *Journal of biomedical engineering*, 11(6):462–466, 1989.

[67] Stephen Sprigle, Morris Huang, and Jacob Misch. Measurement of rolling resistance and scrub torque of manual wheelchair drive wheels and casters. *Assistive Technology*, pages 1–13, 2019.

[68] Franco HN Chan, Mehdi Eshraghi, Mohammad A Alhazmi, and Bonita J Sawatzky. The effect of caster types on global rolling resistance in manual wheelchairs on indoor and outdoor surfaces. *Assistive Technology*, 30(4):176–182, 2018.

[69] David S Wein. *The effects of a selected wheel design and caster fixture design on pushing force when pushing four wheeled industrial carts.* PhD thesis, The University of Wisconsin-Milwaukee, 2014.

[70] David P VanSickle, Rory A Cooper, and Michael L Boninger. Road loads acting on manual wheelchairs. *IEEE Transactions on Rehabilitation Engineering*, 8(3):371–384, 2000.

[71] Haoyong Yu, Matthew Spenko, and Steven Dubowsky. Omni-directional mobility using active split offset castors. *J. Mech. Des.*, 126(5):822–829, 2004.

[72] Songfeng Guo, Rory A Cooper, Tom Corfman, Dan Ding, and Garrett Grindle. Influence of wheelchair front caster wheel on reverse directional stability. *Assistive technology*, 15(2):98–104, 2003.

[73] Larry Russell Crichlow. *Development of a comprehensive mathematical model and physical interface for manual wheelchair simulation.* PhD thesis, University of Toronto, 2011.

[74] Min Huang. *Dynamic modeling and simulation analysis of an AGV (CONCIC-2 AGV).* PhD thesis, Concordia University, 1991.

[75] Alberto Doria, Luca Taraborrelli, Tarek Jomaa, Tom Peijs, Mario Potter, Sunjoo Advani, and Larry Crichlow. Identification of the mechanical properties of tires for wheelchair simulation. *The Open Mechanical Engineering Journal*, 10(1), 2016.

[76] HB Pacejka and IJM Besselink. Magic formula tyre model with transient properties. *Vehicle system dynamics*, 27(S1):234–249, 1997.

[77] Qian Wang, Zhi Peng Li, and Dao Qiang Wang. Structural Design and Analysis on Frame of Blueberry Harvesters Based on ANSYS. *Applied Mechanics and Materials*, 26-28:794, June 2010. ISBN: 9780878492497 Num Pages: 794 Place: Zurich, Switzerland Publisher: Trans Tech Publications Ltd.

[78] Martin Langner and David Sanders. Controlling wheelchair direction on slopes. *Journal of Assistive Technologies*, 2008.

[79] Ghusn Abdul Redha Ibraheem, Ahmad Taher Azar, Ibraheem Kasim Ibraheem, and Amjad J Humaidi. A novel design of a neural network-based fractional pid controller for mobile robots using hybridized fruit fly and particle swarm optimization. *Complexity*, 2020, 2020.

[80] Nabil H Hadi and Kawther K Younus. Path tracking and backstepping control for a wheeled mobile robot (wmr) in a slipping environment. In *IOP Conference Series: Materials Science and Engineering*, volume 671, page 012005. IOP Publishing, 2020.

[81] Alexandr Stefek, Thuan Van Pham, Vaclav Krivanek, and Khac Lam Pham. Energy comparison of controllers used for a differential drive wheeled mobile robot. *IEEE Access*, 8:170915–170927, 2020.

[82] Mauricio F Jaramillo-Morales, Sedat Dogru, and Lino Marques. Generation of energy optimal speed profiles for a differential drive mobile robot with payload on straight trajectories. In *2020 IEEE International Symposium on Safety, Security, and Rescue Robotics (SSRR)*, pages 136–141. IEEE, 2020.

[83] Xing Wu, Jorge Angeles, Ting Zou, Haining Xiao, Wei Li, and Peihuang Lou. Steering-angle computation for the multibody modelling of differential-driving mobile robots with a caster. *International Journal of Advanced Robotic Systems*, 15(6):1729881418820166, 2018.

[84] RS Sharp and R Granger. On car steering torques at parking speeds. *Proceedings of the Institution of Mechanical Engineers, Part D: Journal of Automobile Engineering*, 217(2):87–96, 2003.

[85] Dong Cao, Bin Tang, Haobin Jiang, Chenhui Yin, Di Zhang, and Yingqiu Huang. Study on low-speed steering resistance torque of vehicles considering friction between tire and pavement. *Applied Sciences*, 9(5):1015, 2019.

[86] Jo Yung Wong. *Theory of ground vehicles*. John Wiley & Sons, 2008.

[87] Moustapha Doumiati, Aa Victorino, Ali Charara, and Daniel Lechner. Lateral load transfer and normal forces estimation for vehicle safety: experimental test. *Vehicle System Dynamics*, 47(12):1511–1533, 2009.

[88] YU Zhisheng. *Theory of the automobile*. machine industry press, Beijing, 1990.

[89] Michael Selig, Boris Lorenz, Dirk Henrichmöller, Karsten Schmidt, Andrew Ball, and Bo Persson. Rubber friction and tire dynamics: A comparison of theory with experimental data. *Tire science and technology*, 42(4):216–262, 2014.

[90] V Colli, Giovanni Tomassi, and Maurizio Scarano. " single wheel" longitudinal traction control for electric vehicles. *IEEE Transactions on Power Electronics*, 21(3):799–808, 2006.

[91] Jian Jun Zhu. Study of vehicle dynamics with planar suspension systems (pss). 2011.

[92] Sulakshan Rajendran, Sarah K Spurgeon, Georgios Tsampardoukas, and Ric Hampson. Estimation of road frictional force and wheel slip for effective antilock braking system (abs) control. *International Journal of Robust and Nonlinear Control*, 29(3):736–765, 2019.

[93] Junmin Wang, Lee Alexander, and Rajesh Rajamani. Gps based real-time tire-road friction coefficient identification. 2004.

[94] Peter D Cenek, Neil J Jamieson, and Maurice W McLarin. Frictional characteristics of roadside grass types. *Opus International Consultants, Central Laboratories, Gracefield, New Zealand*, 2005.

[95] JD Summers, KP Self, and GL McLaughlin. Performance of i-3 traction implement tires on sod and soil. *SAE Transactions*, pages 616–621, 1987.

[96] M Schreiber, HD Kutzbach, et al. Influence of soil and tire parameters on traction. *Research in Agricultural Engineering*, 54(2):43–49, 2008.

[97] TC Petterson and SD Gooch. Rolling resistance of atv tyres in agriculture. In *Proceedings of the Design Society: DESIGN Conference*, volume 1, pages 2561–2570. Cambridge University Press, 2020.

[98] J Leathwick, F Morgan, G Wilson, D Rutledge, M McLeod, and K Johnston. Land environments of new zealand: a technical guide (p. 184). *Hamilton: Ministry for the Environment, Wellington, and Manaaki Whenua Landcare Research*, 2002.

[99] Jan Wieckhorst, Thomas Fedde, and Ludger Frerichs. Echtzeitmessung von traktionsparametern eines traktors bei der bodenbearbeitung. *Landtechnik*, 74(1/2):10–22, 2019.

[100] Hamid Taghavifar and Aref Mardani. Net traction of a driven wheel as affected by slippage, velocity and wheel load. *Journal of the Saudi Society of Agricultural Sciences*, 14(2):167–171, 2015.

[101] Pavel Osinenko. Optimal slip control for tractors with feedback of drive torque. 2015.

Appendix A

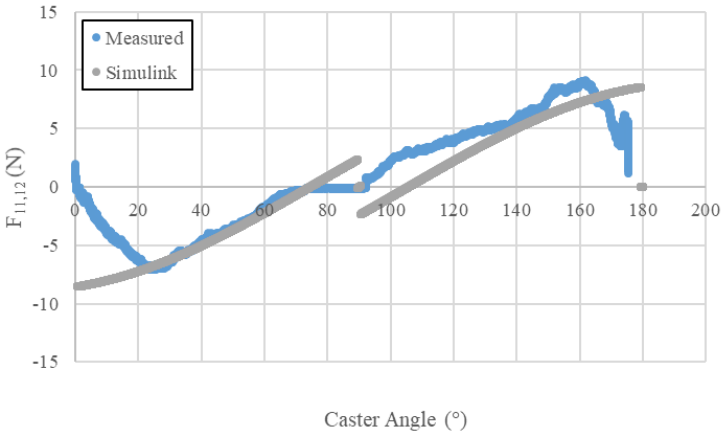

Figure 7.1: *Lateral reaction force vs caster angle @ 82.3 N.*

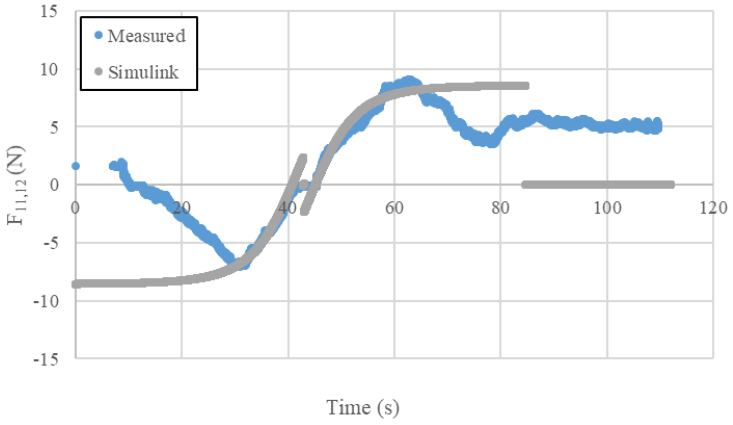

Figure 7.2: *Lateral reaction force and angle vs time @ 82.3 N.*

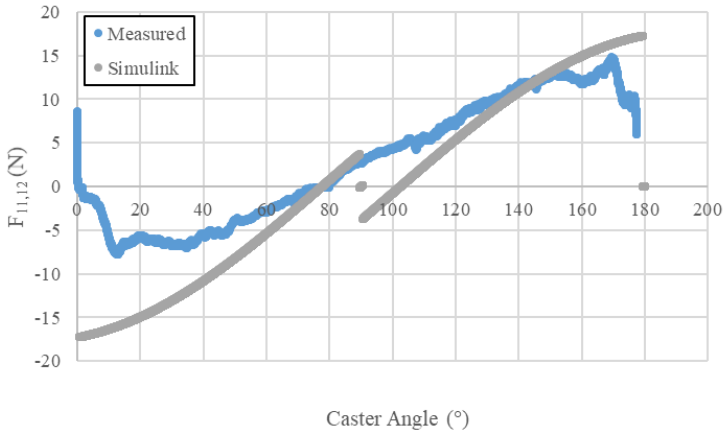

Figure 7.3: *Lateral reaction force vs caster angle @ 131.3 N.*

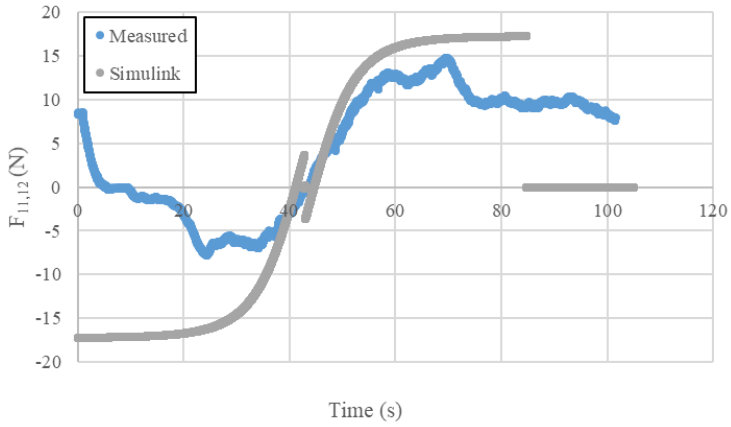

Figure 7.4: *Lateral reaction force and angle vs time @ 131,3 N.*

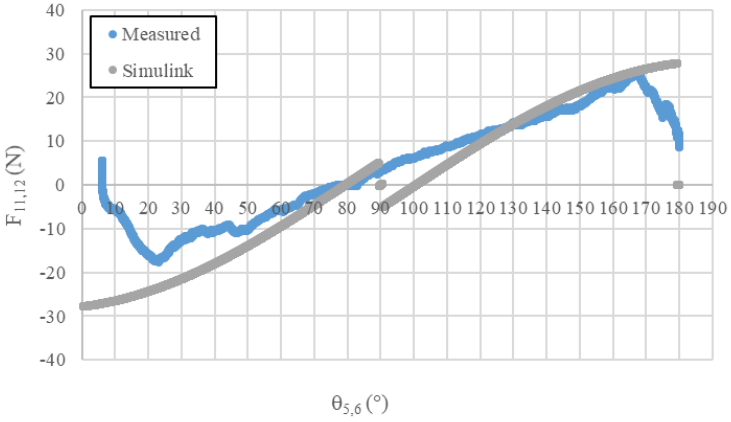

Figure 7.5: *Lateral reaction force vs caster angle @ 180.4 N.*

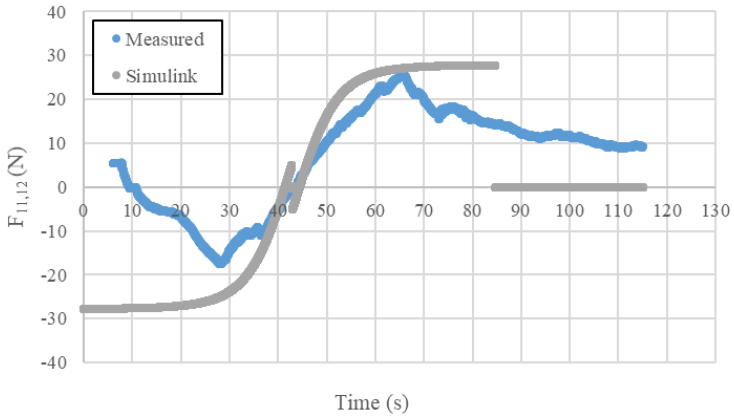

Figure 7.6: *Lateral reaction force and angle vs time @ 180.4 N.*

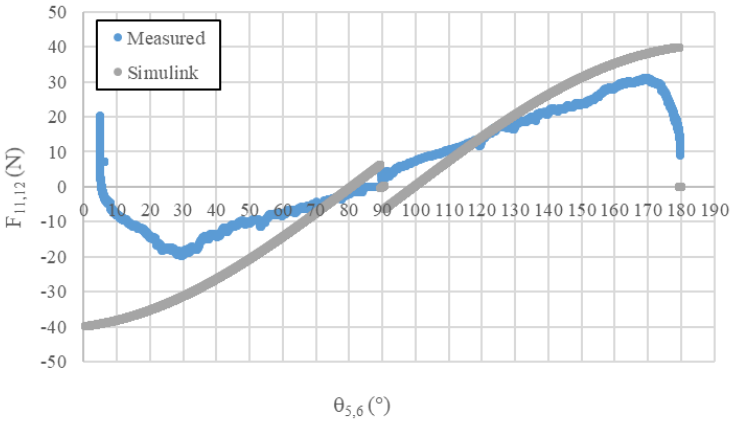

Figure 7.7: *Lateral reaction force vs caster angle @ 229.4 N.*

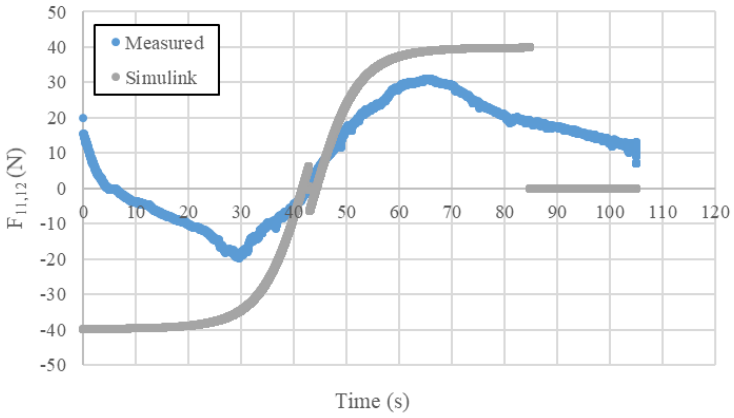

Figure 7.8: *Lateral reaction force and angle vs time @ 229.4 N.*

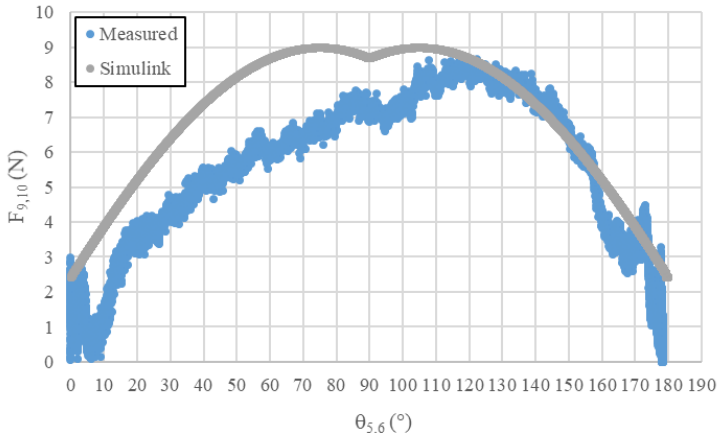

Figure 7.9: *Longitudinal reaction force vs caster angle @ 82.3 N.*

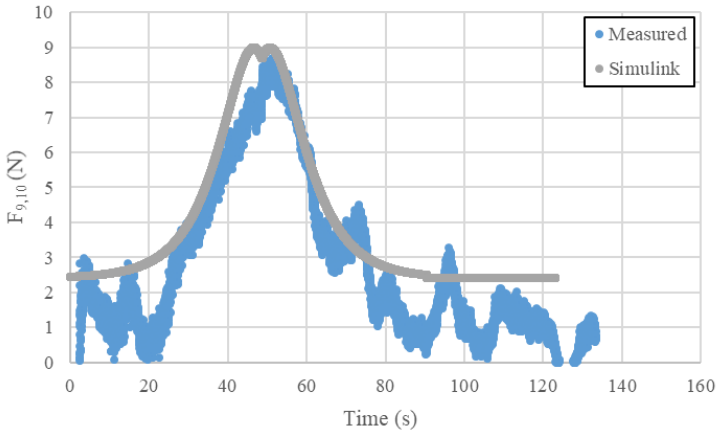

Figure 7.10: *Longitudinal reaction force vs time @ 82.3 N.*

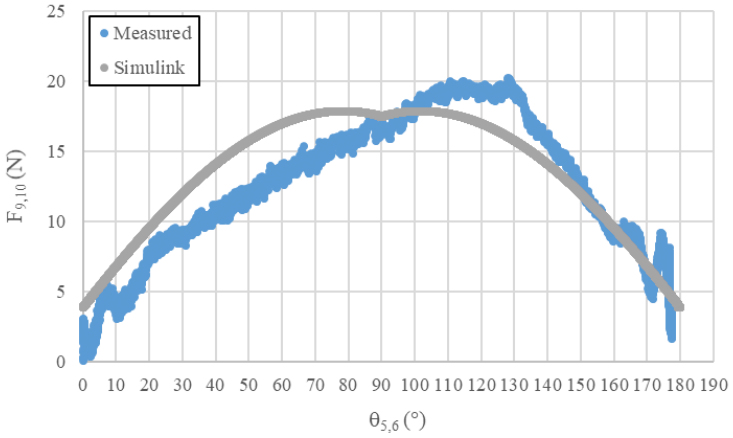

Figure 7.11: *Longitudinal reaction force vs caster angle @ 131.3 .*

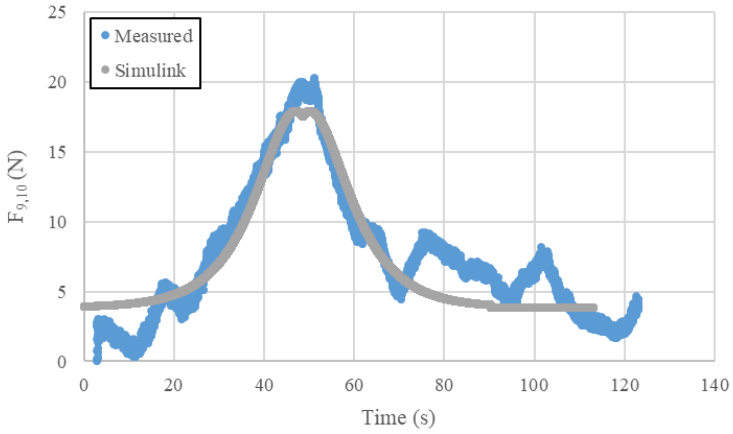

Figure 7.12: *Longitudinal reaction force vs time @ 131.3. N.*

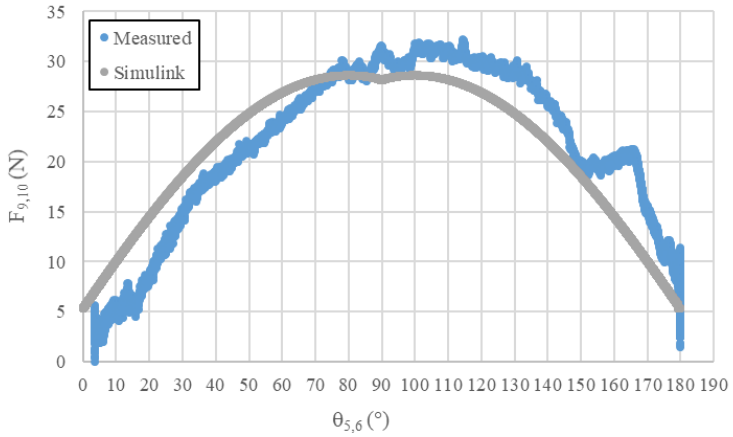

Figure 7.13: *Longitudinal reaction force vs caster angle @ 180.4 N.*

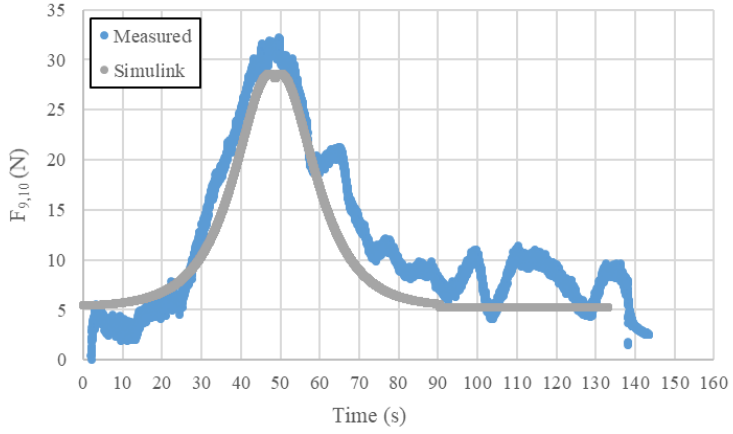

Figure 7.14: *Longitudinal reaction force vs time @ 180.4 N.*

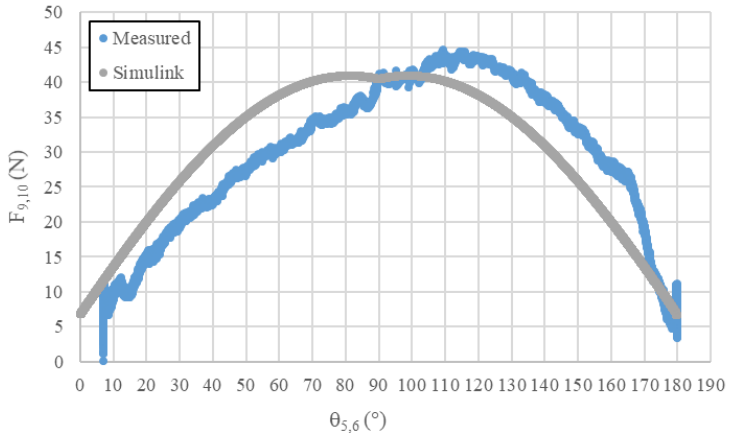

Figure 7.15: *Longitudinal reaction force vs caster angle @ 229.4 N.*

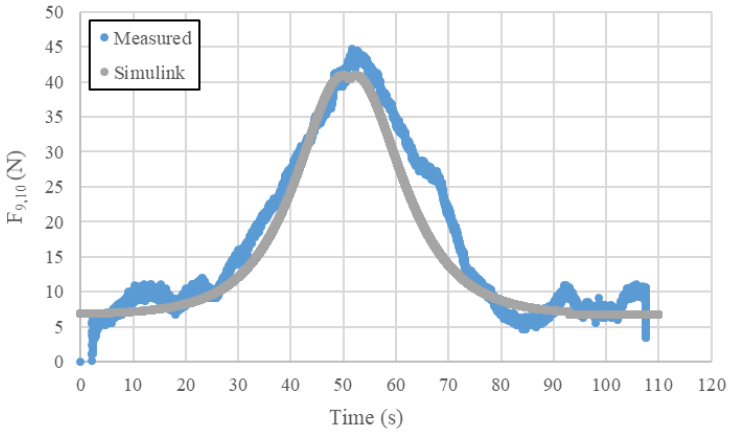

Figure 7.16: *Longitudinal reaction force vs time @ 229.4 N.*

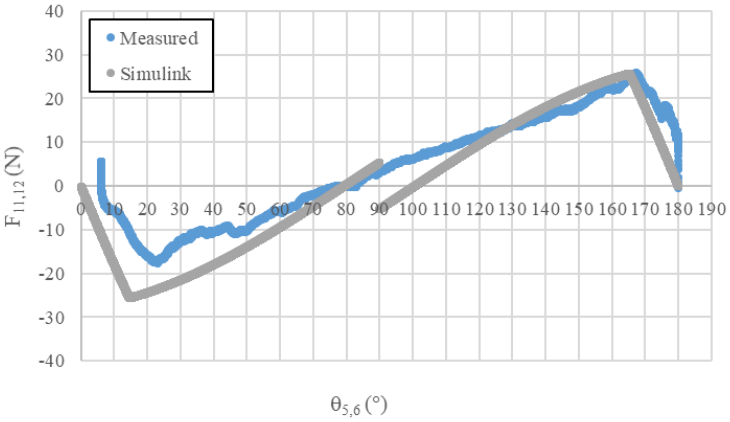

Figure 7.17: *Lateral reaction force vs caster angle @ 180.4 N with adjusted function.*

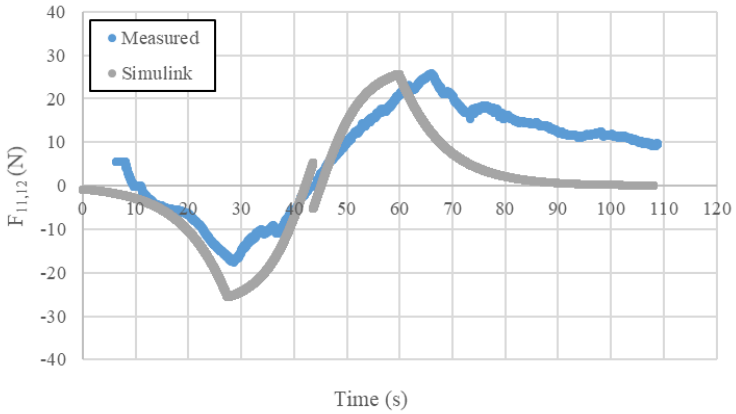

Figure 7.18: *Lateral reaction force and angle vs time @ 180.4 N with adjusted function.*

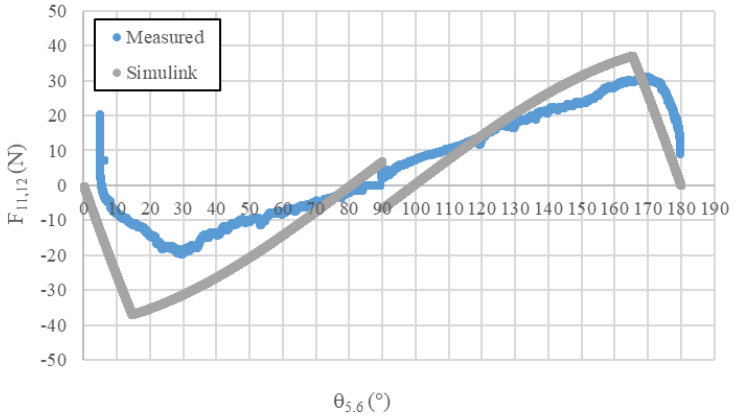

Figure 7.19: *Lateral reaction force vs caster angle @ 229.4 N with adjusted function.*

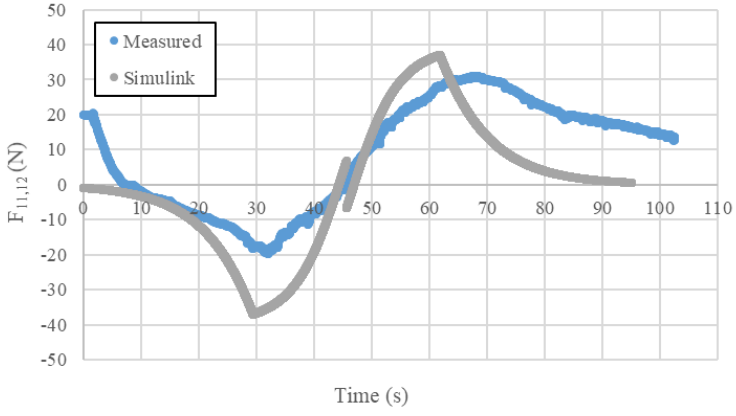

Figure 7.20: *Lateral reaction force and angle vs time @ 229.4 N with adjusted function.*

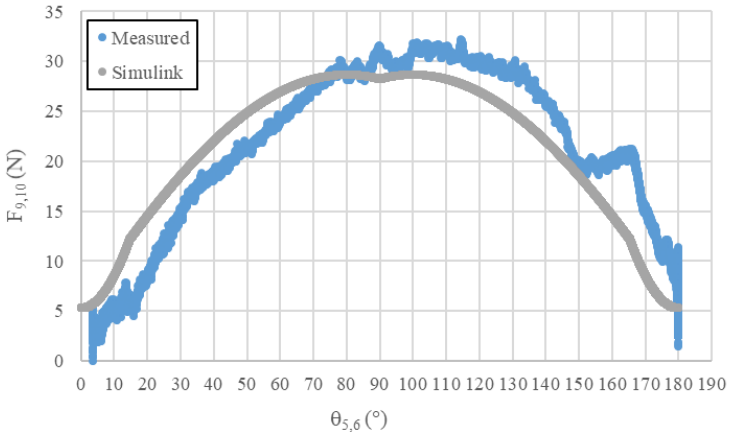

Figure 7.21: *Longitudinal reaction force vs caster angle @ 180.4 N with adjusted function.*

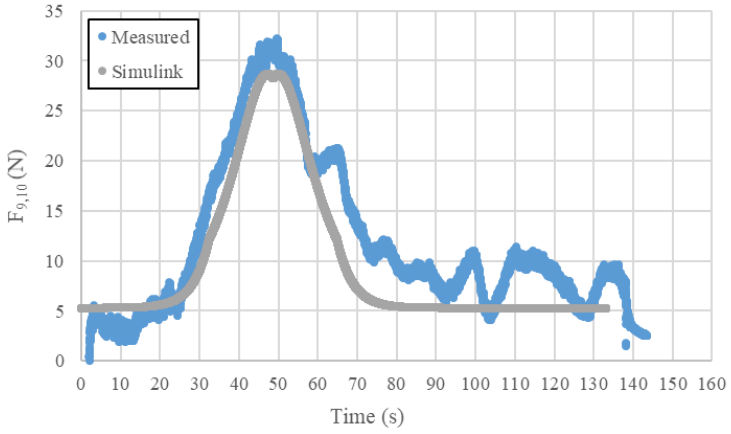

Figure 7.22: *Longitudinal reaction force vs time @ 180.4 N with adjusted function.*

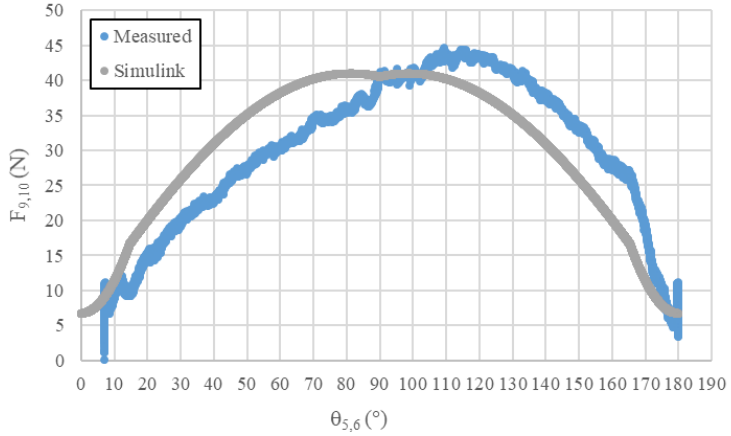

Figure 7.23: *Longitudinal reaction force vs caster angle @ 229.4 N with adjusted function.*

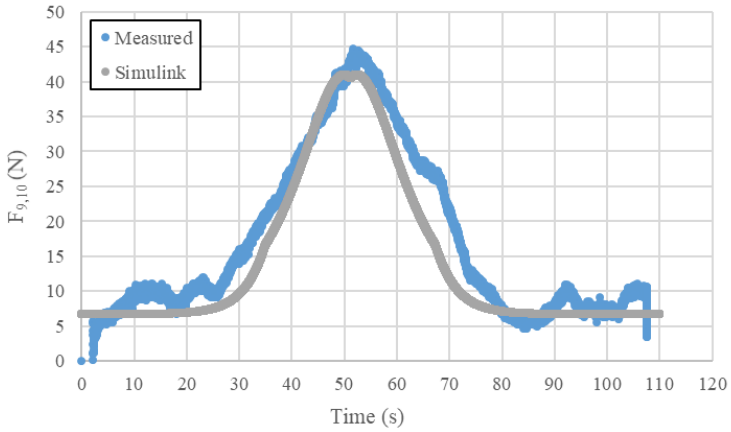

Figure 7.24: *Longitudinal reaction force vs time @ 229.4 N with adjusted function.*

Appendix B

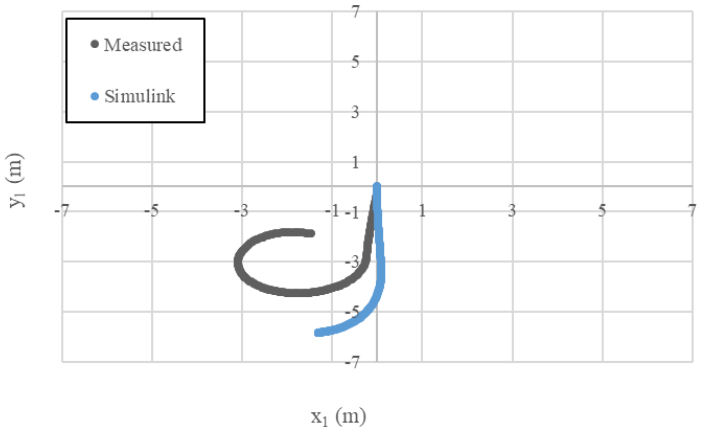

Figure 7.25: *Nico Bot test 2 trajectory.*

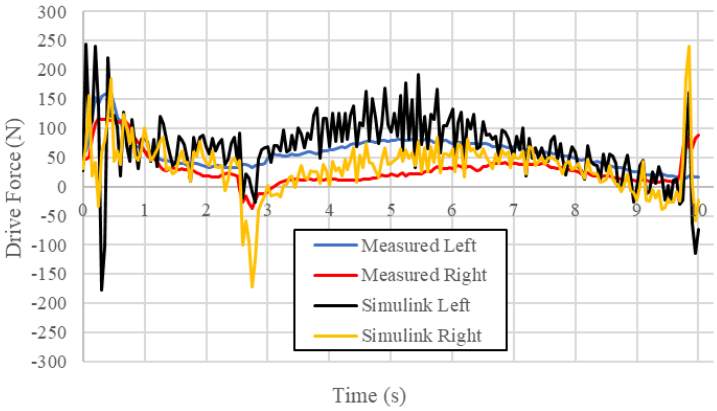

Figure 7.26: *Nico Bot test 2 drive forces.*

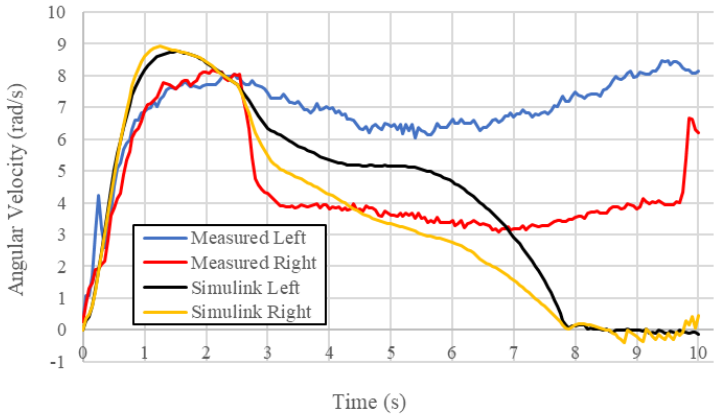

Figure 7.27: *Nico Bot test 2 wheel velocities.*

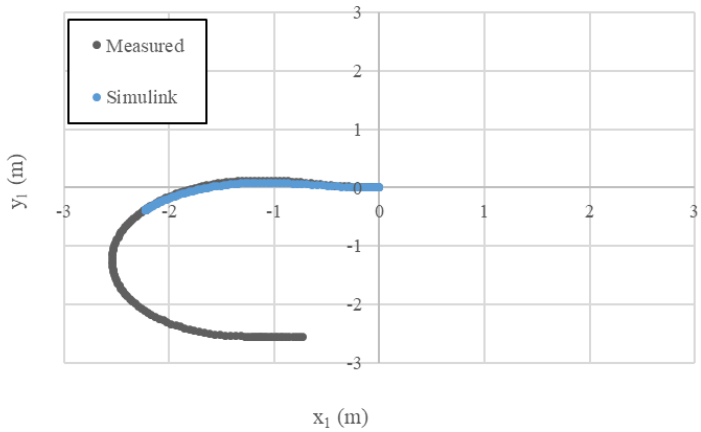

Figure 7.28: *Nico Bot test 3 trajectory.*

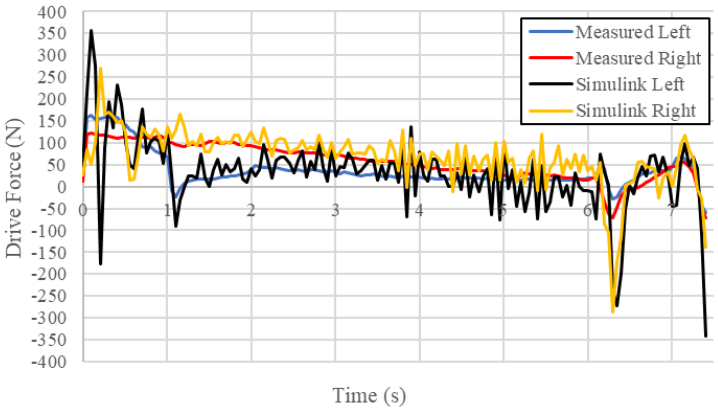

Figure 7.29: *Nico Bot test 3 drive forces.*

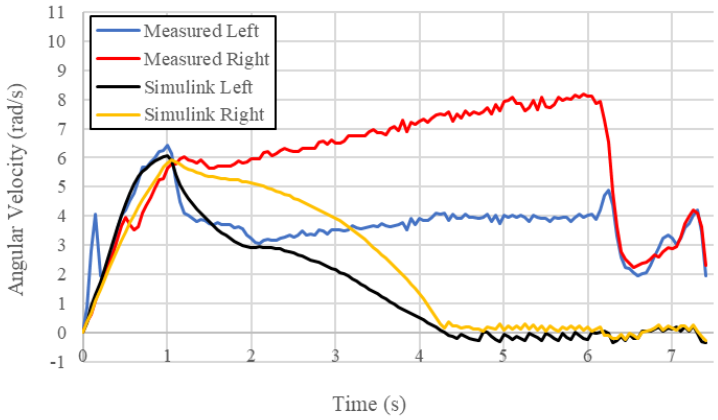

Figure 7.30: *Nico Bot test 3 wheel velocities.*

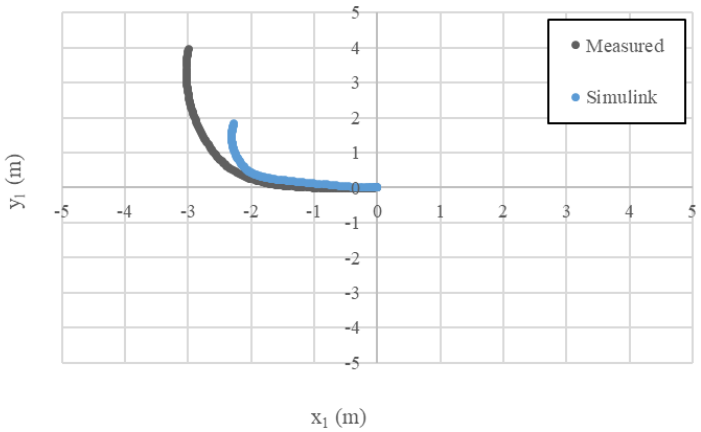

Figure 7.31: *Nico Bot test 6 trajectory.*

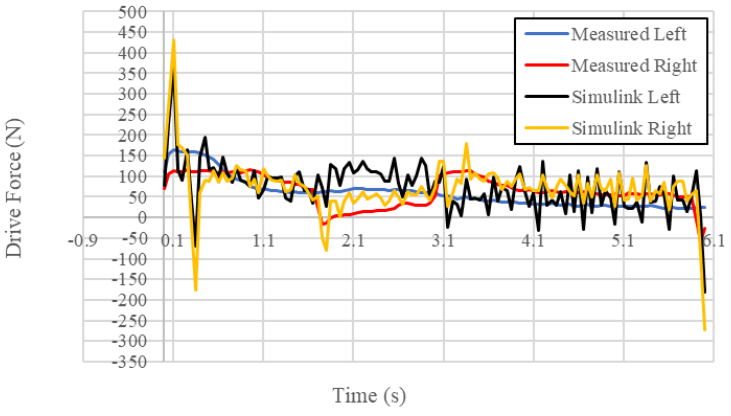

Figure 7.32: *Nico Bot test 6 drive forces.*

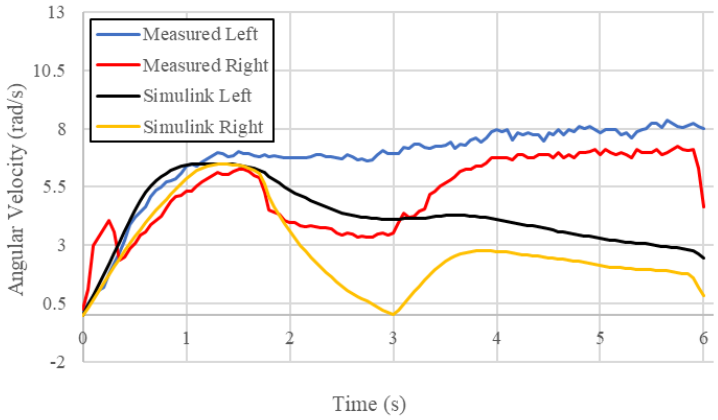

Figure 7.33: *Nico Bot test 6 wheel velocities.*

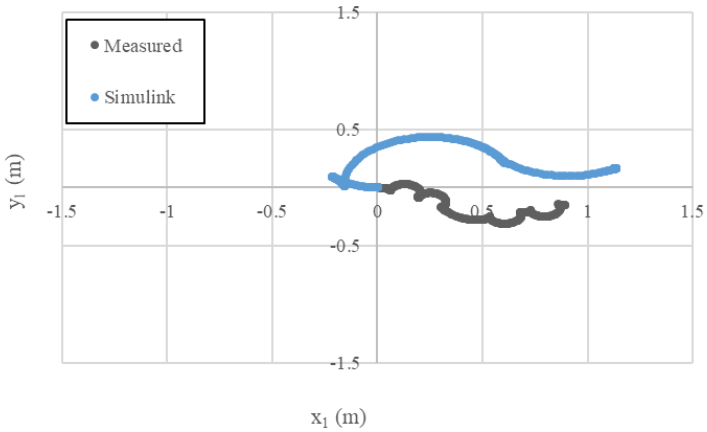

Figure 7.34: *Nico Bot test 7 trajectory.*

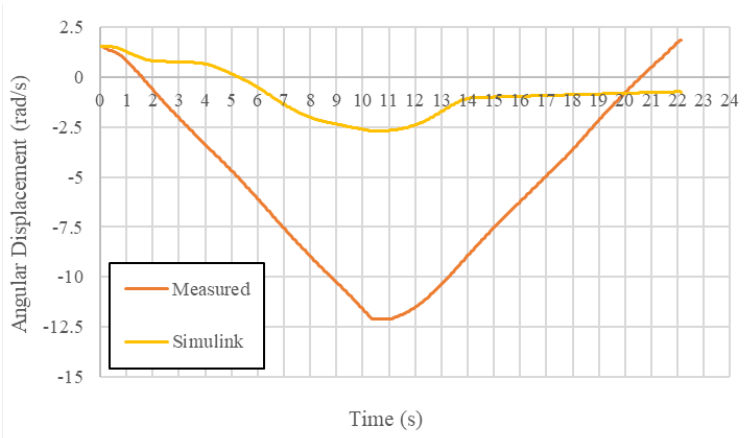

Figure 7.35: *Nico Bot angular displacement test 7.*

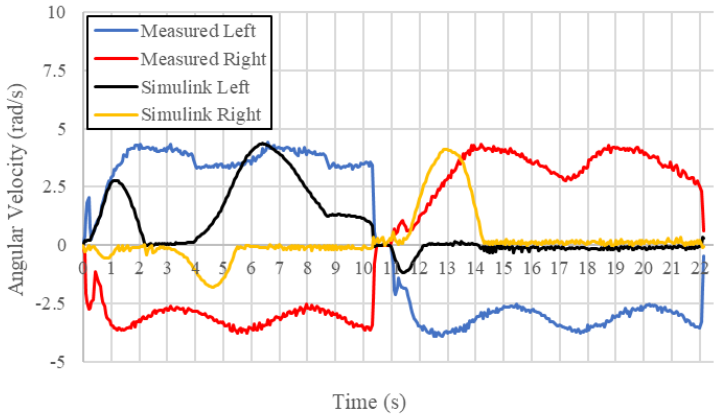

Figure 7.36: *Nico Bot test 7 wheel velocities.*

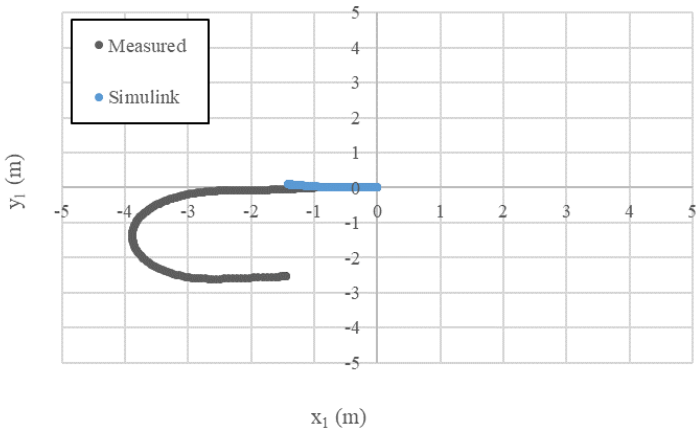

Figure 7.37: *Nico Bot test 8 trajectory.*

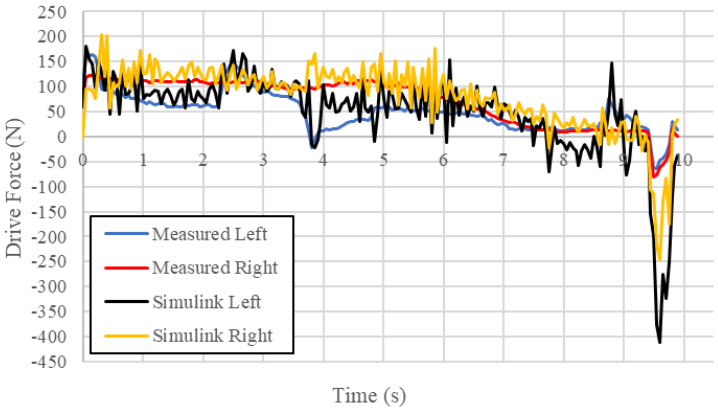

Figure 7.38: *Nico Bot test 8 drive forces.*

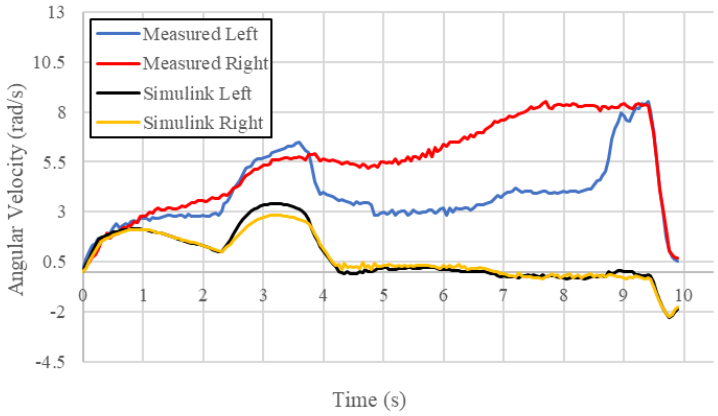

Figure 7.39: *Nico Bot test 8 wheel velocities.*

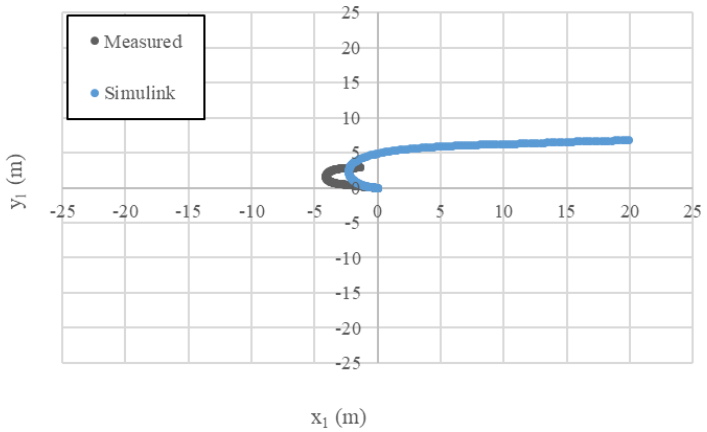

Figure 7.40: *Nico Bot test 9 trajectory.*

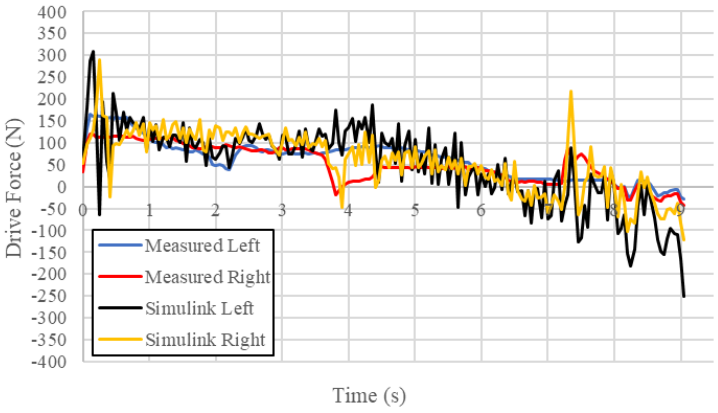

Figure 7.41: *Nico Bot test 9 drive forces.*

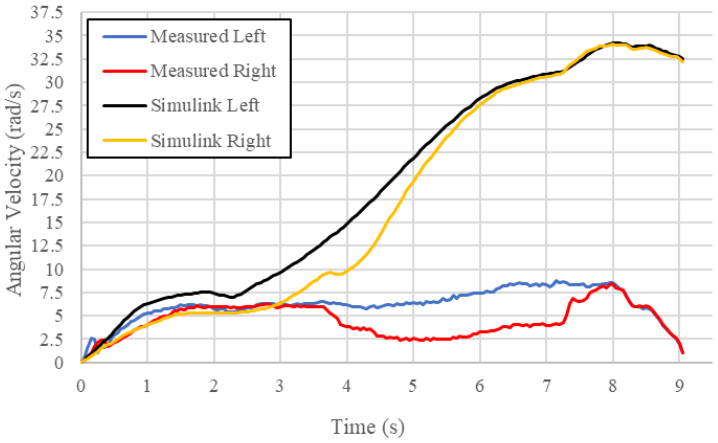

Figure 7.42: *Nico Bot test 9 wheel velocities.*

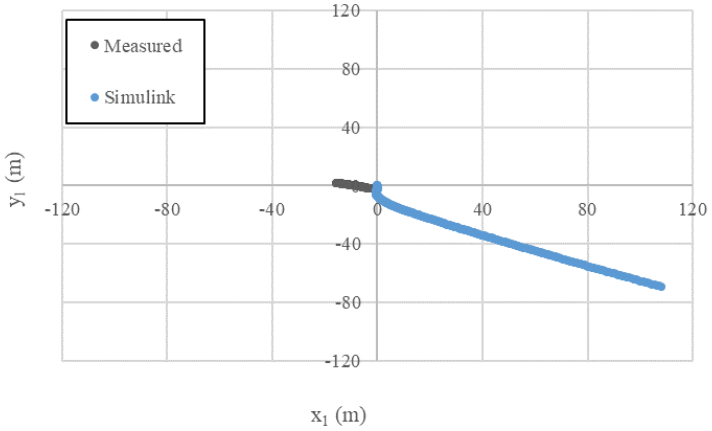

Figure 7.43: *Nico Bot test 10 trajectory.*

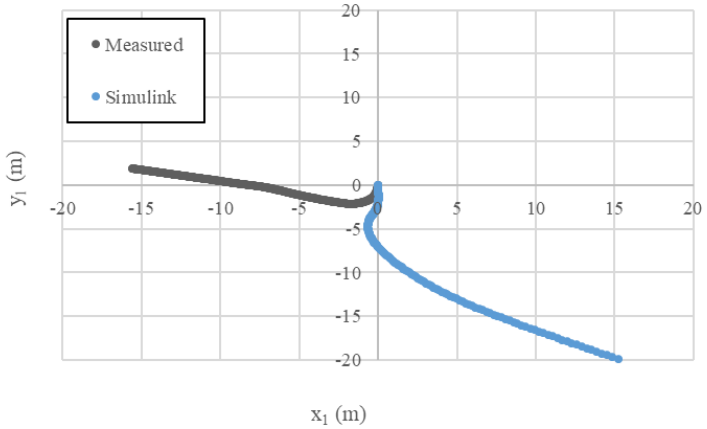

Figure 7.44: *Nico Bot test 10 trajectory zoomed in.*

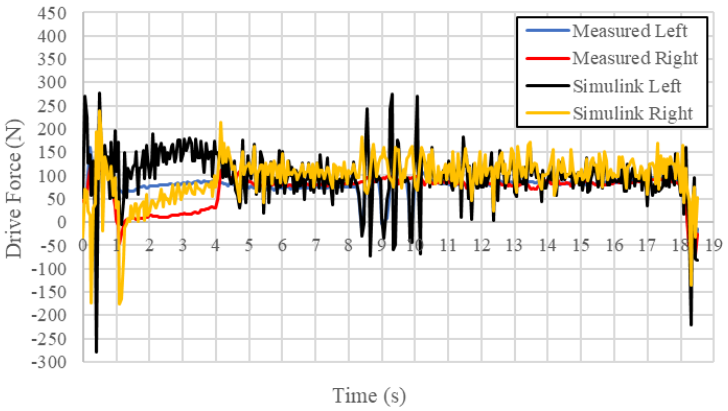

Figure 7.45: *Nico Bot test 10 drive forces.*

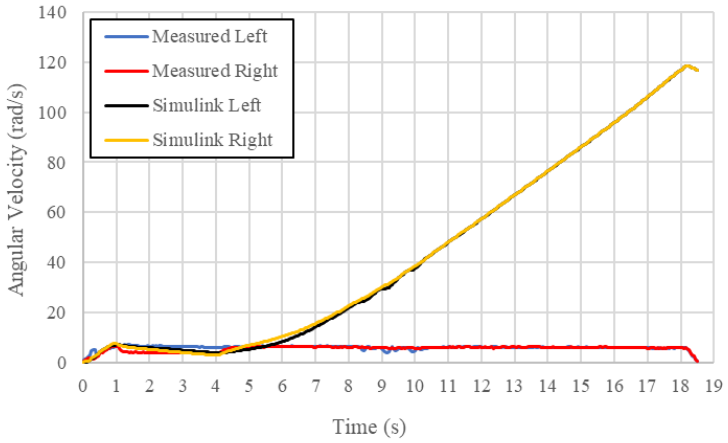

Figure 7.46: *Nico Bot test 10 wheel velocities.*

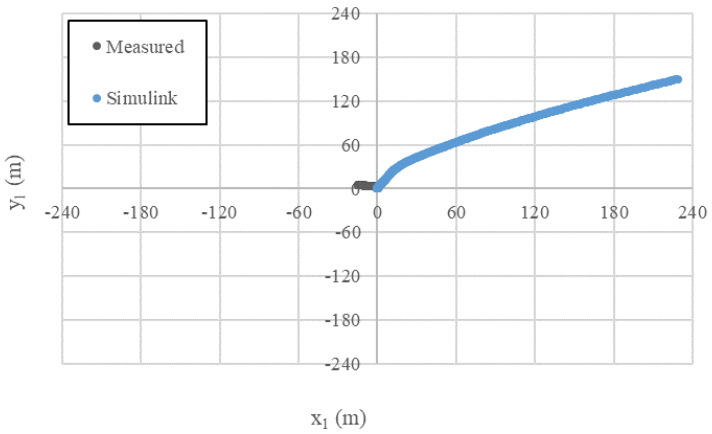

Figure 7.47: *Nico Bot test 11 trajectory.*

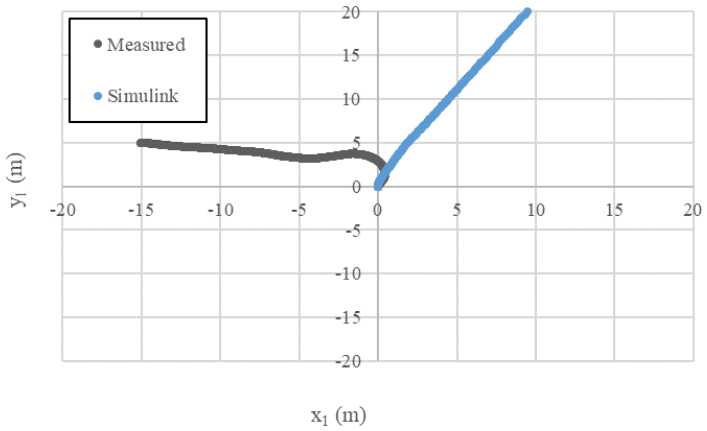

Figure 7.48: *Nico Bot test 11 trajectory zoomed in.*

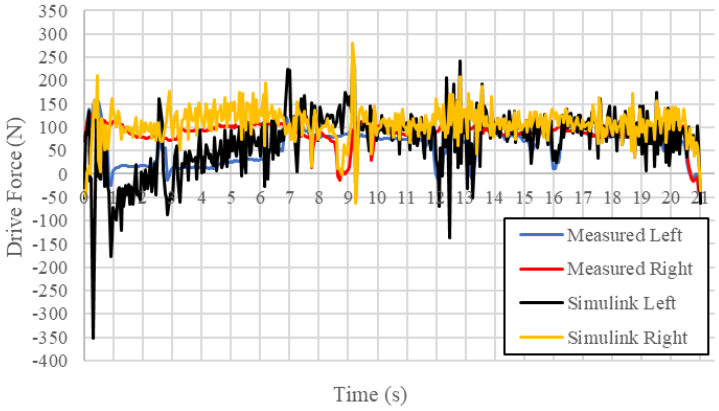

Figure 7.49: *Nico Bot test 11 drive forces.*

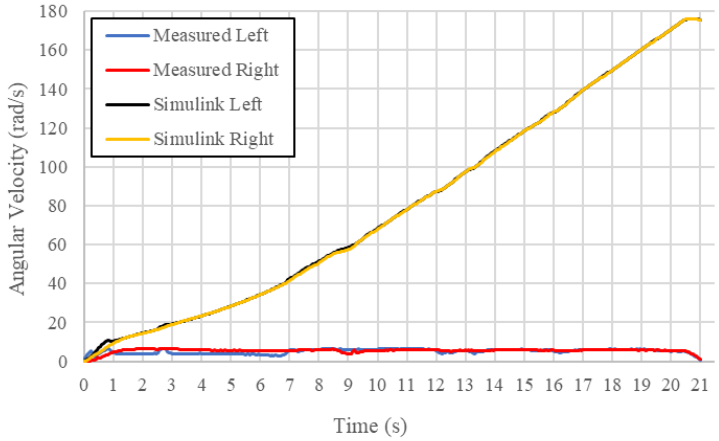

Figure 7.50: *Nico Bot test 11 wheel velocities.*

Appendix C

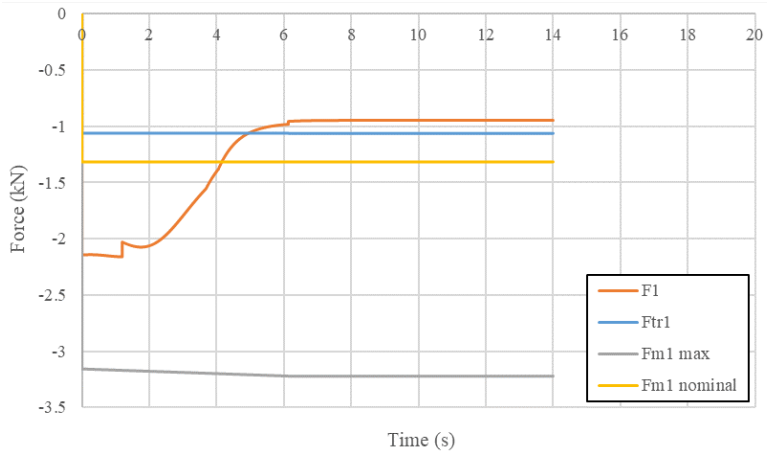

Figure 7.51: *Drive force, traction force, max motor drive force and nominal motor drive force vs time for left drive wheel, Trajectory 6, default dimensions.*

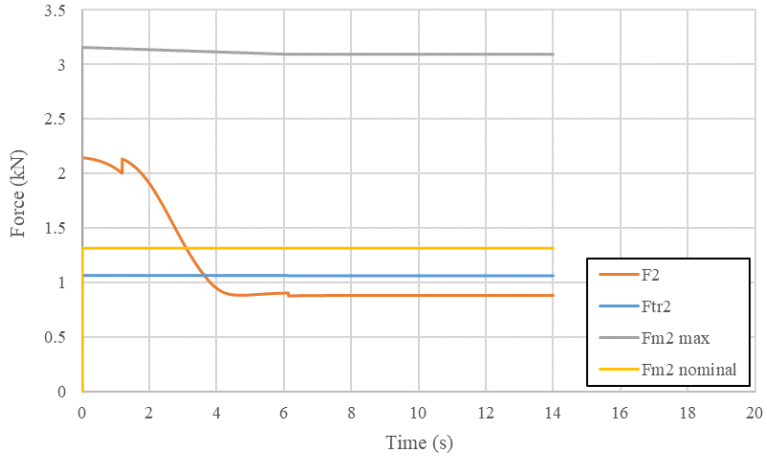

Figure 7.52: *Drive force, traction force, max motor drive force and nominal motor drive force vs time for right drive wheel, Trajectory 6, default dimensions.*

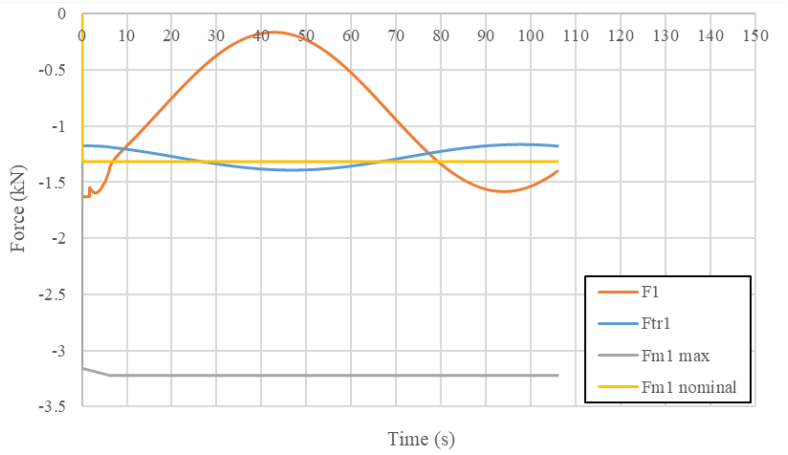

Figure 7.53: *Drive force, traction force, max motor drive force and nominal motor drive force vs time for left drive wheel, Trajectory 7,* $d_4 = 0.25$ *and* $d_1 = 1.2$.

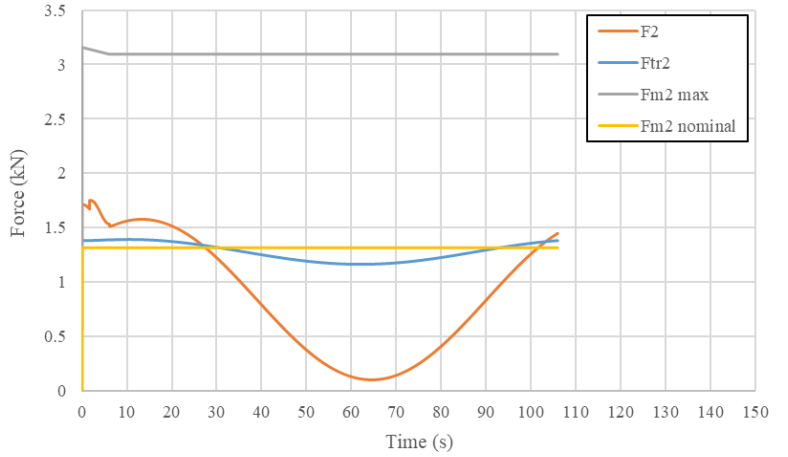

Figure 7.54: *Drive force, traction force, max motor drive force and nominal motor drive force vs time for right drive wheel, Trajectory 7,* $d_4 = 0.25$ *and* $d_1 = 1.2$.

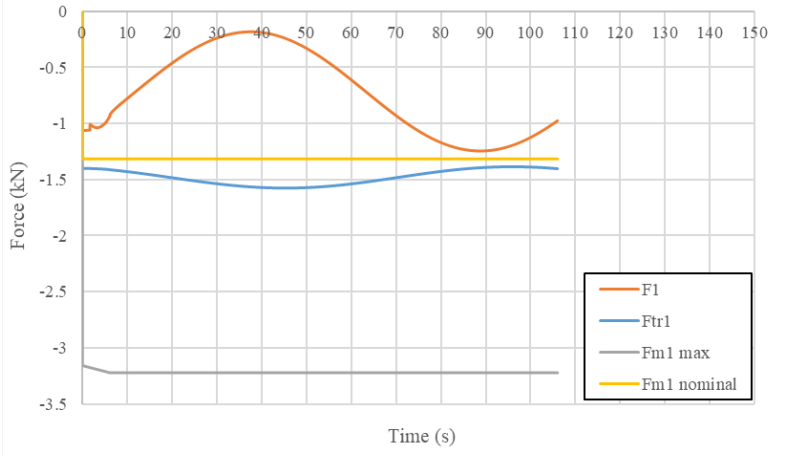

Figure 7.55: *Drive force, traction force, max motor drive force and nominal motor drive force vs time for left drive wheel, Trajectory 7,* $d_4 = 0.25$ *and* $d_1 = 0.8$, $2L_2 = 2.4$.

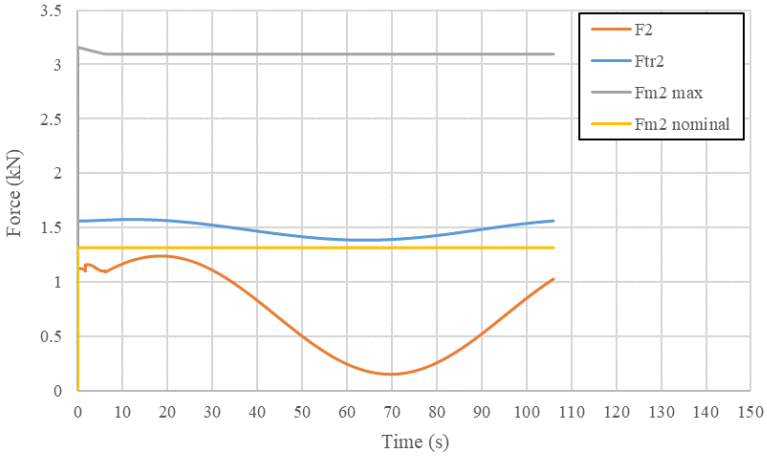

Figure 7.56: *Drive force, traction force, max motor drive force and nominal motor drive force vs time for right drive wheel, Trajectory 7,* $d_4 = 0.25$ *and* $d_1 = 0.8$, $2L_2 = 2.4$.